

Connections Between Atmospheric Blocking, General Circulation,
and Weather Extremes in a Hierarchy of Models and Various
Climates

by

Veeshan Narinesingh

A dissertation submitted to the Graduate Faculty in Physics in partial fulfillment
of the requirements for the degree of Doctor of Philosophy, The City University of

New York

2022

© 2022

Veeshan Narinesingh

All Rights Reserved

Connections Between Atmospheric Blocking, General Circulation, and Weather Extremes in a
Hierarchy of Models and Various Climates

by

Veeshan Narinesingh

This manuscript has been read and accepted for the Graduate Faculty in Physics in satisfaction of
the dissertation requirement for the degree of Doctor of Philosophy.

Date

James F. Booth

Chair of Examining Committee

Date

Alexios Polychronakos

Executive Officer

Supervisory Committee:

Yi Ming

Tobias Schäfer

Zhengzhao Johnny Luo

Gillian Bayne

THE CITY UNIVERSITY OF NEW YORK

ABSTRACT

Connections Between Atmospheric Blocking, General Circulation, and Weather

Extremes in a Hierarchy of Models and Various Climates

By

Veeshan Narinesingh

Advised by: Dr. James F. Booth

The field of geophysical fluid dynamics (GFD) includes the study of both the motion and thermodynamic aspects of the atmosphere. These properties are of particular importance because they directly influence both local and large-scale weather and climate and are associated with various phenomena. One phenomena that is particularly influential is atmospheric blocking. Atmospheric blocks are persistent, quasi-stationary anticyclones (a.k.a. high-pressure systems) that occur in the atmosphere and disrupt the flow. Blocks are known to induce heat extremes and cold spells, as well as steer storms and cause numerous types of hazards. Yet despite the hazards associated with blocks, our current physical understanding and simulations of blocking are lacking. For example, no one has fully explained why blocking occurs more in some regions than others or how blocking will change in future climates. Another open question regarding blocking relates to the numerical models used to create climate projections: the models have biases in their representation of blocking, but the cause of the biases has not been determined. As such, this thesis investigates the climatology, dynamics, and impacts of atmospheric blocking within various models and climate forcing conditions. This is divided into three original research components.

The first research component utilizes an idealized moist general circulation model (GCM) to: (1) investigate the dynamics of blocking in an aquaplanet, and (2) determine how the orographically-induced mean circulation features affect the climatology of blocking. For this, a model integration using an aquaplanet configuration is compared to reanalysis and separate idealized model integrations that include mountains. Blocks in the aquaplanet are found to exhibit a similar evolution of eddy momentum flux convergence and geopotential height compared to reanalysis and orographic integrations. In the orographic integrations, we find that blocking is anchored upstream of the high-pressure stationary wave anomaly induced by orography. On the other hand, blocking minimizes near the low-pressure stationary wave anomaly where zonal flow maximizes. As the height of orography is increased, we find a correlation between stationary wave amplitude and hemispherically-averaged blocking frequency. Overall, these results help explain the regional variations in blocking location and emphasize the importance of mean circulation features in setting the frequency and location of blocking.

The second research component compares blocking in two comprehensive GCMs with contrasting ocean forcing. The first model, AM4, is an atmosphere only model forced by observed sea-surface-temperatures. The second model, CM4, is a coupled atmosphere-ocean model. Because it has a free-running ocean, CM4 has more atmospheric mean state biases than AM4. In particular, it exhibits equatorward-shifted mean zonal winds and contracted Hadley circulation compared to reanalysis and AM4. Despite the difference in zonal circulation between AM4 and CM4, however, both models produce similar blocking climatology biases: too much blocking in the Pacific and too little in the Atlantic. This result is consistent with both models' biases in the stationary wave, which is amplified near the Pacific blocking maxima, and weakened in the Atlantic. This result is not simply self-consistent. We know this because we find that the stationary

wave bias exists even if we only consider the time periods when no blocking is detected in the reanalysis. Our results suggest that biases in the stationary wave are more relevant than biases in the climatological jet in generating biases in blocking for these models. Block-centered compositing analysis confirms that the models reproduce realistic onset of Atlantic and Pacific blocking in terms of geopotential height and transient eddy momentum flux convergence.

The third research component focuses on blocking and persistent extreme heat events in summer. This is done by analyzing reanalysis as well as historical and climate change integrations of CM4. First, the regional variation of blocking and heat extreme co-location is investigated. We find that blocks and heat extremes are co-located most often over northeastern and northwestern North America and over Scandinavia and northern Eurasia. For heat events in northeastern North America, we compare those that are associated with blocking to those that are not. The duration and evolution of 500 hPa geopotential height, 2 m temperature, sea-level-pressure, and the 1000 hPa temperature budget equation are analyzed. We find that, on average, blocked heat events are warmer and longer in duration for this region. We then shift focus to CM4, confirming the model's fidelity in simulating blocking and the association of blocking with heat extremes in the historical integration. In the climate change projection integration, less blocking occurs as compared to the historical integration and the association of blocks with heat extremes also decreases. Consistent with less blocking, composited heat events in the climate change projection exhibit anomalous temperatures that are 1-2 K cooler than in the historical integration. However, this is outweighed by a 6-7 K warming of the mean state.

Chapter 5 provides a summary and conclusions for the three research components. This chapter puts all of the novel physics research completed in for this dissertation in context. It also includes a discussion on possible future work.

Chapter 6 is a standalone chapter focused on original research in STEM education and diversity, in which the effects of mentorship on adolescents of color from underserved communities are investigated. This research grew out of a mentoring program that I co-founded. For this, college student mentors from similar sociocultural backgrounds guide youth throughout two 12-week semesters. Interpretive phenomenological analysis (IPA) is implemented to extract superordinate and subordinate themes from adolescent accounts within the program. The superordinate (subordinate) themes identified are as follows: social-emotional support (support with mental health, and family-like bonds and inclusivity), building paths to academic and professional success (demystifying success, and skills for success), and supporting connections to STEM (nurturing interests in STEM, and seeing oneself in STEM careers).

ACKNOWLEDGMENTS

Wow, so many people to thank: family, friends, mentors, institutions, students so many.

The first and most important person is my Mom. Thank you for showing me the value of hard work. All those double shifts, all that over time –it was never in vain. Your work-hard mentality was imprinted on me. Any time things get tough, I think back to how much you sacrificed, and it puts me in a mindset to make things happen. I also thank you for never giving up on me. I wonder. As you rode that plane from Trinidad to New York, with a dream of finding better opportunities for your kids, did you ever think that one of them could get a Ph.D.? This one is for you Mom, we accomplished this together.

Next, I have to thank my elder sister, Tina, for being like a second mom throughout my whole life. Thanks for always being there. Also thank you to my fiancé Alyssa. I can go on and on, but in particular, thanks for the encouragement, support and being such a great teammate in this game of life. Thank you to my nephews Tristan and Joey for the joy you bring and inspiring me to give you dudes a good role model to look up to.

Thank you to my cousins for always looking out and all the good times: Tariq, Nick, Lisa, Cuzaunty Karima, Rashema, Reshma, Sandip, Jeffrey, Avi, Valini, Mahen, Becky, Ricky, and everybody else. Big big shout out to all my uncle and aunty dem too: Aunty Ena, Aunty Patty, Aunty Seeta, Mamu, Uncle Navin, Uncle Dev, Uncle Harold, and the rest. Rest in peace and thank you as well to Aunty Gaitree and Uncle Prem –you treated me like a son and supported one of the most important aspects of my life: my education.

Thank you to my best friends since we were 12 years old, Lorenzo and Justin. Since I could first form meaningful memories, you dudes have brought so many laughs and really a sense of brotherhood into my life. Thank you, Lorenzo especially. You and my mom are truly my biggest

inspirations and I'm proud of your accomplishments just as much as my own. I also need to thank my colleagues and friends from school. All those hours spent suffering studying physics and doing research –we made it! Sung Soo, Charlie, Matt, Bryant, Mirko, Mandeep, Francesco, Ian, Katie, JJ, Carolien, Jiehao, Jireh, Spencer, Tracy, Farrah; I could not do this without you! Thank you to some other important colleagues as well: Shakira Lleras, Ben Lev, Andrew Peterson, Scott Moore, and a resounding thank you to Tiffani Kolozian.

My mentors now. Dr. Jimmy Booth, my Ph.D. advisor, I could go on and on, but you are not the sentimental type. So, I'll say this: Thanks for helping me grow not just as a professional and as a scientist, but also as a person. Thanks for allowing me to be me and giving me the room to pursue my own interests. You and Yi have been very supportive and understanding, but also challenged me to strive for greatness as a scientist. Dr. Yi Ming, my NOAA mentor, I'd also like to say thank you for believing in me. For someone as decorated as you are to show interest in my work and belief in me as a scientist, it really helped me to believe in myself.

I also want to thank Dr. Gillian Bayne for seeing value in me and mentoring me in scholarly work most close to my heart –STEM Education, Diversity, and Outreach. Where other professors couldn't be bothered, you took the time. Thank you as well to Dr. Stan Altman and Dr. Brian Schwartz. From working with you, I've learned a lot about myself. Thank you also to all my other great mentors/teachers over the years: Ms. Ganley, Mr. Harrison, Ms. Wright, Ms. Harlow, Ms. Morton, Dr. Cygan, Prof. Tiburzi, Prof. Hedberg, Prof. Boyer, Prof. Franco, Prof. Gayen, Prof. Menon, Claude Telesford, Greg Borman, Prof. Schaeffer, Prof. Luo, Prof. Block, Dr. Perkins, Dr. Jeff Secor, Dr. Sutkis, John Ferrin, Francois Nzi, Farrell Evans, Sarah Sakura, Reggie Mays, Jeffrey Booker, Dr. Degnan, and Bob Rubin.

Thank you to CCNY Physics, CCNY as a whole, and CUNY for the opportunity to pursue my dreams. I'm so proud to be from institutions that are such beacons of upward mobility. I especially want to thank certain administrators: Sue Turner, Daniel Moy, and Joan Brijlall. Also thank you to NOAA-CESSRST, NOAA EPP, and Geophysical Fluid Dynamics Laboratory for the amazing training and opportunities during my Ph.D. I especially would like to thank Dr. Shakila Merchant, Cesar Ortiz, Georgina Fekete, and the rest of the CESSRST staff. Thank you to Geophysical Fluid Dynamics Laboratory and its staff for access to models and data to produce my thesis research.

Last, but definitely not least are my mentees/students and their families. In particular Jireh, Claire, Ricardo, Nico, Isabel, Jeann, Cherif, Jaylen, Antonio, Zion, Triniim, and the rest of my brothers from Bridge Golf Foundation. You all have inspired and encouraged me so much. One reason I strive so hard for greatness is to be a great role model for you all. It has always been a two-way street, however, where I learn as much from you as you do from me. Thank you. I dedicate this thesis to you and can't wait to see what you all can accomplish in this life!

With Love,

Vee

This thesis was supported through NOAA Educational Partnership Program/Minority-Serving Institutions award number NA16SEC4810008 to the Center for Earth System Sciences and Remote Sensing Technologies at (CCNY, UPRM, UTEP, UMBC, or SDSU). Contents are solely the responsibility of the award recipient and may not represent official views of NOAA or the U.S. Department of Commerce.

Chapter 2 is published in Weather and Climate Dynamics (<https://doi.org/10.5194/wcd-1-293-2020>). Chapter 3 is currently under minor revision in Journal of Climate.

Contents

	Page
List of Tables	xv
List of Figures	xvii
Chapter 1: Introduction	1
1.1 What is Atmospheric Blocking?	1
1.2 Geophysical Fluid Fundamentals of Blocking.....	3
1.2a Rossby Waves in the Atmosphere.....	4
1.2a Building and Maintaining Blocks	6
1.3 Tracking Blocks	8
1.3a Background	8
1.3b Geopotential Height Anomalies.....	9
1.3c Block Detection and Tracking	10
1.4 Blocking: Observations and Simulations in Current and Future Climates	12
1.4a Blocking in Observations	12
1.4b Blocking in Comprehensive Models for Current Climates.....	16
1.4c Blocking in Future Climates	18
1.5 Outline of Thesis and Research	20
1.5a Chapter 2: Atmospheric Blocking in an Aquaplanet and the Impact of Orography	20
1.5b Chapter 3: Blocking and General Circulation in GFDL Comprehensive Climate Models.....	21
1.5c Chapter 4: Connections Between Atmospheric Blocking and Heat Extremes in Current and Possible Future Climates	21
Chapter 2: Atmospheric Blocking in an Aquaplanet and the Impact of Orography	23
2.1 Introduction.....	24
2.2 Methods	27
2.2a Reanalysis Data	27
2.2b Idealized Model Configurations	27
2.2c Block Detection and Tracking	30
2.2d Analysis Metrics	31
2.2e Analysis Methods.....	34

2.3 Results	37
2.3a Blocking in the aquaplanet, dynamical aspects, and intermodel comparison.....	37
2.3b Climatological Analysis.....	42
2.3c Block Duration Statistics.....	52
2.4 Discussion	56
2.5 Summary and Conclusion	58

Chapter 3: Blocking and General Circulation in GFDL Comprehensive Climate Models

3.1 Introduction	64
3.2 Methods	66
3.2a General Circulation Models	66
3.2b Stationary Wave and Mean Zonal Wind.....	67
3.2c Block Tracking, Climatology and Regional Sorting.....	67
3.2d Transient Eddy Forcing: Wave Activity Flux.....	70
3.2e Block-centered Compositing.....	72
3.2f Statistical Significance Testing	72
3.3 Results	74
3.3a General Circulation Features.....	74
3.3b Blocking Climatology	81
3.3c Block Count, Duration, and Area.....	84
3.3d Zonal background flow during block onset	86
3.3e Transient Eddy Forcing.....	88
3.4 Discussion	90
3.5 Summary and Conclusions	94

Chapter 4: Connections Between Atmospheric Blocking and Heat Extremes in Current and Possible Future Climates

4.1 Introduction.....	98
4.2 Methods	99
4.2a Reanalysis and General Circulation Models	99
4.2b Block Tracking and Climatology.....	100
4.2c Persistent Extreme Heat Events: Tracking and Block Association	101
4.2d Significance Testing	103
4.3 Results	104
4.3a The Association of Blocking and Heat Extremes in Reanalysis	104

4.3b Dynamical Comparison of Heat Extremes with and without Blocking	106
4.3c Blocking and Heat Extremes in CM4: Historical Simulation	113
4.3d Blocking and Heat Extremes in CM4: Climate Change Projection, RCP 8.5.....	115
4.4. Discussion: Causality Between Blocking and Persistent Extreme Heat Events.....	119
4.5 Summary and Conclusions	121
 Chapter 5: Conclusion and Discussion	125
5.1 Research Component 1: Atmospheric Blocking in an Aquaplanet and the Impact of Orography	125
5.2 Research Component 2: Blocking and General Circulation in GFDL Comprehensive Climate Models	128
5.3 Research Component 3: Connections Between Atmospheric Blocking and Heat Extremes in Current and Possible Future Climates	130
5.4 Concluding Remarks.....	134
 Chapter 6: Mentoring Youth through COVID and Beyond: Combatting Loneliness, Opportunity Gaps, and Underrepresentation in STEM	136
6.1 Introduction.....	137
6.1a A Mentoring Program To Combat Loneliness, Opportunity Gaps, And Underrepresentation	138
6.2b Institutions in Coalition	140
6.2 Methodology	141
6.2a Program Structure	141
6.2b Participants and Identity	142
6.2c Modes of Supportive Engagement	144
6.3 Programmatic Outcomes.....	148
6.3a Social-Emotional Support	149
6.3b Building Paths to Academic and Professional Success	151
6.2c Supporting Connections to STEM	155
6.4 Discussion and Conclusion	157
6.4a Key Takeaways	157
6.4b Improvements and Future Plans Beyond COVID	158
6.5 References (Chapter 6)	159
 References (Chapters 1-5)	163

List of Tables

	Page
Table 2.1. Regions used for subsetting blocks in the compositing and duration analysis. Each region spans 30° - 65° N, for the longitudes listed in the table	35
Table 2.2. Cool season area-averaged block frequency and number of events in the idealized model integrations. Asterisks indicate values that are significantly different from the aquaplanet.....	50
Table 2.3. Mean block duration and number of events in parentheses for midlatitude, cool season blocks in each idealized model configuration.....	54
Table 3.1. Normalized RMS error, F (Eq. 2), for regional blocking in AM4 and CM4 compared against ERA5 reanalysis. All regions cover only the midlatitudes (30° - 75° N). The Pacific, Atlantic, and All Midlatitude regions extends longitudinally from 153.75° - 241.25°, 288.75° - 16.25°, and 0° - 360°, respectively. “*” indicates significant differences between the models.	84
Table 3.2. For ERA5 reanalysis and both GFDL models (AM4 and CM4), block duration, standard deviation of block duration, and mean number of events per DJF in each region.	85
Table 3.3. For ERA5 reanalysis and both GFDL models (AM4 and CM4), mean block area and standard deviation of block area in each region.....	85
Table 4.1. Duration statistics for blocked and non-blocked 90th percentile heat events in New York City. Difference in average duration between blocked and non-blocked events are found to be statistically significant by the parameters used within this paper.	107
Table 4.2. Average and standard deviation for blocked and non-blocked 90th percentile heat events in the New York City grid cell of the CM4 historical and RCP 8.5 integrations.....	118
Table 5.1. For each of the three thesis research components, a summary of key takeaways.	134
Table 6.1. Curriculum Map for Mentor Training Workshops.	146

Table 6.2. Regarding outcomes for mentees, superordinate and respective subordinate themes identified from mentee and mentor feedback.....	149
--	-----

List of Figures

	Page
Figure 1.1. (a) Taken from National Weather Service, a schematic of a blocking configuration where contours indicate geopotential height, and the arrows show the geostrophic flow. The H represents the high-pressure blocking anticyclone (b) Geopotential height (contours) and precipitation anomalies (shading) composited over wintertime blocks that fill the area of the magenta box over the North Atlantic Ocean. Computed with ERA5 reanalysis data from 1980-2014.....	1
Figure 1.2. (a) A schematic of the transient eddy reinforcement of blocking. Red represents anticyclonic anomalies, while blue represents cyclonic anomalies. Taken from Hoskins and James (2014).	7
Figure 1.3. For a single 6-hourly snapshot in ERA-Interim reanalysis (a) the 500 hPa geopotential height field, Z_{500} , and (b) Z' as calculated in Eq. 1.9, the anomaly of the normalized Z_{500} field. The white star in (b) indicates the presence of an atmospheric block.	9
Figure 1.4. The blocking climatology during December, January, and February (DJF) in ERA5 reanalysis data. Shading indicates the percentage of DJF timesteps a location is blocked.	12
Figure 1.5. Taken from Dunn-Sigouin and Son 2013. Blocking Frequency (shading) in NCEP-NCAR reanalysis data from 1960-2009 in (a) Winter defined as December, January, and February (DJF), (b) Spring defined as March, April, and May, (c) Summer defined as June, July, and August (JJA), and (c) Autumn defined as September, October, and November.....	13
Figure 1.6. Taken from Nakamura and Huang (2018): Composite longitude-time (i.e., Hovmoller) diagrams of (A) local wave activity, (B) zonal wind, and (C) zonal wave activity flux along 45° for 24 Atlantic blocking events. Day 0 corresponds to the peak of blocking.....	15
Figure 1.7. Taken from Paradise et al. (2019): Using the idealized traffic jam model described in Eq. 1.15, blocked days (prevalence) as a function of (left) stationary wave amplitude, (middle) eddy feedback, and (right) background flow strength....	16

Figure 1.8. Taken from Davini and D'Andrea 2020: Biases in the winter blocking climatology (shading) for the multi model mean in (left) CMIP3, (middle) CMIP5, and (right) CMIP6 models.	17
Figure 1.9. Taken from Woollings et al. 2018: CMIP5 multi-model mean of changes in the blocking climatology between historical and RCP 8.5 integrations using a geopotential height (left) anomaly, (middle) gradient reversal, and (right) hybrid anomaly and gradient reversal metrics. The top panel are for DJF and the bottom are for JJA.	18
Figure 2.1. Surface height (shading) of the idealized model integrations with (a) a single 3 km high Gaussian mountain centered at 45 N, 90E and (b) two 3 km high Gaussian mountains centered at 45 N, 90E and 45 N, 150 W, respectively. The red outlines indicate the block genesis regions described in Table 2.1.	28
Figure 2.2. 500 hPa geopotential height (black contours), 500 hPa geopotential height anomaly (shading), outline of blocked area (red contour), and wave activity flux vectors \vec{W} (black arrows), for the first day of a blocking episode in the aquaplanet run. The black dot inside the block denotes the block centroid. Geopotential height contours are in 100 m intervals. \vec{W} with magnitudes less than $20 \text{ m}^2 \text{ s}^{-2}$ are removed.....	38
Figure 2.3. For cool season blocking events: Block centered composites of positive 500 hPa geopotential height anomalies (solid contours), negative 500 hPa geopotential height anomalies (dotted contours), \vec{W} (arrows), and $\nabla \cdot \vec{W}$ (shading). (a, e, i): Computed with NH blocks over ocean in ERA-Interim. (b, f, j): Computed with SH blocks in ERA-Interim. (c, g, k): Computed with blocks in the aquaplanet integration. (d, h, l) 4 th Row: Computed with blocks in the 3 km single mountain integration. The left, middle, and right columns are composites over the first, strongest, and last timesteps of blocking episodes, respectively. Positive (negative) 500 hPa geopotential height anomaly contours are in 50 m (-10 m) intervals with outer contour 50 m (-30 m). \vec{W} with magnitudes less than $20 \text{ m}^2 \text{ s}^{-2}$ are removed. Latitude and longitude are defined relative to the composite block center.	40

Figure 2.4. (a and b) Left: For 30 cool seasons (Nov.-Mar.) in the aquaplanet, (a) the stationary wave (shading) and storm track (heavy black contours), and (b) the blocking climatology (shading) and $\overline{U250}$ (heavy black contours) for the idealized model aquaplanet integration. (c and d) Right: Blocking climatology (shading) for (c) 100 and (d) 250 cool seasons in the aquaplanet. In (a) storm track contours are in 10 m intervals where the outer contour is 50 m. In (b) $\overline{U250}$ contours are in 5 m/s intervals where the outer contour is 30 m s^{-1} 43

Figure 2.5. (a-b) Left: Cool season stationary wave (shading) and storm track (heavy black contours) for the (a) northern and (b) southern hemispheres in ERA-Interim. Storm track contours are in 10 m intervals where the outer contour is 50 m. (c-d) Right: Cool season blocking climatology (shading) and $\overline{U250}$ (heavy black contours) for the (c) northern and (d) southern hemispheres in ERA-Interim. $\overline{U250}$ contours are in 5 m/s intervals where the outer contour is 10 m s^{-1} 46

Figure 2.6. (a-d) Left: Cool season stationary wave (shading) and storm track (heavy black contours) for the (a) 1 km, (b) 2 km, (c) 3 km, and (d) 4 km mountain height integrations. Storm track contours are in 10 m intervals where the outer contour is 50 m. (e-h) Right: Cool season blocking climatology (shading) and $\overline{U250}$ (heavy black contours) for the (e) 1 km, (f) 2 km, (g) 3 km, and (h) 4 km mountain height integrations. $\overline{U250}$ contours are in 5 m/s intervals where the outer contour is 10 m s^{-1} . Black (white) stippling in (e-h) indicates significantly greater (less) block frequency at nearby gridpoints when compared to a 250-year aquaplanet integration. Pink and black dotted contours represent surface height, where the outer contour is the edge of the land-mask and the inner contours are in 1 km intervals..... 49

Figure 2.7. For the 2-mountain idealized model integration, (a) the cool season stationary wave (shading) and storm track (heavy black contours), and (b) the cool season blocking climatology (shading) and $\overline{U250}$ (heavy black contours). In (a) storm track contours are in 10 m intervals where the outer contour is 50 m. In (b) $\overline{U250}$ contours are in 5 m/s intervals where the outer contour is 10 m s^{-1} . Black (white) stippling in b indicates significantly greater (less) block frequency at nearby gridpoints when compared to a 250-year aquaplanet integration. Pink and black dotted contours represent surface height, where the outer contour is the edge of the 53land-mask and the inner contours are in 1 km intervals. 53

Fig. 2.8. Block duration probability density distributions for the aquaplanet and “East” blocks (defined in table 2.1) in (a) SingleMtn 1 km, (b) SingleMtn 2 km, (c) SingleMtn 3 km, (d) SingleMtn 4 km, and (e) TwoMtn configurations. Thick lines denote the mean probability density distribution for each configuration. Shaded regions bordered by dotted lines outline +/- 1 full standard deviation from the mean.

55

Figure 2.9. For an integration with 1 flat landmass, (a) the cool season stationary wave (shading) and storm track (heavy black contours), and (b) the cool season blocking climatology (shading) and $\overline{U_{250}}$ (heavy black contours). In (a) storm track contours are in 10 m intervals where the outer contour is 50 m. In (b) $\overline{U_{250}}$ contours are in 5 m/s intervals where the outer contour is 10 m s⁻¹. Black (white) stippling in b indicates significantly greater (less) block frequency at nearby gridpoints when compared to a 250-year aquaplanet integration. The pink and black dotted contours represent the outer edge of the land-mask.....

57

Figure 3.1. (a) Blocking climatology (shading), C , for ERA5 averaged over December, January, and February (DJF). Red boxes show the boundaries used to define the Pacific and Atlantic regions. (b) Area-weighted meridional mean of the midlatitude DJF blocking climatology, \tilde{C} , in ERA5, AM4, and CM4. The horizontal red lines denote the Pacific and Atlantic regions. C_0 is the minimum blocking frequency used to define each region.....

69

Fig. 3.2 Case-study example for the first day of an Atlantic blocking episode on 4 February 1983: (a) 6-day high-pass-filtered 250 hPa geopotential height, Z_{250} (shading), and unfiltered 500 hPa geopotential height in meters (contours). (b) Divergence of 6-day high-pass-filtered wave activity flux, $\nabla \cdot \mathbf{W}$ (shading), and 500 hPa geopotential height anomaly as defined by the DS13 block tracking algorithm (contours). In (b), thick (thin dashed) black contours indicate positive (negative) geopotential height anomalies with outer contour 50 m (-50 m) and a 50 m (-50 m) contour interval. Thick white contour in (b) indicates 0 m height anomalies. In (a) and (b) the red contour indicates the blocked region as detected by the DS13 algorithm and black arrows show 6-day high-pass-filtered \mathbf{W}

73

Figure 3.3. (a-b) DJF Stationary wave at 500 hPa (Z_{500}^*) for ERA5 (contours), and the GFDL models (shading): (a) AM4, and (b) CM4. (c-d) Z_{500}^* for ERA5 (contours) and Z_{500}^* in the GFDL models minus reanalysis (shading) for (c) AM4 and (d) CM4. Solid and dashed contours in (a-d) show the positive and negative Z_{500}^* , respectively. The outer contour for the solid (dashed) contours is 25 m (-25 m) and the contour interval is 25 m (-25 m). White stippling in (c-d) denotes regions where Z_{500}^* in the GFDL models differ significantly from ERA5 reanalysis.....

75

Figure 3.4. Z_{500}^* for AM4 (contours) and Z_{500}^* in CM4 minus AM4 (shading). Solid and dashed contours show the positive and negative Z_{500}^* , respectively. The outer contour for the solid (dashed) contours is 25 m (-25 m) and the contour interval is 25 m (-25 m). White stippling denotes regions where Z_{500}^* in the CM4 differs significantly from AM4.

76

Figure 3.5. (a-b) DJF mean zonal wind at 250 hPa, $\overline{U_{250}}$ for ERA5 (contours) and the GFDL models (shading): (a) AM4, and (b) CM4. (c-d) $\overline{U_{250}}$ for ERA5 (contours) and $\overline{U_{250}}$ in the GFDL models minus ERA5 (shading): (c) AM4 and (d) CM4. The outer contour is 8 m s^{-1} , and the contour interval is 8 m s^{-1} . White stippling in (c-d) denotes regions where the $\overline{U_{250}}$ in the GFDL models differs significantly from ERA5 reanalysis.....

77

Figure 3.6. (a) $\overline{U_{250}}$ for AM4 (contours) and $\overline{U_{250}}$ in CM4 minus AM4 (shading). The outer contour is 8 m s^{-1} , and the contour interval is 8 m s^{-1} . White stippling indicates regions where $\overline{U_{250}}$ in CM4 differs significantly from AM4. (b-c) DJF zonal mean zonal wind, $[\bar{U}]$, for ERA5 (contours) and DJF zonal mean zonal wind for (b) AM4 and (c) CM4 minus ERA5 (shading). Solid (dashed) contours in (b-c) indicate positive (zero and negative) zonal wind values with outer contour 5 m s^{-1} (0 m s^{-1}) and contour interval 5 m s^{-1} (-5 m s^{-1}).....

79

Figure 3.7. (a) Sea surface temperature (SST) in AM4 (contours) and difference in SST between CM4 and AM4 (shading). The outermost contour is 30°C and the contour interval is 5°C . (b-c) Negative of the meridional gradient of SST (shading) in (b) AM4 and (c) CM4. (d) Negative meridional gradient of SST in AM4 (contours) and difference between CM4 and AM4 (shading). The outer contour is $0^\circ \text{ C km}^{-1}$ and the contour interval is $.01^\circ \text{ C km}^{-1}$

80

Figure 3.8. (a-b) DJF blocking climatology for ERA5 (contours) and in the GFDL models (shading): (a) AM4, and (b) CM4. (c-d) Blocking climatology for ERA5 (contours) and GFDL models minus ERA5 (shading): (c) AM4 and (d) CM4. The outer contour and contour interval are both 2 %. White stippling in (c-d) denotes regions where the blocking climatology in the GFDL models differs significantly from ERA5 reanalysis.....

81

Figure 3.9. (a) Blocking climatology for AM4 (contours) and CM4 minus AM4 (shading). Magenta stippling indicates regions where the blocking climatology in CM4 differs significantly from AM4. (b) Standard deviation of the blocking climatology in AM4 (contours) and CM4 (shading). The outer contours and contour interval are both 2 % in (a) and (b).

83

Figure 3.10. (a, b) For the block onset phase, block-centered composites of unfiltered 500 hPa geopotential height (m) (contours) and 30-day low-pass-filtered 250 hPa zonal wind, U_{250} (shading) for (a) Pacific and (b) Atlantic blocks in ERA5. (c-f) For the block onset phase, block-centered composites of unfiltered 500 hPa geopotential height (contours) and difference between block-center composited U_{250} in the GFDL models and ERA5 (shading). (c-d) Computed using AM4 for (c) Pacific and (d) Atlantic blocks. (e-f) Computed using CM4 for (e) Pacific and (f) Atlantic blocks. Magenta stippling in (c-f) indicate significant differences between the corresponding GFDL model and ERA5.

87

Figure 3.11. (a, c, e) For the onset phase of Pacific blocking events, block-centered composites of positive 500 hPa geopotential height anomalies (solid contours), negative 500 hPa geopotential height anomalies (dashed contours), column integrated wave activity flux, \mathbf{W} (arrows), and $\nabla \cdot \mathbf{W}$ (shading) for (a) ERA5, (c) AM4, and (e) CM4. (b, d, f) As in (a, c, e) but for Atlantic blocks in (b) ERA5, (d) AM4, and (f) CM4. Positive (negative) geopotential height contours have an outer contour of 50 m (-20 m) and contour interval of 50 m (-20 m). \mathbf{W} is calculated using 6-day high-pass-filtered fields. Vectors with magnitudes less than $5 \cdot 10^4 \text{ kg m}^{-2} \text{ s}^{-2}$ are masked. Magenta stippling indicates significant differences in $\nabla \cdot \mathbf{W}$ between (b) ERA5's Pacific and Atlantic blocks, and (c-f) the corresponding GFDL model and ERA5.....

89

Figure 3.12. (a, c, e) For the strongest days of Pacific blocking events, block-centered composites of positive 500 hPa geopotential height anomalies (solid contours), negative 500 hPa geopotential height anomalies (dashed contours), column integrated wave activity flux, \mathbf{W} (arrows), and $\nabla \cdot \mathbf{W}$ (shading) for (a) ERA5, (c) AM4, and (e) CM4. (b, d, f) As in (a, c, e) but for Atlantic blocks in (b) ERA5, (d) AM4, and (f) CM4. Positive (negative) geopotential height contours have an outer contour of 50 m (-20 m) and contour interval of 50 m (-20 m). \mathbf{W} is calculated using 6-day high-pass-filtered fields. Vectors with magnitudes less than $5 \cdot 10^4 \text{ kg m}^{-2} \text{ s}^{-2}$ are masked. Magenta stippling in (c-f) indicates significant differences in $\nabla \cdot \mathbf{W}$ between the corresponding GFDL model and ERA5.

91

Figure 4.1. Percent of heat extreme days that include blocking (shading), $P(B|H)$, for (a) 70th, (b) 80th, (c) 90th, and (d) 99th percentile heat events. Contours indicate the percent of all summer days that are blocked, $P(B)$. The outer contour and contour interval is 5 %. Stippling indicates significant differences between $P(B|H)$ and $P(B)$

104

Figure 4.2. $P(H B)$, the percent of blocked days that also include a (a) 70 th , (b) 80 th , (c) 90 th , and (d) 99 th percentile heat event.....	106
Figure 4.3. Temperature anomalies for non-blocked 90 th percentile heat events in New York City (contours) and difference between blocked and non-blocked events (shading) composited (a) one day before event onset, (b) one day after event onset, and (c) 3 days after event onset. The outer contours and contour interval are 1 K. ..	107
Figure 4.4. (a-c) Three days before the onset of blocked 90th percentile heat extremes in the grid-cell containing New York City, composited (a) 2 m temperature anomaly (shading) and blocking probability, $P(B)$ (contours), (b) Z_{500} (contours) and anomalous Z_{500} (shading), and (c) SLP (contours) and anomalous SLP (shading). Panels (d-f) and (g-i) are as in (a-c) but instead composited one day before onset and one day after event onset, respectively. The outer contour and contour interval in (a), (d), and (g) is 20 %.....	108
Figure 4.5. (a-c) Three days before the onset of non-blocked 90 th percentile heat extremes in New York City, composited (a) 2 m temperature anomaly (shading), (b) Z_{500} (contours) and anomalous Z_{500} (shading), and (c) SLP (contours) and anomalous SLP (shading). Panels (d-f) and (g-i) are as in (a-c) but instead composited one day before onset and one day after event onset, respectively.....	109
Figure 4.6. (a-b) For block associated heat events in the grid-cell containing New York City, composited 1000 hPa temperature budget terms: (a) Horizontal and vertical advection terms (b) Adiabatic advection terms, A , plus all other terms, Q . (c-d) As in (a-b) but for heat events not associated with blocking.	112
Figure 4.7. (a) Mean 250 hPa zonal wind, $\overline{U_{250}}$, for June, July, and August from 1980-2014 in ERA5 reanalysis (contours) and CM4 historical simulation (shading). (b) CM4 historical $\overline{U_{250}}$ subtracting ERA5 reanalysis (shading). $\overline{U_{250}}$ in ERA5 reanalysis (contours). (c) Percent of blocked June, July, and August days, $P(B)$, from 1980-2014 in ERA5 reanalysis (contours) and CM4 historical integration (shading). (d) CM4 historical $P(B)$ subtracting ERA5 reanalysis (shading). $P(B)$ in ERA5 reanalysis (contours). Outer contour and contour interval in (a-b) is 5 m/s. Outer contour and contour interval in (c-d) is 5 %.	113
Figure 4.8. (a-c) In ERA5 reanalysis, percent of heat extreme days that include blocking (shading), $P(B H)$, for (a) 80 th , (b) 90 th , (c) and 99 th percentile heat events. (d-f) As	115

Figure 4.9. (a) Mean 250 hPa zonal wind, $\overline{U_{250}}$, for all June, July, and August in CM4 historical integration (contours) and CM4 RCP 8.5 simulation (shading). (b) CM4 RCP 8.5 $\overline{U_{250}}$ subtracting CM4 historical (shading). $\overline{U_{250}}$ in CM4 historical (contours). (c) Difference in P(B) for CM4 RCP 8.5 subtracting CM4 historical (shading). P(B) in CM4 historical (contours). (d-e) Difference in P(B|H), CM4 RCP 8.5 subtracting CM4 historical (shading) for (d) 90th, and (e) 99th percentile heat events. Outer contour and contour interval in (a-b) is 5 m/s. Outer contour and contour interval in (c) is 5 %.....

116

Figure 4.10. (a) Composite 2 m temperature anomaly for one day after the onset of all 90th percentile New York City heat events in CM4's historical integration (contours). The outer contour and contour interval is 1 K. Difference in 2 m temperature anomaly composite one day before all 90th percentile New York City heat events, CM4 RCP 8.5 subtracting CM4 historical integration (shading). Blue stippling indicates significant differences. (b-c) Mean 2 m temperature for June, July August in (b) CM4 historical integration from 1980-2014, and (c) CM4 RCP 8.5 integration from years 2065-2099. (d) Difference between (c) and (b), CM4 RCP 8.5 subtracting CM4 historical integration.

117

Figure 5.1. A schematic of where blocking is most ubiquitous. H represents the high-pressure anomaly of the stationary wave. In reality blocking occurs near the high-pressure stationary wave anomaly and end of the storm track.

127

Figure 5.2. Modified version of Fig. 5.1 to explicitly include the jet. This schematic depicts an idealization of where blocking is most ubiquitous relative to the jet, storm track, and high-pressure stationary wave anomaly (H).

130

Figure 6.1. Schematic of the multi-level group mentoring model used by the National Society of Black Physicists and Harlem Gallery of Science Mentoring Program. MS denotes middle school students; HS denotes high school students.....

141

Figure 6.2. Mentee and mentor races and ethnicities by percentages.....

143

Chapter 1

Introduction

1.1 What is Atmospheric Blocking?

One of the first things we do in the morning is check the weather. Is it going to rain today, or will it be bright and sunny? We plan our whole day around what the weather forecast says. Daily weather conditions in the midlatitudes are largely influenced by specific geophysical fluid phenomena such as storms, or what this thesis focuses on, atmospheric blocking.

Atmospheric blocks are large, quasi-stationary high-pressure systems that influence the atmosphere from several days up to several weeks (Rex 1950a, b). The presence of blocks often leads to persistent local weather patterns. Figure 1.1a shows a schematic of a blocking configuration.

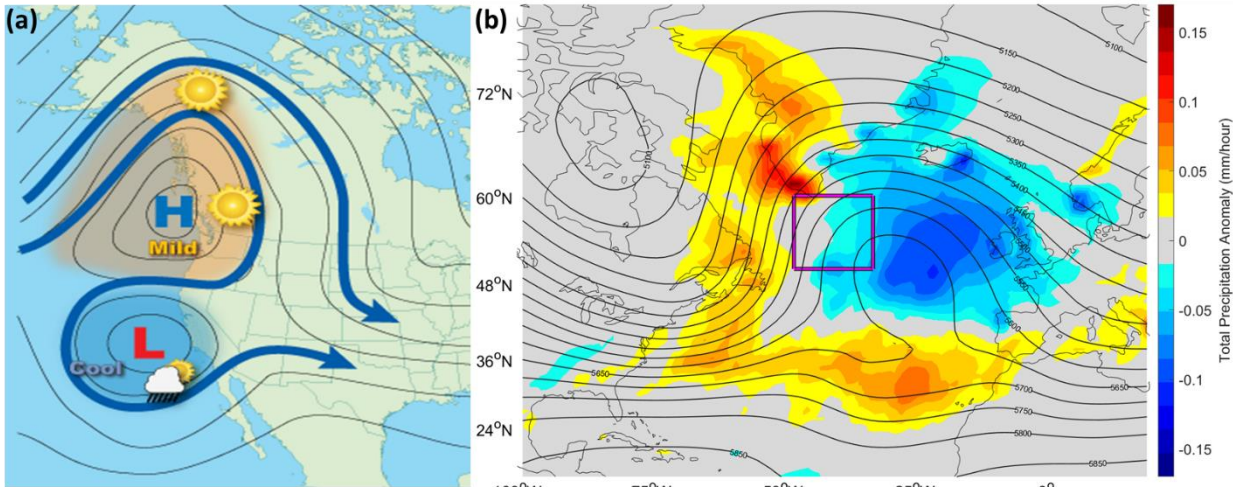


Figure 1.1. (a) Reproduced from National Weather Service, a schematic of a blocking configuration where contours indicate geopotential height, and the arrows show the geostrophic flow. The H represents the high-pressure blocking anticyclone (https://www.weather.gov/images/jetstream/constant/rex_wx.png). (b) Geopotential height (contours) and precipitation anomalies (shading) composited over wintertime blocks that fill the area of the magenta box over the North Atlantic Ocean. Computed with ERA5 reanalysis data from 1980-2014.

configuration. The high-pressure anticyclone is typically what is considered the block. Note, however, that a larger scale flow pattern is also present, where the high-pressure is flanked equatorward by low-pressure. The entire disturbance acts to deflect and split the typically eastward flow.

Fig. 1.1b shows a composite of blocking events from observations. Blocks usually appear as ridges (Fig. 1.1b) or cut off highs in upper-tropospheric geopotential height contours. Upstream and equatorward of the block one finds enhanced precipitation, while within the block precipitation is suppressed and temperatures are anomalously warm (e.g., Pfahl and Wernli 2012). Furthermore, blocks have been associated with deadly hazards such as heat waves (Horton 2016; Dong et al. 2018; Chan et al. 2019), cold spells (Sillman et al. 2011), and persistent strong storm surge events (Booth et al. 2021). Yet despite the danger blocks pose, many of their fundamental physical aspects are not fully understood and newest generation of GCM's still contain notable errors in their representation of blocks.

This thesis investigates the climatology and dynamics of atmospheric blocking and associated weather extremes. Through original research, this is carried out using a hierarchy of general circulation models configured with various climate forcing conditions. Chapter 1 contains an overview of blocking. This includes fundamental fluid and climatological aspects of blocking, as well as its simulation in climate models. Then, Chapters 2-4 each focus on individual research components that have been published, in revision, or prepared for publication:

1. Atmospheric Blocking in an Aquaplanet and the Impact of Orography (Chapter 2;
published in *Weather and Climate Dynamics*)
2. Blocking and General Circulation in GFDL Comprehensive Climate Models (Chapter
3; in revision in *Journal of Climate*)

3. Connections Between Atmospheric Blocking and Heat Extremes in Current and Possible Future Climates (Chapter 4; to be submitted to GRL)

Chapter 5 contains a summary and concluding discussion of the weather and climate physics portion of this thesis.

The final chapter, Chapter 6, is a self-contained chapter with original research on the effects of mentorship on adolescents of color from underserved communities. This component focuses primarily on scholarly work in STEM education and diversity. For this, college student mentors from the National Society of Black Physicists and Harlem Gallery of Science mentoring program guide youth throughout two 12-week semesters. Interpretive phenomenological analysis (IPA) is used to extract superordinate and subordinate themes of adolescent accounts within the program.

1.2 Geophysical Fluid Fundamentals of Blocking

The name block comes from the fact that these systems “block” the westerly flow and thus the eastward progression of weather systems. The influence of atmospheric blocking has been noted since the early 20th century (Garriot 1904), characterized by slowly propagating surface high pressure systems. The earliest studies on the dynamical and climatological features of blocking, however, did not begin until around the mid-20th century.

In 1950, work done by Rex was some of the first attempts to understand the fundamental physics and statistics of blocking. His work began to make the connection between blocking and Rossby waves (1950a), as well as describe the regions where blocking occurred most often (1950b). Since then, numerous studies (e.g., Woollings et al. 2018; Lupo 2021) have investigated many aspects of blocking, however, a general physical theory of blocking from onset through decay remains to be formulated.

To build up a physical understanding of blocking, Rossby waves are a great starting point. Rossby waves have been found to be deeply related to blocking through processes such as wavebreaking (Pelly and Hoskins 2003; Masato et al. 2012) and transient eddy momentum flux convergence (Shutts 1983). Due these connections, let us take a moment to describe some basic aspects of Rossby wave theory.

1.2.a Rossby Waves in the Atmosphere

In a fluid, potential vorticity (PV) is a variable this is proportional to the dot product of vorticity and stratification. PV is useful for studying midlatitude dynamics because it is conserved in the absence of diabatic and frictional processes. In addition, through PV inversion, one can straightforwardly obtain the horizontal winds. Herein, we will consider the quasigeostrophic potential vorticity, which is PV for a flow with the following properties: (1) Vertical length scales that are very small compared to horizontal length scales, (2) Coriolis and pressure gradient forces are nearly, but not exactly in balance, and (3) the Coriolis force varies linearly with latitude (beta-plane approximation). The conservation of quasigeostrophic potential vorticity (QGPV) on a beta-plane can be expressed in terms of the stream function, ψ :

$$\frac{D_h}{Dt} (\nabla^2 \psi + f_0 + \beta y + \frac{f_0^2}{N^2} \left(\frac{\partial^2}{\partial z^2} (\psi) \right)) = 0 \text{ (Eq. 1.1)}$$

Here, the material derivative in the horizontal plane is $\frac{D_h}{Dt} = \frac{\partial}{\partial t} + u \frac{\partial}{\partial x} + v \frac{\partial}{\partial y}$, where u and v are the zonal and meridional winds. $f_0 + \beta y$ is the planetary vorticity in the beta plane approximation where f_0 is the Coriolis parameter, $f = 2\Omega \sin \phi$ at some reference latitude, ϕ_0 , Ω is the angular velocity of earth, and $\beta = \frac{df}{dy}|_{\phi_0}$. N is the Brunt–Väisälä frequency, a measure of vertical stability.

We then decompose the streamfunction and wind into a mean state plus some small perturbation:

$$\psi(x, y, z, t) = \bar{\psi} + \psi'(x, y, z, t) \text{ (Eq. 1.2)}$$

$$u(x, y, z, t) = \bar{u} + u'(x, y, z, t) \text{ (Eq. 1.3)}$$

$$v(x, y, z, t) = \bar{v} + v'(x, y, z, t) \text{ (Eq. 1.4)}$$

Here overbars indicate the mean state and primes indicate perturbations. Inserting equations 1.2-1.4 into equation 1.1 and keeping only terms that are linear in the perturbation fields yields the linearized QGPV equation (Eq. 1.5). For simplicity's sake, we take the mean flow to be purely zonal, i.e., $\bar{v} = 0$, this yields:

$$\psi'_{xxt} + \psi'_{yyt} + \frac{f_0^2}{N^2} \psi'_{zzt} + v'\beta + \bar{u}(\psi'_{xxx} + \psi'_{yyx} + \frac{f_0^2}{N^2} \psi'_{zzx}) = 0 \text{ (Eq. 1.5)}$$

One solution to this equation is that of two-dimensional plane waves, $\psi' = e^{i(kx+ly-\omega t)}$.

Inserting this solution into Eq. 1.5 yields the following dispersion relationship:

$$\omega = \frac{\bar{u}k(k^2+l^2)-k\beta}{k^2+l^2} \text{ (Eq. 1.6)}$$

Calculating the zonal phase speed, $c_p = \frac{\omega}{k}$ we arrive at:

$$c_p = \bar{u} - \frac{\beta}{k^2+l^2} \text{ (Eq. 1.7)}$$

From this we see that zonal phase speed vanishes when $\bar{u} = \frac{\beta}{k^2+l^2}$. This is the condition for stationary Rossby waves (excluding meridional propagation). Though various simplifying assumptions were made along the way, this relation is what we observe in reality. Atmospheric blocking, for example, is a multiscale interaction of Rossby waves. In generating blocks, low wavenumber, stationary or retrograding Rossby waves are amplified by transient, high-frequency wave disturbances (Tung and Lindzen 1979).

1.2.b Building and Maintaining Blocks

Blocks typically begin with a poleward extrusion of subtropical air, which is often contained in the crest of a low-frequency Rossby wave packet. This poleward extrusion features anomalously anticyclonic, high-pressure, low PV air and can be recognized on maps of pressure or geopotential as large-scale ridges or cut off highs. If this high-pressure/low-PV anomaly remains quasi-stationary for multiple days, then it is typically what is referred to as the block.

The amplification of a ridge into a mature block can occur through several pathways. In simplified systems, blocks can form solely through the interaction of planetary scale waves with the mean flow or through the interaction of multiple modes (Charney and Devore 1979; Reinhold and Raymond 1982; Brunet 1994). In reality however, transient synoptic scale eddies also play a prominent role. This can occur through both dry and moist processes (Shutts 1983; Yamazaki and Itoh 2009; Steinfeld and Pfahl 2019).

One way of amplifying and sustaining a blocking system is through the absorption of anticyclonic air brought in by transient, eastward progressing eddies (Shutts 1983; Yamazaki and Itoh 2009). This is a dry, mechanical process that occurs even in the absence of moisture. Fig. 1.2 shows a schematic of this process. Here, the blocking dipole consists of a positive height anomaly (i.e., anticyclonic) flanked on its equatorward side by a negative height anomaly (i.e., cyclonic). An incident wave propagates towards the block. As the incident wave approaches the block, it is strained, stretched, and then absorbed by the block and accompanying cyclone according to polarity.

Hoskins and James (2014)* Chap. 17.5: a diagnostic interpretation of observed blocks

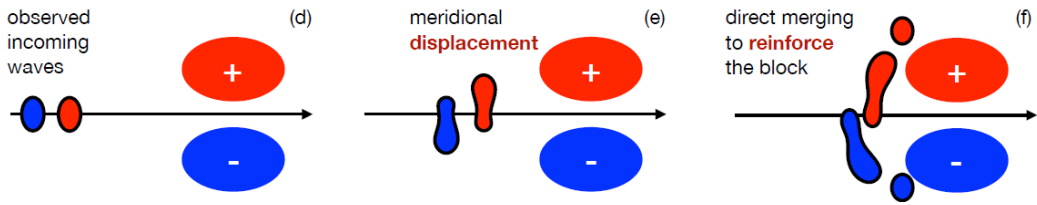


Figure 1.2. (a) A schematic of the transient eddy reinforcement of blocking. Red represents anticyclonic anomalies, while blue represents cyclonic anomalies. Reproduced from Hoskins and James (2014).

To quantify this forcing, the convergence of wave-activity flux, \mathbf{W} (Eq. 1.8), can be utilized.

\mathbf{W} is the pseudo-momentum of Rossby waves. Convergence of \mathbf{W} indicates the absorption of waves and tends to decrease zonal flow, reinforcing blocking (Takaya and Nakamura 2001):

$$\mathbf{W} = \frac{p \cos \phi}{2|\mathbf{u}|} \begin{pmatrix} \bar{u} \left(v'^2 - \frac{\Phi' \partial v'}{f \partial x} \right) + \bar{v} \left(-u' v' - \frac{\Phi' \partial v'}{f \partial y} \right) \\ \bar{u} \left(-u' v' + \frac{\Phi' \partial u'}{f \partial x} \right) + \bar{v} \left(u'^2 + \frac{\Phi' \partial u'}{f \partial y} \right) \end{pmatrix} \quad (\text{Eq. 1.8}).$$

Here, p is the pressure, Φ is the geopotential height, and the horizontal background flow is $\bar{\mathbf{u}} = (\bar{u}, \bar{v})$, and all other variables were defined after Eq. 1.1. In Chapters 2 and 3 $\nabla \cdot \mathbf{W}$ will be used to assess how well GCM's capture the dynamics of blocking.

Another means to amplify and reinforce blocks is through moist processes (Steinfeld and Pfahl 2019; Steinfeld et al. 2020). For this, ascending air streams typically associated with the warm sector of upstream cyclones are warmed by latent heating associated with water vapor –so-called “warm conveyor belts”. A decreasing vertical gradient in the latent heating generates anomalously anticyclonic PV, and therefore portions of the ascending air are anticyclonic relative to their surroundings. If this air reaches the region of the block, it can act to reinforce them. Pfahl et al. (2015) found 30-45% of parcels within blocking anticyclones experienced warm ascension prior to being absorbed, emphasizing the relative importance of diabatic processes in the onset and maintenance of blocking.

1.3 Tracking Blocks

1.3a Background

Blocking has a strong influence on many fluid properties, and thus, throughout the years numerous methods to identify and track blocks have been implemented (Dole and Gordon 1983; Tibaldi and Molteni 1990; Barnes et al. 2011). These methods utilize different fields such as geopotential height (Dole-Gordon 1983), potential temperature (Pelly and Hoskins), zonal wind (Barnes et al. 2011), or local wave activity (Nakamura and Huang 2018). Most blocking events with significant amplitude and spatial scale, however, are captured by all fields (Barnes et al 2011).

The block tracking metric as described by Dole and Gordon (1983) is one of the most commonly used metrics. It searches for high amplitude, persistent positive anomalies in the 500 hPa geopotential height field. Some disadvantages of this method are that it captures events that do not necessarily halt the zonal flow and it requires a reference climatology. Circumventing these issues, the method of Tibaldi and Molteni (1990) is another widely used metric. This metric looks for a reversal of the meridional gradient of Z_{500} , and thus a reversal of quasigeostrophic zonal flow. But even this metric has its drawbacks: it only describes blocks as a function of longitude without any meridional consideration and can be extremely sensitive to mean state biases (Scaife et al. 2011).

For this thesis the hybrid block tracking metric as described in Dunn-Sigouin and Son 2013 (DS13, hereinafter) is used. The DS13 metric is a hybrid of the Dole-Gordon (1983) and Tibaldi-Molteni (1990) metrics in the sense that it looks for strong, positive Z_{500} anomalies that also reverse the meridional gradient of Z_{500} . This metric still captures high-amplitude events, but also those that simultaneously halt or reverse the midlatitude westerlies.

What follows are some details of the tracking algorithm, but a more complete description can be found in DS13. A Z_{500} based metric is chosen because Z_{500} is often more readily available from model output as opposed to other fields such as PV or local wave activity.

1.3b Geopotential Height Anomalies

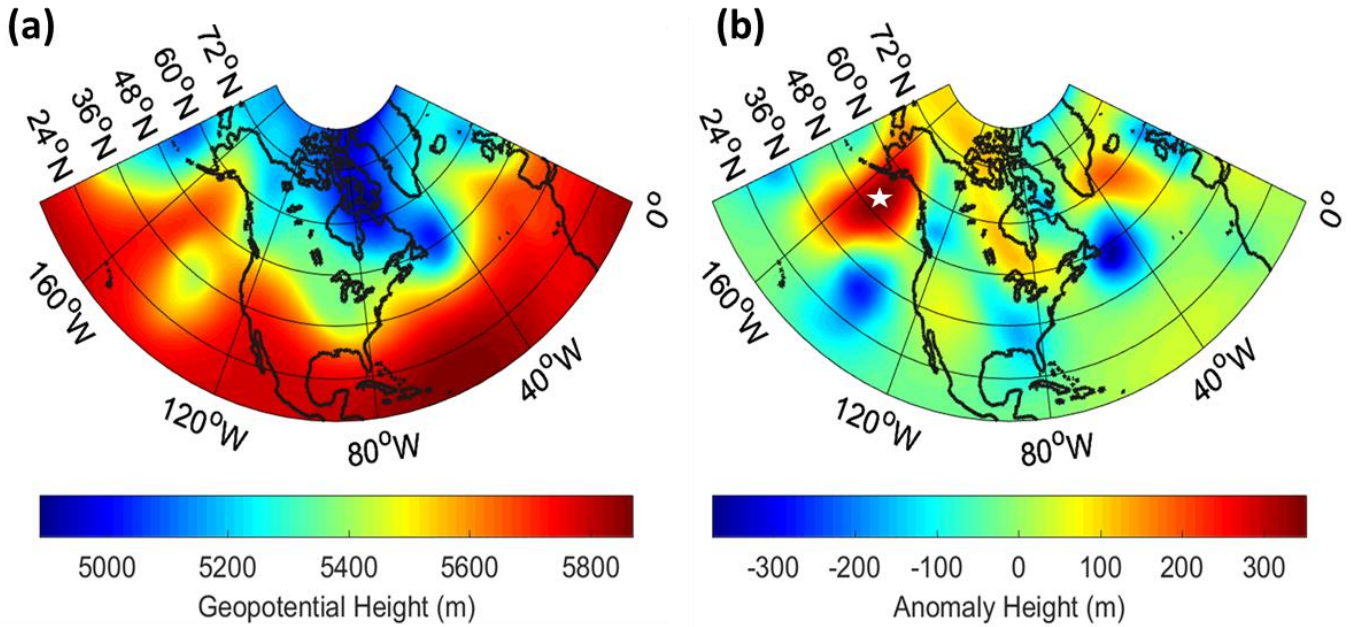


Figure 1.3. For a single 6-hourly snapshot in ERA-Interim reanalysis (a) the 500 hPa geopotential height field, Z_{500} , and (b) Z' as calculated in Eq. 1.9, the anomaly of the normalized Z_{500} field. The white star in (b) indicates the presence of an atmospheric block.

The tracking algorithm begins by calculating anomalies, Z' (Fig. 1.3), in the 500-hPa geopotential height, Z . Anomalies are normalized by the sine of latitude. The anomaly calculation in DS13 is a slight modification of the work by Sausen et al. (1995). At each gridpoint:

$$Z'(t) = Z(t) - \bar{Z}(t) - \hat{Z}(\nu) \quad (\text{Eq. 1.9})$$

Here, \bar{Z} is the running annual mean and \hat{Z} is the climatological mean seasonal cycle (after removing the running annual mean). t is the time dimension of the entire data series with number of elements equal to K , the number of years, times N , the number of timesteps per year. ν is a subspace within

t corresponding to each day of the year. To effectively detrend the data and reduce the effects of interannual variability, $\bar{Z}(t)$ is defined as:

$$\bar{Z}(t) = \begin{cases} \bar{Z}\left(\frac{1}{2}N + 1\right), & \text{for } 1 \leq t \leq \frac{1}{2}N \\ \frac{1}{N+1} \sum_{\tau=t-\frac{N}{2}}^{t+\frac{N}{2}} Z(\tau), & \text{for } \frac{1}{2}N + 1 \leq t \leq KN - \frac{1}{2}N - 1 \text{ (Eq. 1.10)} \\ \bar{Z}\left(KN - \frac{1}{2}N + 1\right), & \text{for } KN - \frac{1}{2}N \leq t \leq KN \end{cases}$$

Next, to calculate \hat{Z} , the running monthly mean of the anomaly with respect to the annual mean, Z^* , is calculated:

$$Z^*(t) = \begin{cases} Z^*\left(\frac{1}{2}M + 1\right), & \text{for } 1 \leq t \leq \frac{1}{2}M \\ \frac{1}{M+1} \sum_{\tau=t-\frac{M}{2}}^{t+\frac{M}{2}} Z(\tau) - \bar{Z}(\tau), & \text{for } \frac{1}{2}M + 1 \leq t \leq KN - \frac{1}{2}M - 1 \text{ (Eq. 1.11)} \\ Z^*\left(KN - \frac{1}{2}M + 1\right), & \text{for } KN - \frac{1}{2}M \leq t \leq KN \end{cases}$$

Here, M is the number of timesteps per month. \hat{Z} is then calculated spanning the time interval $1 \leq \nu \leq N$, yielding a single value for each day of the year, i.e., \hat{Z} is the climatology of Z^* :

$$\hat{Z}(\nu) = \frac{1}{K} \sum_{l=1}^K Z^*(N(l-1) + \nu) \text{ (Eq. 1.12)}$$

1.3c Block Detection and Tracking

The Z' field is then used to detect and track blocks. Contiguous positive anomalies in Z' are first identified, then several restrictions are imposed.

1. Anomalies at each gridpoint must have an amplitude of at least A . A is calculated as 1.5 standard deviations in Z' from 30° - 90° latitude for a 3-month window centered on given month. Thus A has a single value corresponding to each month of the year.
2. Contiguous anomalies must have an area of at least $2.5 \times 10^6 \text{ km}^2$.
3. Contiguous anomalies must contain a meridional gradient reversal of Z .

4. Quasi-stationary condition: the region that satisfies conditions 1-3 must have a 50% area overlap every 2 days.

5. Satisfaction of the above criteria for at least 5 days.

The meridional gradient reversal condition (criteria 3 above) is as follows. On the equatorward flank of the anomaly maximum, the height difference, $D(i)$, is defined as the maximum value of:

$$Z_{500}(i, j^*) - Z_{500}(i, j^* - \Delta\phi) \text{ (Eq. 1.13)}$$

This is on the interval $j - \frac{\Delta\phi}{2} \leq j^* \leq j + \frac{\Delta\phi}{2}$, where i and j are longitudinal and latitudinal indices, respectively, and $\Delta\phi=15^\circ$. For the reversal to be satisfied, $D(i^*)$ must be negative on the interval $i - \frac{\Delta\lambda}{2} \leq i^* \leq i + \frac{\Delta\lambda}{2}$ for any longitude. Here, $\Delta\lambda=10^\circ$.

An example of a block can be seen in Fig. 1.3. In the Z_{500} field (Fig. 1.3a) near where the block is, a strong ridge is flanked by a cutoff low. In the anomaly field (Fig. 1.3b) we see this manifested as a characteristic high-low dipole in the meridional direction. One caveat to this metric is that the amplitude and area thresholds were developed in a way tuned to identify winter blocking. Summer blocks, however, typically exhibit weaker geopotential height anomalies and smaller areas (Nabizadeh et al. 2021)). With this in mind, we will explore summer blocking more in Chapter 4, where retuned amplitude and area thresholds (Chan et al. 2019) are employed to better capture summer blocking.

1.4 Blocking: Observation and Simulation in Current and Future Climates

1.4a Blocking in

Observations

For the Northern Hemisphere, blocking is most ubiquitous near two regions: in the Northeastern Pacific just south of the Aleutian Islands, and in the Northeastern Atlantic southeast of Greenland. Herein these regions will be referred to as the Pacific and Atlantic blocking maxima, respectively. Fig 1.4 shows the blocking climatology for winter

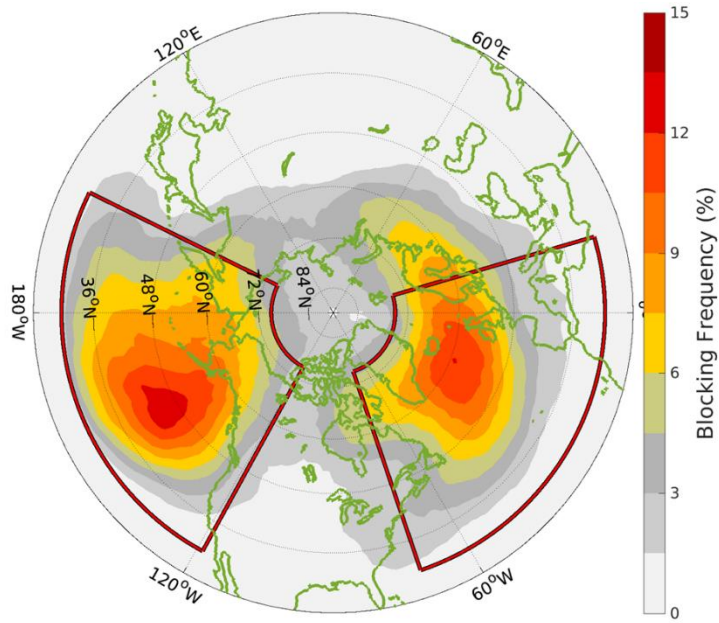


Figure 1.4. The blocking climatology during December, January, and February (DJF) in ERA5 reanalysis data. Shading indicates the percentage of DJF timesteps a location is blocked.

defined as December, January, and February in ERA5 reanalysis data. The red boxes outline the blocking maxima.

The Pacific maximum peaks near the eastern edge of the Pacific Ocean basin, extending west over the central Pacific poleward of the jet and storm track exit regions (Narinesingh et al. 2020). The Atlantic maximum peaks southeast of Greenland and extends eastward into Europe.

The climatology of blocking exhibits a seasonal cycle (Fig. 1.5a). During the winter blocking is most ubiquitous and during the summer blocking minimizes (Fig. 1.5c). This is seemingly counterintuitive; despite the zonal background flow carrying the most momentum during Winter, it is the season that contains the most blocking. Clearly, other factors beyond the zonal flow play a role in the formation and maintenance of blocking.

Why blocking occurs where it does, and the seasonality of blocking are two features of the blocking climatology that are still not well understood. The theoretical work of Huang and Nakamura (2016; 2017; Nakamura and Huang 2018) provides some insight. For their analysis, they use the local wave activity (LWA), which measures the waviness of PV contours and serves as a diagnostic for the presence and amplitude of Rossby waves. In their formalism, blocking is manifested as an accumulation of LWA. The conservation of column integrated local wave

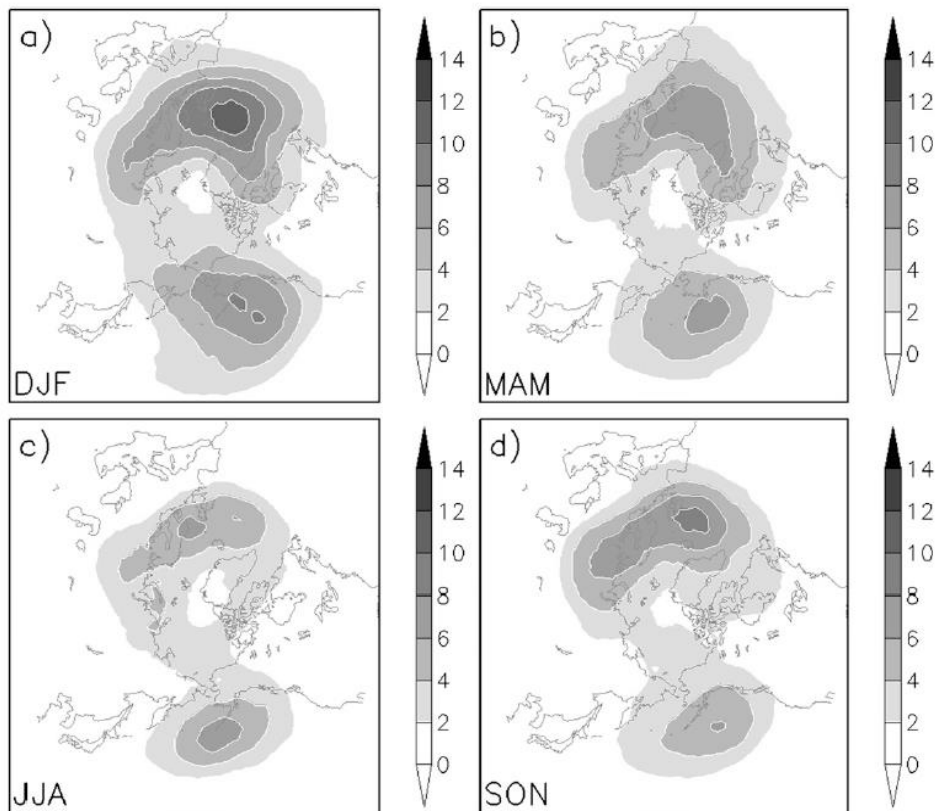


Figure 1.5. Reproduced from Dunn-Sigouin and Son 2013. Blocking Frequency (shading) in NCEP-NCAR reanalysis data from 1960-2009 in (a) Winter defined as December, January, and February (DJF), (b) Spring defined as March, April, and May, (c) Summer defined as June, July, and August (JJA), and (c) Autumn defined as September, October, and November.

activity, A , can be written approximately as:

$$\frac{\partial}{\partial t} \langle A \rangle \cos \phi_0 \approx -\frac{1}{a} \frac{\partial F_\lambda}{\partial \lambda} + \frac{1}{a \cos \phi_0} \frac{\partial}{\partial \phi'} \langle u' v' \cos^2(\phi_0 + \phi') \rangle + \frac{f \cos \phi_0}{H} \left(\frac{v' \theta'}{\partial \hat{\theta} / \partial z} \right) \Big|_{z=0} + Res.$$

(Eq. 1.14)

Here ϕ_0 is a reference latitude, ϕ' is the departure from ϕ_0 , a is the radius of the planet, and F_λ is the local wave activity flux in the zonal direction, λ . H is the atmospheric scale height, θ' is the potential temperature anomaly, and $\hat{\theta}$ is the area-weighted average of potential temperature over the entire hemisphere. Angle brackets indicate column integrated values.

The first term on the left side of Eq. 1.14 is the local wave activity tendency. On the right, the first term is the convergence of local wave activity. The second and third terms are eddy forcing terms corresponding to meridional eddy momentum flux divergence and low-level eddy meridional heat flux, respectively. *Res.* represents residual terms such as dissipation.

Some simplifying assumptions are imposed on Eq. 1.14. First, F_λ is assumed to be independent of z and y . Next, we take $F_\lambda \approx A(\bar{u} + u' + c_g)$, where c_g is the group velocity of Rossby waves. Finally, a geostrophic approximation is made to relate the eddy zonal wind to transient, $\hat{A}(x, t)$, and stationary wave activity, $A_0(x, t)$: $u' \approx -\alpha(A_0 + \hat{A})$. Where alpha is some scaling constant. The total local wave activity is then: $A(x, t) = A_0(x) + \hat{A}(x, t)$

Eq. 1.14 can then be cast into a form resembling Burger's equation:

$$\frac{\partial}{\partial t} \hat{A}(x, t) = -\frac{\partial}{\partial x} [(u_0 - 2\alpha A_0(x) + c_g) \hat{A} - \alpha \hat{A}^2] + S - \frac{\hat{A}}{\tau} + D \frac{\partial^2 \hat{A}}{\partial x^2} \quad (\text{Eq. 1.15})$$

S now represents the original eddy forcing terms in Eq. 1.14. The second to last term on the right-hand side is a damping term, and the last is a diffusion term; these terms can represent the *Res.* term in Eq. 1.14.

Eq. 1.15 is a simplified and idealized equation for local wave activity and its flux. This equation can be considered using the analogy of traffic flow, where a buildup or “traffic jam” in A is representative of blocked flow. This can be visualized in Fig. 1.6. In the region where A builds up and maximizes over time (Fig. 1.6a), there is a minimum in zonal flow (1.6b) and zonal wave activity flux is impeded (Fig. 1.6c).

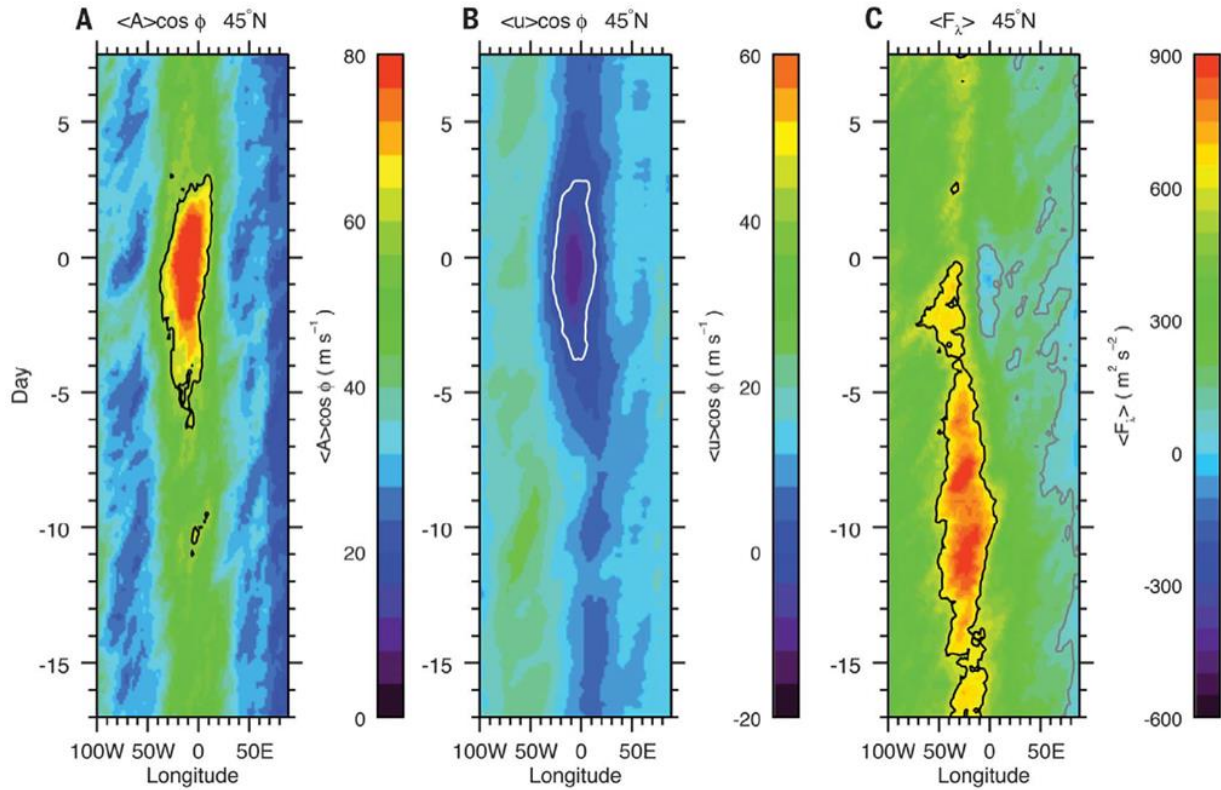


Figure 1.6. Reproduced from Nakamura and Huang (2018): Composite longitude-time (i.e., Hovmöller) diagrams of (A) local wave activity, (B) zonal wind, and (C) zonal wave activity flux along 45° for 24 Atlantic blocking events. Day 0 corresponds to the peak of blocking.

Although Eq. 1.15 is highly idealized, it is physically consistent with reality and useful in developing some dynamical intuition of blocking. This idealized traffic jam model explicitly contains the stationary wave, A_0 , eddy forcing, S , and zonal background flow, u_0 . Paradise et al.

(2019) utilized this formalism and found that the amount of blocking increases for stronger stationary waves and eddy forcing but decreases for stronger zonal background flows (Fig. 1.7).

The results of Paradise et al. (2019) perhaps provide some insight into questions regarding the spatial distribution and seasonality of the blocking climatology. Blocking mostly occurs near the high-pressure anomaly of the planetary stationary waves where zonal background flow is reduced (Narinesingh et al. 2020). In Winter, although the zonal background flow is strongest out of any season, the stationary wave and transient eddy activity are also strongest. Conversely in summer, the stationary wave and transient eddy activity are weaker than in any other season, and also blocking frequency is the smallest of all seasons, despite weaker zonal flow.

We must keep in mind, however, that the work of Paradise et al. (2019) deals with a highly idealized, 1-dimensional model. Thus, Chapters 2 and 3 will provide insight into the spatial distribution of the blocking climatology, using more realistic general circulation models.

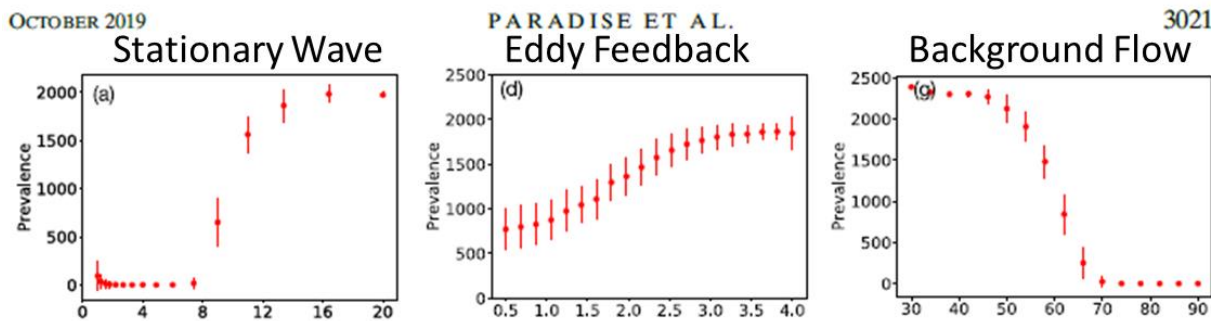


Figure 1.7. Reproduced from Paradise et al. (2019): Using the idealized traffic jam model described in Eq. 1.15, blocked days (prevalence) as a function of (left) stationary wave amplitude, (middle) eddy feedback, and (right) background flow strength.

1.4b Blocking in Comprehensive Models In Current Climates

A precise simulation of the blocking climatology in comprehensive GCM's has yet to be achieved (Davini and D'Andrea 2016, 2020). In the first generation of the Atmospheric Model

Intercomparison Project (AMIP), D'Andrea et al. (1998) found that although the models reproduced the Pacific and Atlantic blocking maxima, there was a general underestimation in blocking frequency and duration. Numerous studies since then have assessed blocking biases in more recent models (Scaife et al. 2010; Barnes et al. 2011; Masato et al. 2013; Anstey et al. 2013; Davini and D'Andrea 2020). All have found biases in model blocking climatologies, albeit with some improvement for more recent generations of Coupled Model Intercomparison Project (CMIP) models (Fig. 1.8; Davini and D'Andrea 2016, 2020).

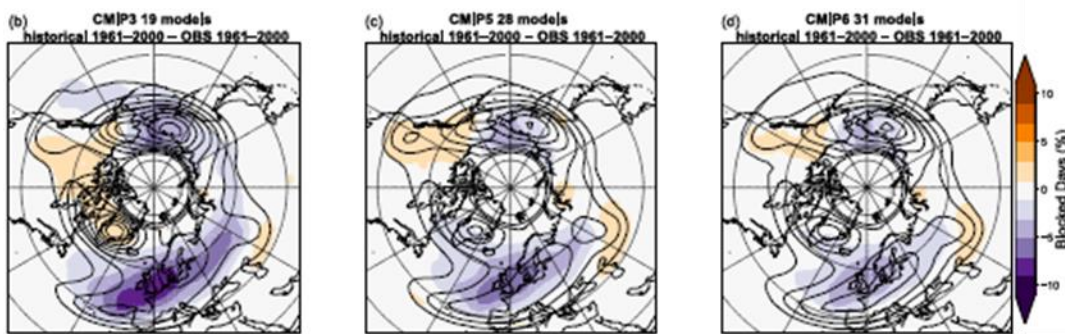


Figure 1.8. Reproduced from Davini and D'Andrea 2020: Biases in the winter blocking climatology (shading) for the multi model mean in (left) CMIP3, (middle) CMIP5, and (right) CMIP6 models.

For the most recent CMIP models (CMIP6), the multi-model mean of blocking in the Northern Hemisphere is underestimated compared to reality (Davini and D'Andrea 2020). These biases have been associated with both mean state biases (Scaife et al. 2010; Davini and D'Andrea 2016; Kleiner et al 2021) and model limitations in resolving sub-grid scale processes (Jung et al. 2012; Anstey et al. 2013; Davini et al. 2017; Jiang et al. 2019; Steinfeld et al. 2020).

Though we have an idea of how mean and transient circulation features are linked to blocking, these relationships are not well understood. For example, where some studies suggest less blocking for poleward shifted jets, others have found more (Yeh 1949; Wang and Kuang 2019).

As such, Chapter 3 of this thesis focuses on general circulation and blocking biases in NOAA Geophysical Fluid Dynamics Laboratory (GFDL) models. There, we examine biases in the stationary wave, upper-level jet, and blocking climatology. Constituencies/inconsistencies between mean-state and blocking biases are discussed.

1.4c Blocking in Future Climates

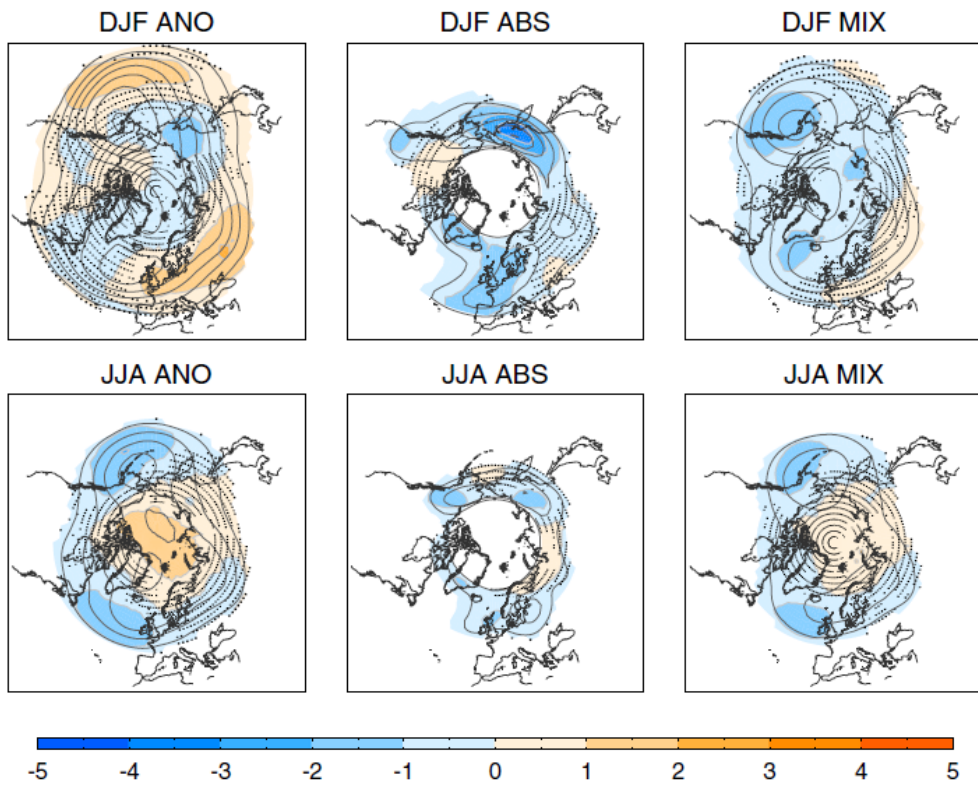


Figure 1.9. Reproduced from Woollings et al. 2018: CMIP5 multi-model mean of changes in the blocking climatology between historical and RCP 8.5 integrations using a geopotential height (left) anomaly, (middle) gradient reversal, and (right) hybrid anomaly and gradient reversal metrics. The top panel are for DJF and the bottom are for JJA.

How will blocking change in future climates? Will the number of events increase or decrease? Will blocks last longer? These are potentially billion-dollar questions when it comes to

the weather hazards blocks can create. To provide more background for Chapter 4, here we briefly review some of the previous work regarding climate projections of blocking.

Using CMIP3 models, Barnes et al. (2011) found a robust decrease in blocking for future warming scenarios across all seasons. This was: (i) accompanied by a strengthening of the midlatitude jets, and, (ii) driven by less events overall rather than a reduction in block duration. Recent studies using CMIP5 and CMIP6 models (Woollings et al 2018; Davini and D’Andrea 2020), however, exhibit more convoluted changes in the blocking climatology for future climates. These results show a regional variation in the frequency of blocking that is also sensitive to which block tracking metric is used for the analysis (Fig. 1.9).

Changes in mean and transient flow features have been associated with changes in blocking (Woollings 2010; De Vries et al. 2013; Dunn-Sigouin and Son 2013; Cheung and Zhou 2015). For example, the downstream shift in winter Euro-Atlantic blocking is consistent with the eastward extension of the jet and storm track, though disentangling cause and effect proves difficult. When interpreting these results, however, one must keep in mind that the models themselves contain errors in the blocking climatology (Fig. 1.8) as well as the general circulation itself (as will be discussed in Chapter 3). Thus, an answer to how blocking may change in the future has yet to be conclusively put forth and likely to evolve as new generations of models are created.

Uncertainty about the future of blocking has profound implications for the future of the hazards that blocking can impose. In Chapter 4, blocking, persistent heat extremes, and the association of the two are investigated in a “business as usual” (Riahi et al. 2011) climate change projection. Changes in the mean and transient circulation as they relate to blocking is also discussed.

1.5 Outline of Thesis and Research

Motivated by the blocking-related questions discussed above, this thesis investigates the climatology and dynamics of atmospheric blocking using a hierarchy of models. The original research herein is separated into three distinct papers corresponding to Chapters 2, 3, and 4, respectively. The research questions for each of these chapters is outlined below. Each chapter contains its own abstract, introduction, motivation, methods, results, and conclusions. Chapter 2 has been published in Weather and Climate Dynamics. Chapter 3 has gone through revisions at Journal of Climate and Chapter 4 will soon be submitted to the Geophysical Research Letters journal of AGU.

1.5a Chapter 2: Atmospheric Blocking in an Aquaplanet and the Impact of Orography

This chapter focuses on winter blocking in an idealized moist GCM. First the idealized model is configured as an aquaplanet to assess if the model accurately captures the dynamical lifecycles of blocking. Then, in separate integrations, orography is introduced into the model to investigate the effects of mountains on the blocking climatology and block duration. The research questions are listed below:

1. Are blocks in an aquaplanet dynamically similar to blocks in orographically forced simulations and reanalysis?
2. What is the impact of orography on the hemispherically-averaged frequency of blocking?
3. How does orography affect the spatial distribution of blocking frequency?
4. Does orography affect the duration of blocking events?

1.5b Chapter 3: Blocking and General Circulation in GFDL

Comprehensive Climate Models

Winter blocking in GFDL models is investigated in this chapter. Here, the models of focus are the atmosphere only model, AM4, and the coupled atmosphere-ocean model, CM4. First, each model's reproduction of the mean circulation is compared against one another and reanalysis. Then the same is done for the blocking climatology and block-centered compositing of geopotential height and transient eddy forcing. Lastly, the consistencies between blocking biases and biases in mean and transient flow features are discussed. The research questions are below:

1. What are the biases in the winter stationary wave and upper-level jet in AM4 and CM4?
How do these general circulation features compare between models?
2. What are the biases in the winter blocking climatology in AM4 and CM4?
3. How do biases in the blocking climatology compare between models and are they consistent with any biases in the general circulation?
4. Do the models accurately capture blocking onset in terms of geopotential height and transient eddy forcing?

1.5c Chapter 4: Connections Between Atmospheric Blocking and Heat

Extremes in Current and Possible Future Climates

Chapter 4 focuses on summer blocking and persistent heat extremes in reanalysis along with historical and warming integrations of GFDL's CM4. First focusing on reanalysis, regional dependence of the co-location of blocking and heat extremes is investigated. Then, heat extremes associated with blocking are compared to those not associated with blocking. CM4's fidelity in reproducing blocking and its association with heat extremes is then assessed. Lastly, the

temperature and duration of heat extremes in a historical integration and climate change projection of CM4 are compared. Research Questions:

1. Across the Northern Hemisphere, what is the regional variation in the co-location of atmospheric blocking and persistent extreme heat events?
2. How does the dynamical and thermal evolution of persistent extreme heat events co-located with blocking differ from those not co-located with blocking?
3. How do blocking, persistent heat extremes, and the association between the two differ in the historical versus climate change integrations of CM4?

Chapter 5 is a conclusion section pertinent to Chapters 2-4; There, a reflection and summary of these chapters are presented along with ideas for future research.

Chapter 6 is its own self-contained component separate from the previous chapters. Chapter 6 focuses on the fields of STEM education and diversity in STEM. Original research regarding outcomes from a COVID-era mentoring program developed for youths from underserved communities is presented. This mentoring program was developed with the National Society of Black Physicists and Harlem Gallery of Science.

Chapter 2

Atmospheric Blocking in an Aquaplanet and the Impact of Orography¹

Veeshan Narinesingh, James F. Booth, Spencer K. Clark, Yi Ming

Abstract

Many fundamental questions remain about the roles and effects of stationary forcing on atmospheric blocking. As such, this work utilizes an idealized moist GCM to investigate atmospheric blocking in terms of dynamics, geographical location, and duration. The model is first configured as an aquaplanet, then orography is added in separate integrations. Block-centered composites of wave activity fluxes and height show that blocks in the aquaplanet undergo a realistic dynamical evolution when compared to reanalysis. Blocks in the aquaplanet are also found to have similar lifecycles to blocks in model integrations with orography. These results affirm the usefulness of both zonally symmetric and asymmetric idealized model configurations for studying blocking. Adding orography to the model leads to an increase in blocking. This mirrors what is observed when comparing the northern (NH) and southern hemispheres (SH) of Earth, where the NH contains more orography, and thus more blocking. As the prescribed mountain height is increased, so does the magnitude and size of climatological stationary waves, resulting in more

¹ Narinesingh, V., J. F. Booth, S. K. Clark, and Y. Ming, 2020: Atmospheric blocking in an aquaplanet and the impact of orography. *Weather and Climate Dynamics*, **1**, 293-311, doi:10.5194/wcd-1-293-2020.

blocking overall. Increases in blocking, however, are not spatially uniform. Orography is found to induce regions of enhanced block frequency just upstream of mountains, near high pressure anomalies in the stationary waves which is poleward of climatological minima in upper-level zonal wind. While block frequency minima and jet maxima occur eastward of the wave trough. This result matches what is observed near the Rocky Mountains. Finally, an analysis of block duration suggests blocks generated near stationary wave maxima last slightly longer than blocks that form far from, or without orography. Overall, the results of this work help to explain some of the observed similarities and differences in blocking between the NH and SH of Earth and emphasizes the importance of general circulation features in setting where blocks most frequently occur.

2.1 Introduction

Atmospheric blocks are quasi-stationary anticyclones that can cause temperature extremes (Sillman et al., 2011; Pfahl and Wernli, 2012), steer hurricanes and extratropical cyclones (Mattingly et al., 2015; Booth et al. 2017, respectively), and induce persistent weather (Cassou et al., 2005; Dole et al., 2011; Brunner et al., 2018). For readers looking for a comprehensive review of blocking, see Woollings et al. 2018. Despite the expensive and sometimes deadly impacts of blocks, many fundamental questions remain regarding their behavior, and models tend to underpredict blocks in terms of their frequency and duration (D'andrea et al., 1998; Matsueda, 2009). As such, this paper utilizes an idealized general circulation model to expand our understanding of blocks, focusing on the representation in models configured with and without mountains.

Some have argued that blocks are consequences of an interaction between eddies and stationary waves induced by orography (Egger, 1978; Charney and Devore, 1979; Tung and

Lindzen, 1979; Luo, 2005). These studies suggest mountains are critical for the overall existence of blocking and setting the location of climatological block frequency maxima. On the other hand, Shutts (1983) used a barotropic model to show that blocking flows do not necessarily need stationary forcing and can arise purely through interactions between transient eddies. Confirming this, Hu et al. (2008), Hassanzadeh et al. (2014), and Nabizadeh et al. (2019) have more recently shown that blocks do indeed occur in idealized models in the absence of zonally asymmetric forcing.

This suggests the extratropical cyclones (i.e., synoptic-scale eddies) that occur upstream of the blocking regions may be key. Colucci (1985) and Pfahl et al. (2015) show that extratropical cyclones can impact blocks downstream of the storm track exit region. In a related theory, blocks are linked to Rossby wave-breaking (Pelly and Hoskins, 2003; Berrisford et al., 2007; Masato et al., 2012), which primarily occurs in regions of weak westerly flow.

Hu. et al. (2008) presents case studies that show blocks in an aquaplanet model behave in a realistic manner. They also find that blocks in their aquaplanet model occur more frequently than what is observed in nature – regardless of hemisphere, which is contradictory to the idea that stationary waves facilitate blocking episodes. The results of Hu et al. (2008) however, are complicated by known discrepancies within the community regarding the identification (e.g., Barnes et al., 2012) and seasonality (Barriopedro et al., 2010) of blocking. In Hu et al. (2008), results from their perpetual equinox aquaplanet are compared to Weidenmann et al. (2002), who use a different block identification algorithm on reanalysis over all seasons. Thus, questions remain regarding the relative frequency of blocks with and without the presence of mountains.

The climatological spatial distribution of blocks is well documented. In the cool months of the Northern Hemisphere (NH), two main regions of blocking occur at the north-eastern edges of

the Atlantic and Pacific Ocean basins (Barriopedro et al., 2006; Croci-Maspoli et al., 2007; Dunn-Sigouin et al., 2013). In the Southern Hemisphere (SH), one main region of blocking exists, located southwest of South America (Renwick, 2005; Parsons et al., 2016; Brunner and Steiner, 2017). Overall, blocking occurs more frequently in the northern hemisphere than the southern. This difference in blocking frequency is assumed to relate to the stronger stationary wave in the NH (Nakamura and Huang, 2018), often attributed to more prominent midlatitude topography and land-sea contrasts, e.g., Held et al. (2002). However, to our knowledge, no study has confirmed this assumption.

Previous work suggests that the spatial distribution of blocking frequency (hereafter, the blocking climatology) is dependent on the behavior of the stationary waves, jet streams, and storm tracks. Nakamura and Huang (2018) for example, propose that blocking is most ubiquitous in regions where the positive anomaly in the stationary wave maximizes, and mean westerly flow is weak. Work by others on the effects of transient eddy forcing on blocks (Shutts, 1983; Nakamura et al., 1997; Takaya and Nakamura, 2001; Wang and Kuang, 2019), shows the importance of the storm tracks. The work presented here aims to better characterize the manner in which the spatial distribution of the stationary waves, jet streams, and storm tracks are linked to the blocking climatology.

This article focuses on 4 main research questions:

1. Are blocks in an aquaplanet dynamically similar to blocks in orographically forced simulations and reanalysis?
2. Does the presence of orography affect the hemispherically-averaged frequency of blocking?
3. How does orography affect the spatial distribution of blocking frequency?

4. Does orography affect the duration of blocking events?

To address question 1, we use compositing analysis to compare the life cycles of blocks for an aquaplanet, reanalysis and a model with orography. For questions 2 and 3, we compare the climatology of blocking, stationary waves, jet streams, and storm tracks for models with different orographic configurations. To answer question 4, we carry out an analysis that examines the sensitivity of block duration to mountains.

2.2 Methods

2.2a Reanalysis Data

Although the focus of this paper is on idealized numerical modelling experiments, we also present results using reanalysis to motivate our work. The reanalysis used is the ECMWF ERA-Interim dataset (Dee et al., 2011). ERA-Interim (ERA-1) has been shown to represent winter midlatitude storms as well as, and in some cases better than, other reanalyses (Hodges et al., 2011). Therefore, it likely does a reasonable job at capturing atmospheric blocking. ERA-Interim is produced using a model with roughly 0.67-degree resolution, but it is available to download at different resolutions. Herein, we used data with a 1.5 x 1.5 degree horizontal resolution. For this analysis we focus only on the cool season from 1979-2017, which is defined as Nov. – Mar., and May – Sept. for the Northern and Southern Hemispheres, respectively. Blocks are most abundant during these months (Tibaldi et al., 1994; Barriopedro et al., 2010).

2.2b Idealized Model Configuration

This work utilizes an idealized moist GCM described by Clark et al. (2018; 2019), which is modified from that introduced by Frierson et. al. (2006; 2007) and later altered by Frierson (2007) and O’Gorman and Schneider (2008). The model is configured to use 30 unevenly spaced

vertical sigma coordinate levels, and T42 spectral resolution, corresponding to 64 latitude by 128 longitude grid points when transformed to a latitude-longitude grid. Earth-like orbital parameters are used to simulate a full seasonal cycle in solar insolation. The model includes full radiative transfer and simplified physics parameterizations of convection (Frierson, 2007), boundary layer turbulence (Troen and Mahrt, 1986), and surface fluxes. There is no treatment of cloud radiative effects or condensed water in the atmosphere.

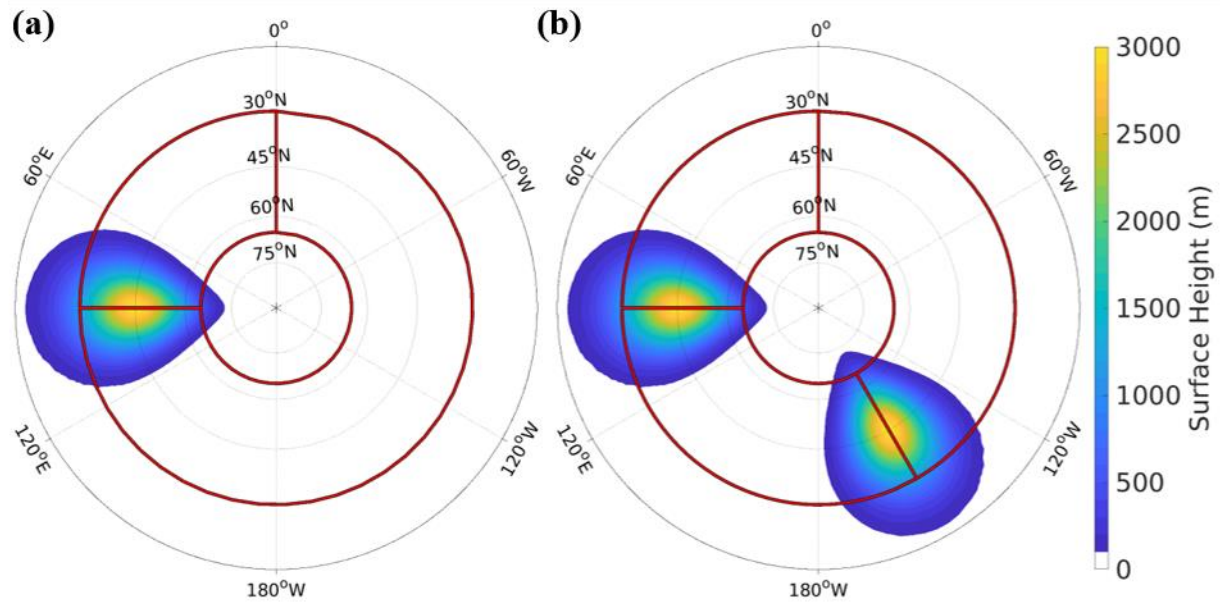


Figure 2.1. Surface height (shading) of the idealized model integrations with (a) a single 3 km high Gaussian mountain centered at 45 N, 90E and (b) two 3 km high Gaussian mountains centered at 45 N, 90E and 45 N, 150 W, respectively. The red outlines indicate the block genesis regions described in Table 2.1.

An aquaplanet configuration is run as the control integration. For the integrations with mountains, configurations of topographical forcing are simulated by modifying the model surface height and using a simplified treatment of land following Geen et al. (2017) and Vallis et al. (2018). Like Cook and Held (1992), and following Lutsko and Held (2016), perturbations to the surface height are introduced in the form of Gaussian mountains centered at 45° N with half-widths of 15

degrees in both the latitude and longitude dimensions. Several configurations are examined in this work:

- a) Aquaplanet: idealized model with no orography
- b) SingleMtn: 4 separate integrations with a single Gaussian mountain centered at 45° N, 90° E of variable peak height (1 km, 2 km, 3 km, 4 km respectively)
- c) TwoMtn: 1 integration with two Asymmetrically placed 3 km high Gaussian mountains centered at 45° N, 90° E and 45° N, 150° W respectively. This placement is to loosely mimic the wide (Pacific) and short (Atlantic) zonal extents of the NH ocean basins.

The 3 km SingleMtn and TwoMtn configurations are shown in Figure 2.1. Ocean grid cells are represented using a slab ocean with a depth of 20 m. For simplicity we prescribe uniformly zero Q-flux, meaning that we assume that in the time mean, the net flux of energy from the ocean to the atmosphere is zero at all surface grid cells. In the configurations with mountains, land grid cells are defined as locations where the height is greater than 1/100th of the maximum surface height (3 km), corresponding to a height threshold of 30 m. As in Geen et al. (2017) and Vallis et al. (2018) land is simulated by reducing the slab ocean depth to 2 m (effectively reducing the heat capacity) and limiting evaporation using a bucket hydrology model. A uniform surface albedo of 0.26 is used to obtain a global annual mean surface temperature resembling that of the Earth. Each configuration is integrated for 40 years, but the first 10 years are discarded as spin-up time. Thus, the results presented here are for years 11-40 of each integration. 6-hourly data sets are used for the analyses in this paper, and the results are presented for Northern Hemisphere cool season, defined as the 5 months centered on the minimum in solar insolation. The model data is interpolated to the 1.5 x 1.5 degree horizontal ERA-Interim resolution prior to any analysis.

2.2c Block Detection and Tracking

Here we use a 500 hPa geopotential height (Z500) hybrid metric that utilizes the Z500 anomaly and meridional gradient. This metric was chosen for its robustness in terms of capturing high amplitude events involving wave-breaking (Dunn-Sigouin et al., 2013), and because it only requires the Z500 field – which simplifies tracking when analyzing large datasets. Barnes et al. (2012) finds that utilizing a Z500 metric produces similar blocking durations and climatologies to both potential vorticity and potential temperature based metrics. Blocks are detected and tracked using the algorithm described by Dunn-Sigouin et. al. (2013), hereinafter as DS13, which is an adaptation of previous methods by Barriopedro et al. (2010) and Sausen et al. (1995). This algorithm searches for large, contiguous regions of persistent, high amplitude, positive anomalies in the Z500 field. Within these regions, Z500 must satisfy a meridional gradient reversal condition. What follows is an overview of the block identification algorithm, but specific details can be found in DS13:

1. Z500 Anomaly Calculation: For each grid-point poleward of 30 N, from the raw Z500 field subtract the running annual mean and mean seasonal cycle as computed in DS13.
2. Normalize each anomaly value by the sin of its latitude divided by sin of 45 degrees, i.e.
$$\frac{\sin(\phi_{ij})}{\sin(45^\circ)}$$
, where ϕ_{ij} is the latitude of an arbitrary grid-point with longitude i and latitude j .
This normalized anomaly will be referred to as $Z500'$.
3. For each month, in a 3-month window centered on a given month, calculate the standard deviation, S , of all $Z500'$ values.
4. Amplitude threshold: Identify contiguous regions of positive $Z500'$, greater or equal to $1.5*S$.
5. Size threshold: Regions must be at least $2.5 \times 10^6 \text{ km}^2$ in area.

6. Gradient Reversal: The meridional gradient of the Z500 field within candidate regions must undergo a reversal in sign as described by DS13.
7. Quasi-stationary condition: For each timestep, regions must have a 50 % area overlap with its previous timestep (modified from DS13's 2 day overlap which was applied to daily mean data)
8. Blocks must meet the above criteria for at least 5 days (e.g. 20 6-hourly timesteps)

In case studies using ERAI and the idealized configurations described here, it was observed that two existing blocks sometimes merged with one another to form a single, larger block. We objectively identified this merging process based on extreme shifts in the location of the block centroid (defined as the gridpoint that is the centroid of the anomalous area associated with the block). If the centroid shifted by more than 1500 km from one 6-hourly snapshot to the next, we labelled the block as a merged event. These merged events represented 23-27 percent of the total initial blocks found in the idealized model integrations. We judge these events to be unique in terms of their relationship between block duration. Furthermore, the merger-blocks create uncertainty in terms of defining a block centre for the sake of our block-centered composite analysis. Therefore, we have excluded the merged events from our block-centered compositing and block duration analyses. The blocking climatological analysis on the other hand, retains all blocks since the primary focus is on the spatial distribution of block frequency, not the individual blocks themselves.

2.2d Analysis Metrics

The metrics used to characterize climatological features and blocking in the idealized model data and reanalysis are outlined below.

2.2d.i Stationary Wave and Eulerian Storm Track

The cool season stationary wave at each point is defined as the anomaly with respect to the zonal mean of the cool season climatology for the 250-hPa geopotential height field: $\overline{Z^*} = \overline{Z} - [\overline{Z}]$, where brackets indicate the zonal mean and overbar indicates the time mean over cool season days for all years. This is computed separately for each gridpoint.

The Eulerian storm track is presented as the standard deviation of a 24-hour difference of the daily mean Z500 field during cool season (Wallace et al., 1988; Guo et al., 2009; Booth et al., 2017). Consider $Z_{500}(t)$ to be the daily mean Z500 value for an arbitrary gridpoint. To obtain the storm track:

1. The 24-hour difference, Z_{500}^τ , at each gridpoint is taken as:

$$Z_{500}^\tau = Z_{500}(t+1) - Z_{500}(t)$$

2. Then, the standard deviation of Z_{500}^τ for all cool season timesteps at each gridpoint is taken to obtain the cool season Eulerian storm track value at that point.

This is computed separately for each gridpoint.

2.2d.ii Blocking and Zonal Wind Climatologies

The spatial distributions of blocking frequency, referred to hereinafter as the blocking climatologies, are calculated by averaging the block identification flag (1 or 0 respectively) per gridpoint over all cool season days. Thus, the blocking climatologies show the percent of cool season timesteps a block (as defined here) is present. This is computed separately at each gridpoint.

The 250 hPa zonal wind climatology, hereinafter referred to as $\overline{U250}$, is presented as the time mean of the 250-hPa zonal wind over the cool season months at each gridpoint.

2.2d.iii Wave Activity Flux Vectors

To better characterize the dynamical evolution of blocks within each model, wave activity flux vectors (hereinafter, \vec{W}) are calculated as described by Takaya and Nakamura (2001), hereinafter TN01. The wave activity flux relates eddy feedback onto the mean state and is essentially the pseudo-momentum associated with Rossby waves. Convergence of \vec{W} is associated with blocking and an overall slowing or reversal of westerly flow. The formulation of \vec{W} in TN01, includes a stationary term that dominates for quasi-stationary, low frequency eddies (i.e. 8- to 30-day timescales), and a non-stationary, group-velocity dependent term that is more relevant for higher frequency eddies. Here we calculate only the stationary, horizontal component of \vec{W} , and focus on contributions solely from the low frequency eddies.

Block centered composites (as described in Sect. 2.5.1. of this paper) are computed using \vec{W} for each block during various stages of the block's lifecycle. The horizontal components of \vec{W} are calculated as in TN01. For this, eddy fields are computed with an 8- to 30-day bandpass filter. This is what is described as low frequency eddies in TN01 and Nakamura et al. (1997). \vec{W} are given by:

$$\vec{W} = \frac{p \cos \phi}{2|\vec{U}|} \begin{pmatrix} U \left(v'^2 - \frac{\Phi'}{f} \frac{\partial v'}{\partial x} \right) + V \left(-u'v' + \frac{\Phi'}{f} \frac{\partial u'}{\partial x} \right) \\ \square \\ U \left(-u'v' + \frac{\Phi'}{f} \frac{\partial v'}{\partial y} \right) + V \left(u'^2 + \frac{\Phi'}{f} \frac{\partial u'}{\partial y} \right) \end{pmatrix}$$

This calculation is performed on variables on the 250-hPa pressure surface. For each point p is the pressure and ϕ is latitude. \vec{U} is the 30-day low-pass filtered horizontal wind vector with zonal and meridional components U and V , respectively. The anomalous zonal wind, meridional wind, and

geopotential are given by u' , v' , and Φ' , respectively. Derivatives are computed using finite-differencing, where zonal derivatives are weighted by latitude. \vec{W} are given in m^2s^{-2} .

2.2e Analysis Methods

2.2e.i Block-centered Compositing

The $Z500'$, \vec{W} , and $\nabla \cdot \vec{W}$ fields are composited around the centroid of each block for the first, strongest, and final days of each block lifecycle. To account for the convergence of meridians, relevant fields are projected onto equal-area grids before compositing. The initial time step of a block is the first timestep that the block satisfies the amplitude, size, and reversal conditions. The strongest time step of a block is defined as the time step with the greatest $Z500'$ (at a single lat/lon location) within a block. The final timestep is the last timestep a block satisfies the amplitude, size, and reversal conditions.

The composites presented in this paper, only include midlatitude-blocks whose centroid are always south of 65° N. This is because we find that the high-latitude blocks exhibit distinct physical behavior. From reanalysis data, high-latitude blocks in the Southern Hemisphere have different dynamical evolution and different impacts on the surrounding flow, as compared to midlatitude blocks (Berrisford et al., 2007). The 65° N cut-off was chosen after estimates showed this to be near the minimum in the meridional potential vorticity gradient, and thus the northern limit of the midlatitude waveguide (e.g. Wirth et al. 2018). Compositing results were robust to changes in cut-off latitude of +/- 7.5° .

2.2e.ii Separating Blocks by Region

To compare the dynamical evolution of blocks originating near the eastern edge of the ocean basins (denoted as “East”, near the windward side of mountains and the high-pressure maxima of stationary waves) against blocks originating elsewhere (denoted as “Other”), blocks

are sorted by their centroid location during their first timestep. These regions are outlined in Table 2.1 and shown in Figure 2.1. The East region spans 30°-65° N for 90 degrees of longitude upstream and inclusive of the mountain center. For the TwoMtn configuration, “East” and “Other” refer to two regions within the zonally larger ocean basin (which we refer to as the “Wide Basin”), whereas blocks originating within the zonally smaller ocean basin are denoted as from the “Short Basin”.

Configuration	Region	Western Edge	Eastern Edge
Single Mountain (SingleMtn)	East	0°	90° E
	Other	90° E	0°
Two Mountains (TwoMtn)	Wide Basin East	0°	90° E
	Wide Basin Other	150° W	0°
	Short Basin	90° E	150° W

Table 2.1. Regions used for subsetting blocks in the compositing and duration analysis. Each region spans 30°- 65° N, for the longitudes listed in the table.

2.2e.iii Block duration probability density distributions

Block duration is defined as the time interval from the initial identification timestep to the end of that block’s existence – based on the block identification algorithm (described in Sect. 2.3). Each block is thus assigned one duration value. The steps taken to obtain block duration probability density distributions are as follows:

1. Sort blocks into subsets by model configuration and/or basin.
2. Allowing replacement, randomly select a set of block durations within a given subset.

The size of the random set is given by the number of blocks in the subset being analyzed.

3. Place the durations yielded by step 2 into n equal sized bins (n=8 for figures in this paper) ranging from the minimum to maximum duration of cool season blocks between all model configurations.
4. Steps 2 and 3 are then repeated m times (m=1000 for figures in this paper) to produce an ensemble of m probability density distributions for each subset.
5. For a given subset, the mean probability density distribution is computed by taking the mean of that subset's distributions. This is then smoothed using a running mean.
6. For a given subset, the standard deviation of probability density distribution is computed by taking the standard deviation of that subset's distributions

The results of this paper are nearly constant with respect to changes in the values of n (+/- 2) and m (+/- 200). For all configurations, distributions and mean values presented for duration exclude any high-latitude blocking (blocks whose centroid are ever poleward of 65° N). 65° N was found to be the most appropriate cut-off in each configuration for the same reasons as described for the aquaplanet compositing.

2.2e.iv Statistical Significance

For a given gridpoint and cool season, a block frequency value is computed by averaging all the block identification flag values (1 or 0) for each timestep of that cool season. This is done at every gridpoint for every cool season to yield a 3D matrix of dimensions latitude by longitude by number of years. For each gridpoint, the distributions of blocking frequency were found to approximately follow Poisson distributions (not shown). Mann-Whitney u-tests are implemented for corresponding gridpoints between a given orographic configuration and a 250-year aquaplanet integration. One strength of the u-test is that it does not rely on parametric fitting to any specific distribution. We therefore find this test to be more appropriate than other tests such as the t-test

which requires fitting to a normal distribution. A 250-year aquaplanet integration is used because the blocking climatology is more zonally symmetric when compared to climatology calculations that use less years. This is done to identify regions of enhanced and suppressed blocking frequency in the topographic integrations.

Significance testing for hemispherically averaged block frequency statistics are done by calculating area averaged blocking frequency for each cool season. For each configuration, this yields a one-dimensional array of values with a length that matches the number of years in the simulation. A 2-sample Welch's t-test is then used to examine significant differences in hemispherically averaged block frequency between idealized model configurations. We find this t-test to be appropriate for this analysis because it accounts for the variances of both samples, and distributions of hemispherically averaged blocking frequency were found to be normally distributed (not shown).

Significance testing for mean block duration also utilizes a u-test to compare differences between the various configurations and regions. A 95% confidence interval is imposed as the significance threshold for all significance testing.

2.3 Results

2.3a Blocking in the Aquaplanet, Dynamical Aspects and Intermodel Comparison

On average, 12.9 blocks per cool season are identified for each hemisphere of the aquaplanet. The presence of blocking in this model configuration is consistent with previous studies that also find blocking in GCM's with zonally symmetric forcing (Hu et al., 2008; Hassanzadeh et al., 2014, Nabizadeh et al., 2019). Figure 2.2 shows a snapshot of the first day of an arbitrary block in the aquaplanet. Upstream and coincident with the block, a Rossby wave

pattern can be observed in both the Z500 and Z500' fields (Fig. 2.2 - the Z500 contours show a wave-like feature, and the Z500' field shows an alternating pattern of low and high anomalies in the zonal direction). The presence of these features during the formation of a block agrees with previous work for both simplified (Berggren et al., 1949; Rex, 1950; Colucci, 1985; Nakamura et al., 1997; Hu et al., 2008), and comprehensive models (TN01; Yamazaki and Itoh, 2013; Nakamura and Huang, 2018; Dong et al., 2019).

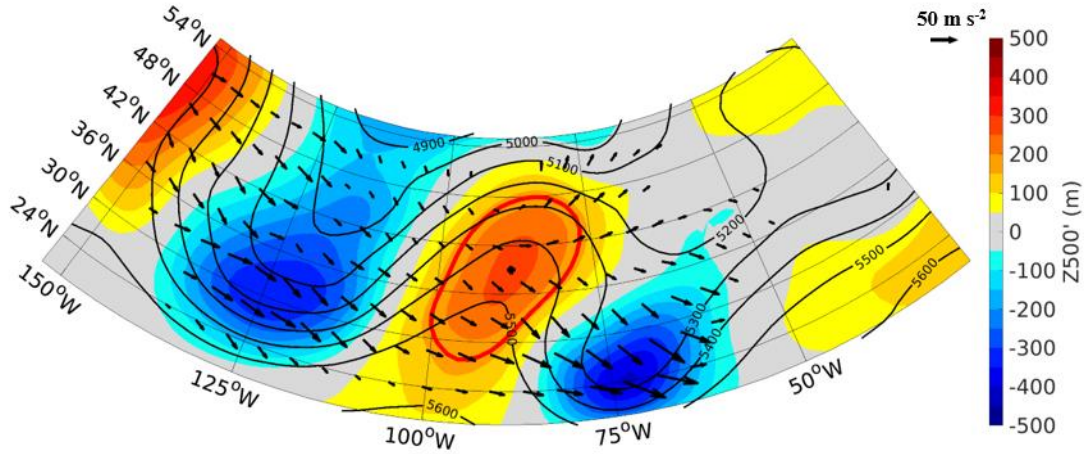


Figure 2.2. 500 hPa geopotential height (black contours), 500 hPa geopotential height anomaly (shading), outline of blocked area (red contour), and wave activity flux vectors \vec{W} (black arrows), for the first day of a blocking episode in the aquaplanet run. The black dot inside the block denotes the block centroid. Geopotential height contours are in 100 m intervals. \vec{W} with magnitudes less than $20 \text{ m}^2 \text{ s}^{-2}$ are removed.

In Figure 2.2 near 75–85° W, a characteristic overturning of the Z500 contours indicative of anticyclonic Rossby wave breaking (Masato et al., 2012; Davini et al., 2012) is also observed. Concentrated, large magnitude \vec{W} are found just upstream of, and propagating into the block, and a relative absence of large magnitude \vec{W} occurs downstream of the block. On the downstream-equatorward flank of the block, converging \vec{W} consistent with a slowing of the zonal mean flow is observed. The behavior of \vec{W} during the genesis of this block case study agrees with Nakamura

et al. (1997) and TN01 and is consistent with Nakamura and Huang's (2018) description of blocking as a traffic jam of wave activity fluxes.

Block-centered compositing analysis is used to confirm that, on average, the blocks identified in the aquaplanet model evolve in a dynamically similar manner to models with zonally asymmetric forcing. Figure 2.3 shows block centered composites of $Z500'$, \vec{W} , and $\nabla \cdot \vec{W}$ for blocks over the NH oceans, and for the SH as well (Fig. 2.3 rows 1 and 2, respectively). In both panels only blocks anchored in the midlatitudes are considered (i.e., occurring between 30° and 65° of latitude). For the sake of comparison with the aquaplanet, blocks over land are excluded. For the idealized model, we show blocks from the aquaplanet (Fig. 2.3, row 3) and the East region (see Table 2.1 and Fig. 2.1) of the 3 km single mountain configuration (3 km SingleMtn East, Fig. 2.3, row 4). The East region of the 3 km SingleMtn was chosen to isolate blocks generated in the model that form near the high-pressure anomaly of stationary waves. However, block-centered composites for all orographic configurations (i.e. 1 km, 2 km, 3 km, and TwoMtn), and each of their respective regions yielded similar results (not shown), with little to no regional variation – this result is discussed again below.

The onset of blocking in the composites (Fig. 2.3, column 1) is qualitatively similar to that found in the case study (Fig. 2.2). The $Z500$ anomalies all show a positive anomaly at the center of the composite and negative anomalies upstream. In the NH, this upstream anomaly has two closed centers (Fig 2.3a), whereas the SH and the idealized configurations each have only one. We have subset the NH observations for the North Atlantic and North Pacific (not shown), and this difference is mainly due to the blocks in the North Atlantic.

The reanalysis and idealized model results all show \vec{W} convergence (i.e., blue shading) on the downstream-equatorward flanks of composite blocks during onset (shading in Fig. 2.3, column

1). The \vec{W} convergence is stronger in the SH and the aquaplanet (Figs. 2.3b and 2.3c) when compared to the NH and the idealized configurations that include orography (Figs. 2.3a and 2.3d).

\vec{W} (vectors in Fig. 2.3) are weaker in the NH at onset (Fig. 2.3a) as compared to the SH and the idealized model. This difference is mainly attributable to the blocks in the North Pacific (not shown) and is likely due to the fact that the \vec{W} shown are for low-frequency eddies only. As discussed in Nakamura et al. (1997), the North Pacific, contributions from low-frequency eddies plays a lesser relative role as compared to the North Atlantic.

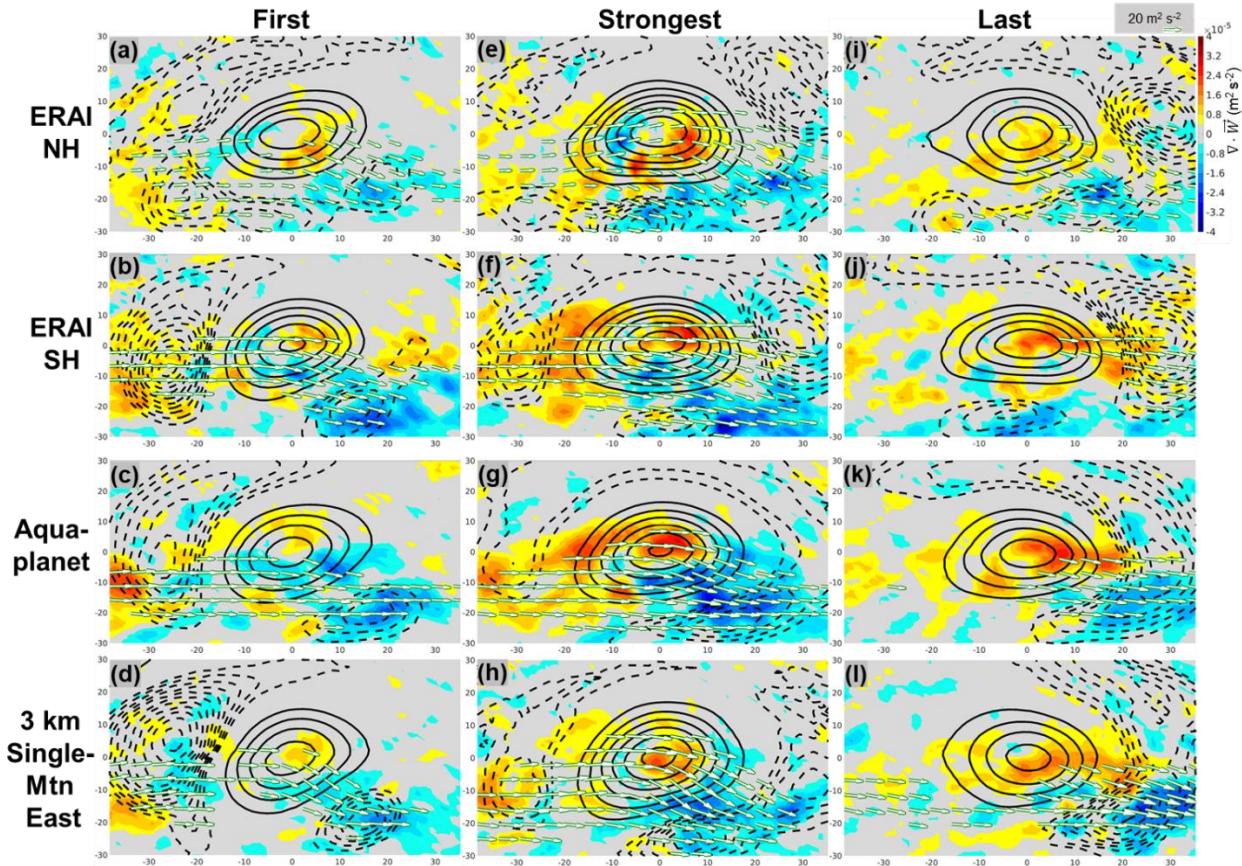


Figure 2.3. For cool season blocking events: Block centered composites of positive 500 hPa geopotential height anomalies (solid contours), negative 500 hPa geopotential height anomalies (dotted contours), \vec{W} (arrows), and $\nabla \cdot \vec{W}$ (shading). (a, e, i): Computed with NH blocks over ocean in ERA-Interim. (b, f, j): Computed with SH blocks in ERA-Interim. (c, g, k): Computed with blocks in the aquaplanet integration. (d, h, l) 4th Row: Computed with blocks in the

3 km single mountain integration. The left, middle, and right columns are composites over the first, strongest, and last timesteps of blocking episodes, respectively. Positive (negative) 500 hPa geopotential height anomaly contours are in 50 m (-10 m) intervals with outer contour 50 m (-30 m). \vec{W} with magnitudes less than $20 \text{ m}^2 \text{ s}^{-2}$ are removed. Latitude and longitude are defined relative to the composite block center.

For composites over blocks at maximum strength (Fig. 2.3 middle column), the positive Z500 anomaly has strengthened, and a similar pattern of $\vec{\nabla} \cdot \vec{W}$ is observed between the reanalysis and the models. Convergence of \vec{W} on the downstream, equatorward flank of the composite blocks are enhanced compared to onset, and the envelope of greatest \vec{W} is now within the high-pressure center. Upstream, downstream, and equatorward low-pressure centers are also evident when the composite blocks are at peak strength, though the pattern is not as clean in idealized model composites (Figs. 2.3g and 2.3h) compared to reanalysis (Figs. 2.3e and 2.3f).

On the final day of the block life cycles (Fig. 2.3., third column), each respective composite block's Z500 anomaly weakens, and low-pressure is concentrated downstream from the block. Weak values of \vec{W} exit the block downstream of the high-pressure maximum during this time (Fig. 2.3c, 2.3f, 2.3i). A net divergence of \vec{W} from the blocked region is indicative of a return to westerly zonal flow as the block dies out. The buildup of \vec{W} upstream and inside the composite block during amplification, and the release of \vec{W} downstream during decay is consistent with downstream development as described in Danielson et al., 2005.

Block-centered composites for the aquaplanet are qualitatively similar to composites for reanalysis, and the similarities are strongest between SH and aquaplanet (Fig. 2.3). This is consistent with the fact that the SH has less orography than the NH. However, we remind the reader that surface forcing in the SH is still asymmetric, as discussed in Berrisford et al. (2007).

Overall, however, the similarities for the model and reanalysis, regardless orography, show the potential utility of an aquaplanet model for understanding the fundamental physics of blocking. Similarities between blocks in the aquaplanet and the orographic configurations show that blocks behave in a similar manner with or without mountains as a source of zonally asymmetric forcing.

On the other hand, the differences between the NH and SH in observations are greater than the differences between the aquaplanet and the blocks in the model configured with mountains (and this result is true even if we use all blocks in the 3km single-mountain model rather than just those near the anticyclonic anomaly of the stationary wave). Thus, the model is missing some details of the internal dynamics of the blocks, as it related to the presence of orography. With this in mind, we now shift our focus to the climatological flow features and blocking climatology.

2.3b Climatological Analysis

The majority of theories on blocking formation and maintenance (summarized in the review by Woollings et al. 2018) imply that stationary waves, storm tracks, and upper-level mean flow all might play important roles setting the spatial distribution of blocking frequency. These quantities are now examined for the aquaplanet, reanalysis, and model integrations with mountains. In our discussion of the climatological features in reanalysis and the SingleMtn configurations, we have chosen the following approach: we first discuss the stationary wave because it is the most fundamental metric that changes when adding mountains; then, we discuss blocking and its relationship to the jet stream. We close the analysis with a discussion of the storm tracks. This choice of the order is motivated by recent theory from Nakamura and Huang (2018) that put greater emphasis on the influence of the jet stream and stationary waves on blocking.

2.3b.i The Aquaplanet

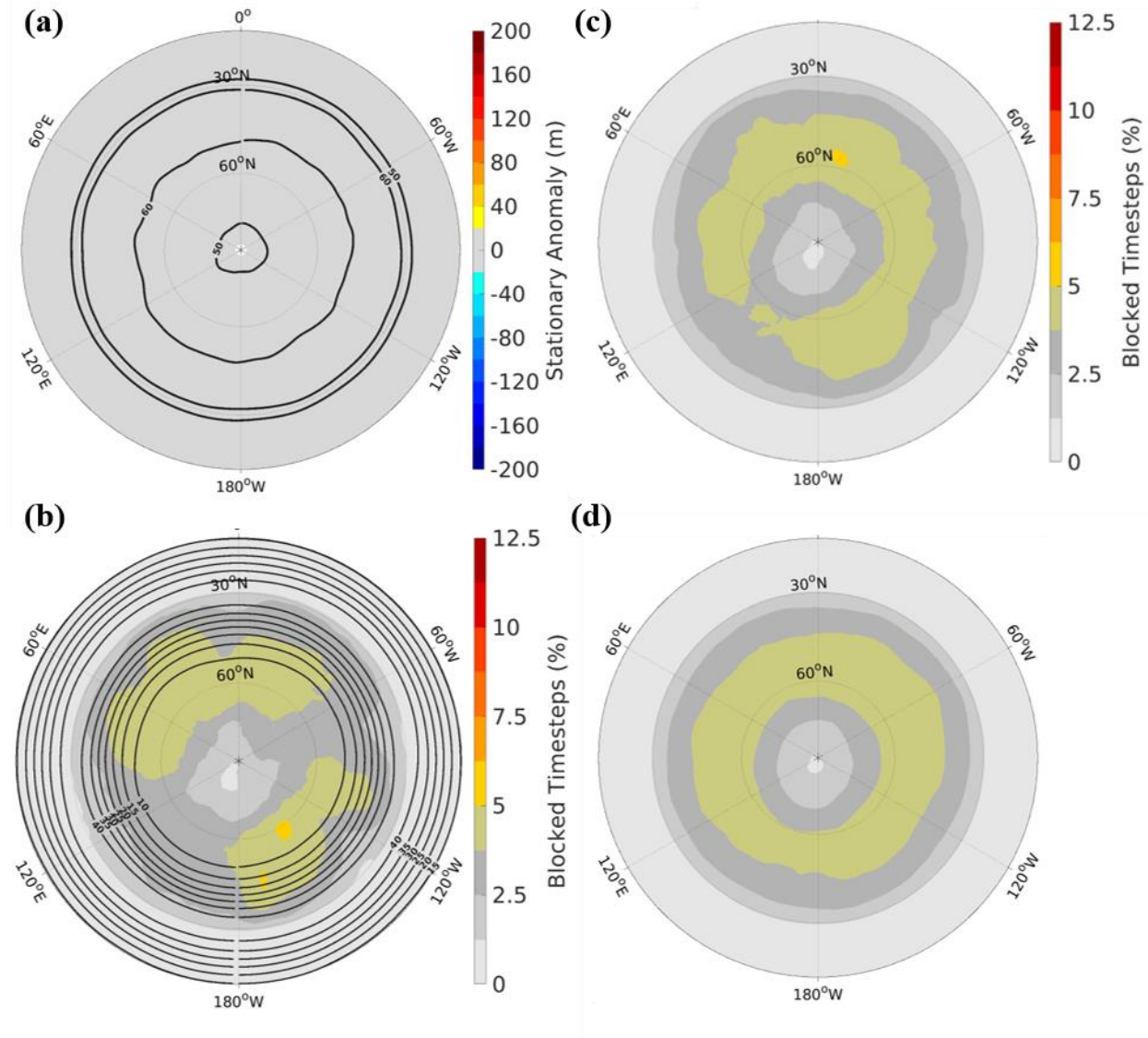


Figure 2.4. (a and b) Left: For 30 cool seasons (Nov.-Mar.) in the aquaplanet, (a) the stationary wave (shading) and storm track (heavy black contours), and (b) the blocking climatology (shading) and $\overline{U250}$ (heavy black contours) for the idealized model aquaplanet integration. (c and d) Right: Blocking climatology (shading) for (c) 100 and (d) 250 cool seasons in the aquaplanet. In (a) storm track contours are in 10 m intervals where the outer contour is 50 m. In (b) $\overline{U250}$ contours are in 5 m/s intervals where the outer contour is 30 m s^{-1} .

For the aquaplanet, the stationary wave, storm track, and $\overline{U250}$ are zonally symmetric (Figs. 2.4a and 2.4b). However, the blocking climatology is not zonally symmetric after 30 years (Fig. 2.4b). We find that it takes 250 years for the aquaplanet blocking climatology to approach zonal symmetry (Figs. 2.4c and 2.4d). However, for the models with orography, the time to reach convergence is likely not as large. We deduced this from the following analysis: we generate 20-year climatologies using randomly sampled years from our 30-year integrations and compare them.

For the configurations with orography, the blocking climatology is spatially consistent, whereas, for the aquaplanet, each climatology has a unique spatial distribution (not shown). Therefore, we believe that 30-years of model runs provides a usable level of convergence of the spatial climatology of blocking in the integrations with mountains.

2.3b.ii Reanalysis

The different orographic configurations of the northern and southern hemispheres produce distinct spatial distributions of general circulation features and atmospheric blocking (Fig. 2.5). Stationary wave patterns can emerge due to land-sea heating contrasts, drag, and flow deflection by topography (e.g. Held et al., 2002). The two strongest regions of anomalous high-pressure in the NH are located on the windward side of the Rocky Mountains, and near the western edge of Europe (Fig. 2.5a). In the SH, the high-pressure maximum is southwest of South America, and a secondary maximum can be found southeast of Australia (Fig. 2.5b). These results are consistent with previous work (Valdes and Hoskins, 1991; Quintanar and Mechoso, 1995; Held et al., 2002; White et al., 2017).

Near the high-pressure stationary wave maxima (Figs. 2.5a-b), regions of suppressed $\overline{U250}$ are apparent (Figs. 2.5c-d). These regions have been shown to be regions of local maxima for Rossby wave breaking (Abatzoglou and Magnusdottir, 2006; Bowley et al. 2018). These regions

are also where blocks are found to occur most often (Figs. 2.5c-d), in agreement with previous work (Wallace et al., 1988; Barriopedro et al., 2006; Dunn-Sigouin, 2013; Brunner and Steiner, 2017). According to Nakamura and Huang (2018), strong positive stationary wave anomalies, and weak mean westerlies are conducive to blocking. These conditions act to slow down the “speed limit” on \overrightarrow{W} , leading to “traffic jams” manifested as blocking episodes. Conversely, regions of strong westerlies, and negative stationary wave anomalies have an opposite effect, hence the suppression of blocking in regions of maximal $\overline{U250}$ (Figs. 2.5c-d) near climatological lows (Figs. 2.5a-b).

Focusing next on storm tracks, we see that the entrance of the storm tracks occurs on the northeast edge of the $\overline{U250}$ maxima (Fig. 2.5a, 2.5c). The details for this relationship are discussed in Chang et al. (2002) and explored in detail for the North Atlantic in Brayshaw et al. (2009). In the SH, there are also two local maxima in the storm tracks, and they occur to the southeast of the respective $\overline{U250}$ maxima. At the storm track exit region, transient eddies play an important role in the onset (Colucci 1985) and maintenance of blocks (Shutts, 1983; Nakamura et al. 1997; Yamazaki and Itoh 2013; Pfahl et al. 2015; Wang and Kuang, 2019). This region is also where the stationary wave and blocking maxima occur (Fig. 2.5). There is one exception in the SH however: the SH storm track exit at the eastern terminus of the Indian Ocean (i.e., 90° E) does not coincide with a maxima in blocking or the stationary wave – but it is a region of locally weak $\overline{U250}$.

For the NH (SH) in this dataset, 485 (336) blocking events are found yielding a hemispherically-averaged blocking frequency of 2.7 % (1.6 %). We find the differences in hemispherically averaged blocking frequency between the hemispheres to be statistically significant. The greater amount of blocking in the NH is typically assumed to be a result of the relative abundance of topographic features. Therefore, we will use configurations of the model to

explore the effects of mountains on the spatial distribution and hemispherically averaged statistics of blocking frequency.

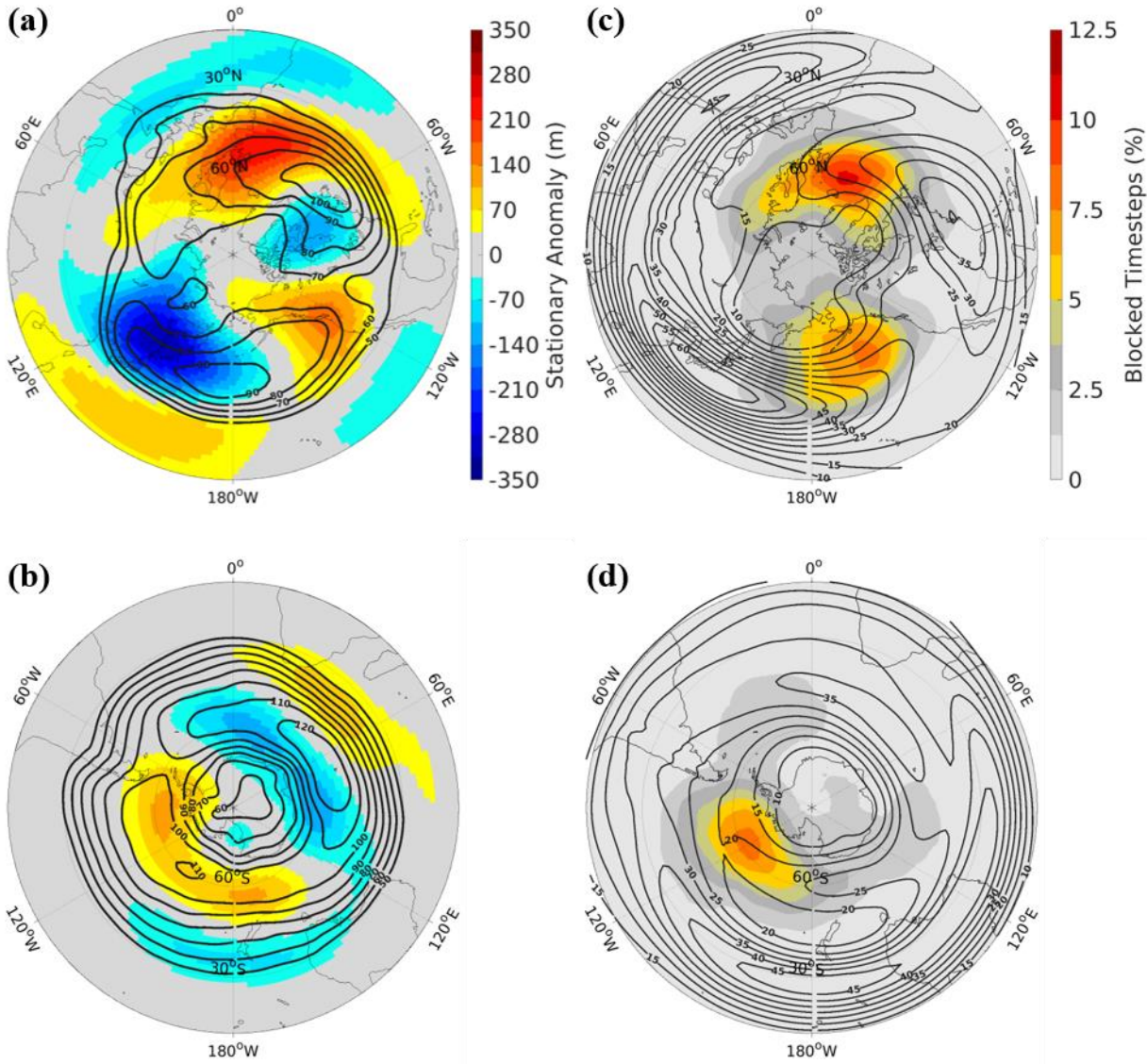


Figure 2.5. (a-b) Left: Cool season stationary wave (shading) and storm track (heavy black contours) for the (a) northern and (b) southern hemispheres in ERA-Interim. Storm track contours are in 10 m intervals where the outer contour is 50 m. (c-d) Right: Cool season blocking climatology (shading) and $\overline{U250}$ (heavy black contours) for the (c) northern and (d) southern hemispheres in ERA-Interim. $\overline{U250}$ contours are in 5 m/s intervals where the outer contour is 10 m s^{-1} .

2.3b.iii Orographic Configurations: Single Mountain of varying height

Here, a single mountain is added to the aquaplanet to study the response of the idealized model blocking climatology to the presence of orography. Figure 2.6 shows the stationary waves, storm tracks, blocking climatologies, and $\overline{U250}$ in the SingleMtn integrations. In each integration, a stationary wave is induced (Figs. 2.6a-6d) with a high-pressure anomaly generated near the coastline on the windward side of the mountain, and a low-pressure anomaly on the leeward side (Fig. 2.6a-d). This results in a meridionally tilted stationary wave pattern that extends into the subtropics leeward of the mountain. This pattern has been explained in previous idealized modeling work (Grose and Hoskins, 1979; Cook and Held, 1992; Lutsko 2016). The intensity and zonal extent of the stationary wave extrema increases with mountain height (Figs. 2.6a-d).

In the SingleMtn integrations, as the height of the mountain is increased, the local maximum in the $\overline{U250}$ increases as well (right column, Fig. 2.6). This relationship between the strength of the local jet maxima and mountain height follows from the thermal wind relationship and the increased temperature gradient in the lower troposphere downstream of the mountain. This mechanism is also apparent in Brayshaw et al. (2009). The stronger temperature gradient is due to enhanced cold advection in the runs with taller mountains. This pattern of the $\overline{U250}$ maximum occurring just downstream of mountains is the same as what occurs for the NH in observations (Fig. 2.5a). Across models, localized strengthening near the maximum $\overline{U250}$ is accompanied by a weakening of $\overline{U250}$ further downstream. In regions poleward of the midlatitude minimum in $\overline{U250}$, blocking is most abundant (Figs. 2.6e-h). This region also coincides with the high-pressure maximum of the stationary wave (Figs. 2.6a-d). The weakened flow and positive stationary wave anomaly here are consistent with a region of lowered \overrightarrow{W} “speed limit” (Nakamura and Huang,

2018), and thus enhanced block frequency. Figures 2.6e-h shows that these regions have significantly more blocking compared to the extended aquaplanet run. On the other side of the mountain, block frequency is significantly suppressed near the low-pressure stationary wave anomaly, poleward of the $\overline{U250}$ maximum.

The presence of mountains also leads to localized storm track maximum in each of the SingleMtn configurations (Figs. 2.6a-d). The storm track maximum straddles the stationary wave minimum immediately downstream of the region where the $\overline{U250}$ maximum occurs (Fig. 2.6e-h).

The storm track exit region in the idealized model does not coincide with the high-pressure stationary anomaly, as it does in the NH of Earth. This allows one to work toward decoupling the response of blocking to each feature. The main blocking maximum occurs near the stationary wave maximum, which is 60° longitude east of the storm track exits. Near the storm track exit region, where the stationary waves are near neutral (i.e. near 90 W), there are suggestions of secondary blocking maxima (Fig. 2.6e-h). This region is perhaps related to the breaking of Rossby waves at the end of the storm track and a local block genesis region associated with strong extratropical cyclones. This would be consistent with theories linking blocking to Rossby wave-breaking (Pelly and Hoskins, 2003; Berrisford et al., 2007; Masato et al. 2012).

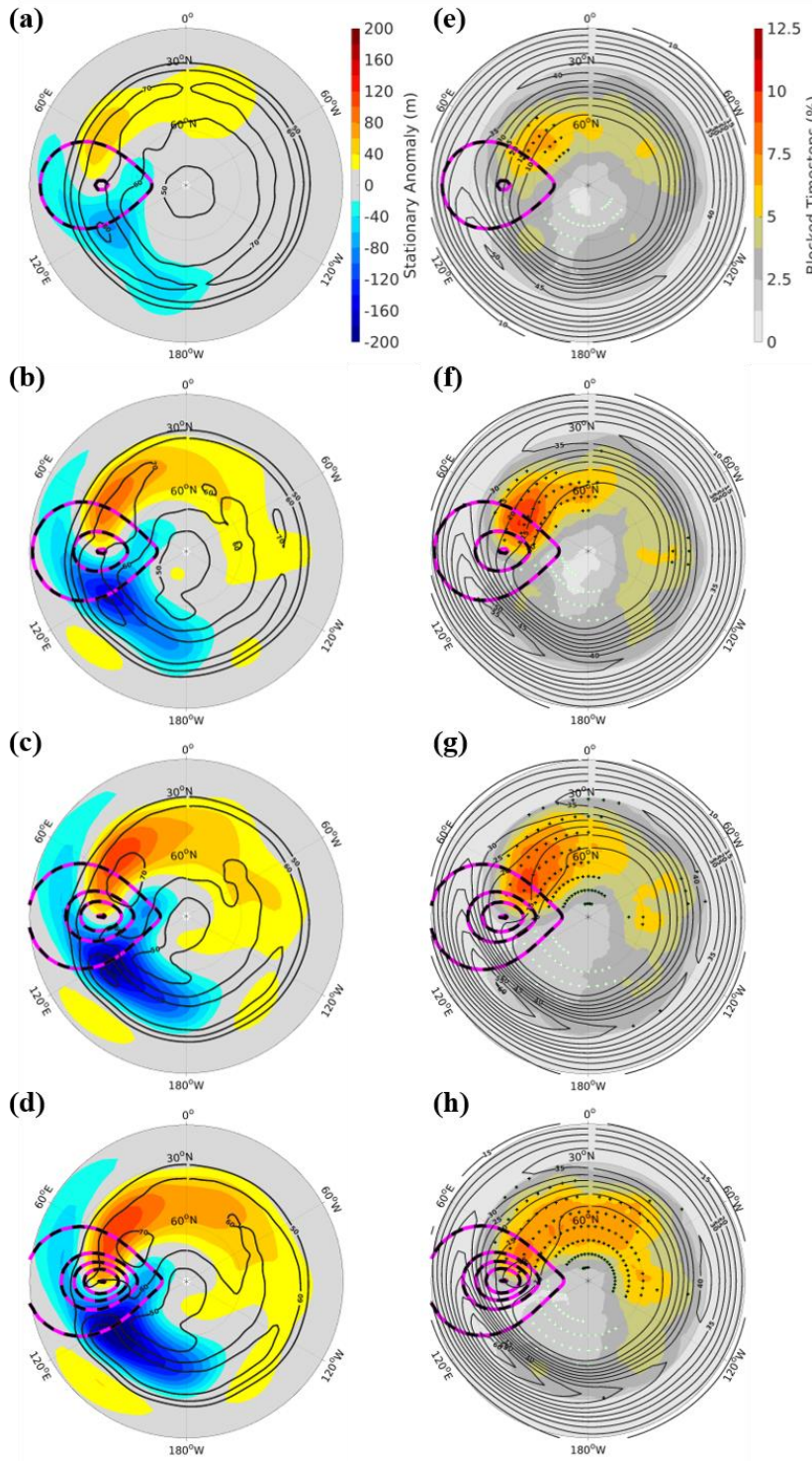


Figure 2.6. (a-d) Left: Cool season stationary wave (shading) and storm track (heavy black contours) for the (a) 1 km, (b) 2 km, (c) 3 km, and (d) 4 km mountain height integrations. Storm track contours are in 10 m intervals where the outer contour is 50 m. (e-h) Right: Cool season blocking climatology (shading) and $\overline{U_{250}}$ (heavy black contours) for the (e) 1 km, (f) 2 km, (g) 3 km, and (h) 4 km mountain height integrations. $\overline{U_{250}}$ contours are in 5 m/s intervals where the outer contour is 10 m s^{-1} . Black (white) stippling in (e-h) indicates significantly greater (less) block frequency at nearby gridpoints when compared to a 250-year aquaplanet integration. Pink and black dotted contours represent surface height, where the outer contour is the edge of the land-mask and the inner contours are in 1 km intervals.

Configuration	Hemispherically averaged Block Frequency (%)	Standard Deviation of Hemispherically Averaged Block Frequency (%)	Number of Events
Aquaplanet	3.24	0.84	387
1 km single mountain	3.17	0.70	365
2 km single mountain	3.67*	1.00	400
3 km single mountain	3.74*	0.90	438
4 km single mountain	3.84*	0.79	433
Two 3 km mountains (TwoMtn)	4.01*	0.99	423

Table 2.2. Cool season area-averaged block frequency and number of events in the idealized model integrations.

Asterisks indicate values that are significantly different from the aquaplanet.

The zonal extent of the blocking climatology maximum increases when mountain height is increased (Figs. 2.6e-h). This agrees with the response of the stationary wave (Figs. 2.6a-d). The overall hemispherically averaged statistics of blocking frequency yields an increase in blocking when mountain height is increased (See Table 2.2). These increases for the 2k-4k configurations are modest however and should be taken with some degree of caution. Still, it is clear that as mountain height increases, there is a greater area of significantly more blocking compared to the aquaplanet (Figs. 2.6e-h). Also worth noting is hemispherically-averaged blocking frequency is significantly greater in the 2k, 3k, and 4k mountain runs when compared with aquaplanet. Next, we investigate the response of adding an additional mountain.

2.3b.iv Orographic Configurations: 2 Mountains

For this analysis, two 3 km-high Gaussian mountains centered at 45° N with 120° of longitude between them are added to the aquaplanet. The placement of the mountains is meant to create a wide and short ocean basin, as observed in the NH of earth. 3 km height is meant to be semi-realistic; the values are lower than the maxima for the Rockies and the Tibetan Plateau (~4400 m and ~8800 m, respectively) – however, the mountains are substantial enough to generate obvious changes in the circulation (as evidenced in the Single Mountain experiments).

The addition of a second mountain induces a second trough and ridge in the stationary wave, and a second maxima for the blocking climatology, storm track, and $\overline{U250}$ (Fig. 2.7). The intensity and zonal extent of these features, however, varies with respect to each mountain and is a result of interference between the forcing (Manabe and Terpstra, 1974; Held et al., 2002; White et al., 2017).

The TwoMtn configuration has a greater hemispherically-averaged blocking frequency than the other configurations (Table 2.2) and is also significantly greater than the aquaplanet. This is despite the TwoMtn configuration having a lower total number of blocks than the 3 and 4 km SingleMtn configurations, respectively – meaning the blocks have a longer average duration in the 2-mountain configuration (Table 2.3). Each mountain also creates regions of enhanced and suppressed blocking frequency (Fig. 2.7b). However, just like the general circulation features, there are differences in the blocking climatology for the two ocean basins.

Next, we examine the blocking climatology within each of the two ocean basins in the TwoMtn simulation (Wide Basin and Short Basin, respectively, see Fig. 2.1 and Table 2.1). In the Wide Basin, there is close to a basinwide enhancement of blocking frequency when compared to the single mountain cases (Figs. 2.6e-h, and 2.7b). Consistent with this enhancement, the overall

midlatitude $\overline{U250}$ climatology is much weaker in the wide basin compared to the other ocean basin and SingleMtn integrations. In the Short Basin, a separate blocking maximum exists near the high-pressure stationary wave anomaly. This maximum, albeit much weaker than its wide basin counterpart, is still significantly more than what occurs in the same region for the aquaplanet.

The proximity of the storm track maximum in the short basin makes there more likely to be times in which storm development occurs just upstream of the mountain; this coupled with a strong background westerly flow would inhibit blocking and perhaps explains the discrepancies between the wide basin and short basin maxima. The shorter ocean basin containing much less blocking is not consistent with what is observed in the NH of Earth, where the Atlantic has a slightly stronger blocking maximum. It seems more elaborate landmasses than this simplified case is needed to better simulate what is observed between the Atlantic and Pacific blocking climatologies in the NH.

2.3c Block Duration Statistics

One of the characteristics that allows blocks to influence midlatitude weather is their persistence. As such, we examine the influence of mountains on block persistence using our duration metric. First, we find that adding mountains leads to at least a modest increase in the average midlatitude block duration (Table 2.3). All topographic configurations aside from 1 km SingleMtn, also have 7-39 more blocks than the aquaplanet (Table 2.3). This helps to explain some of the climatological differences in block frequency between the idealized model configurations (Table 2.2), particularly for the 1 km SingleMtn case. Despite a 0.25-day greater mean block duration (Table 2.3), 1 km was found to have less hemispherically averaged blocking than the aquaplanet (Table 2.2) due to 21 less events. The blocks in the topographic integrations were then

put into subsets based off those originating near the high-pressure stationary wave anomaly and those that were not.

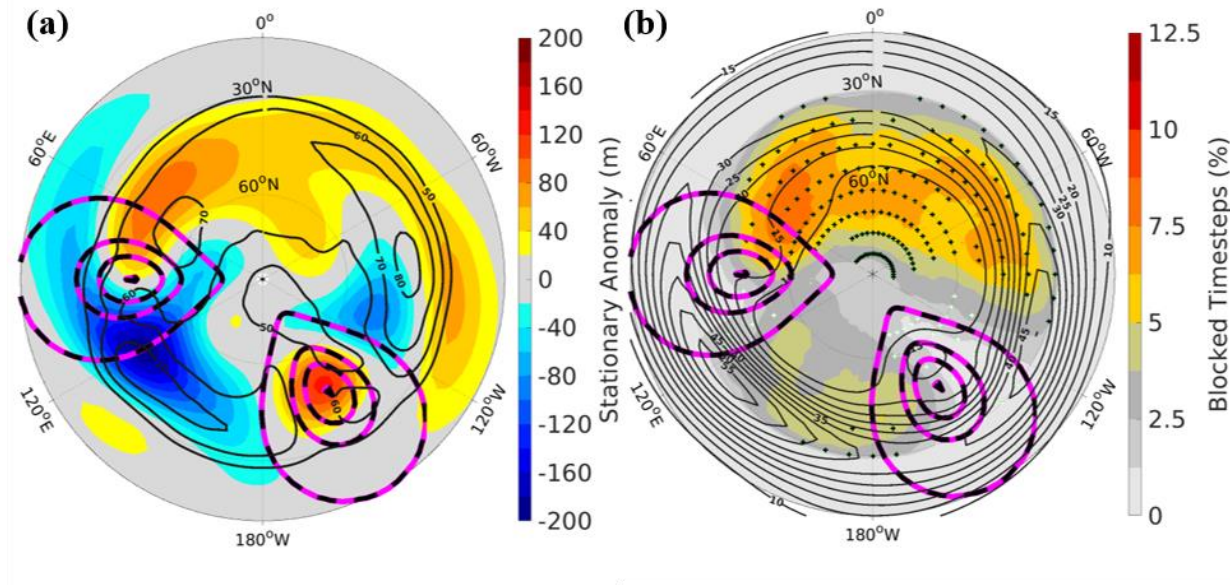


Figure 2.7. For the 2-mountain idealized model integration, (a) the cool season stationary wave (shading) and storm track (heavy black contours), and (b) the cool season blocking climatology (shading) and $\overline{U250}$ (heavy black contours). In (a) storm track contours are in 10 m intervals where the outer contour is 50 m. In (b) $\overline{U250}$ contours are in 5 m/s intervals where the outer contour is 10 m s^{-1} . Black (white) stippling in b indicates significantly greater (less) block frequency at nearby gridpoints when compared to a 250-year aquaplanet integration. Pink and black dotted contours represent surface height, where the outer contour is the edge of the land-mask and the inner contours are in 1 km intervals.

Regions used to subset blocks are denoted as “East”, those originating at the eastern end of the ocean basin near the high-pressure stationary anomaly, and “Other”, those originating elsewhere in the midlatitudes (Fig. 2.1a and Table 2.1). Figure 2.8 shows the probability density distributions for the aquaplanet and East blocks from each configuration. With the exception of the 4 km run, the “East” regions of the single mountain integrations have relatively less shorter duration blocks (i.e. 5-11 days), and relatively more longer duration blocks (11 days or more)

compared to the aquaplanet (Fig. 2.8). Blocks from the “East” regions last longer on average than aquaplanet blocks (Table 2.3), but the 3 km and 4 km enhancement of block duration are not significant to the 95th percentile. Mean block duration is greater for the “East” region compared to the “Other” in the single mountain configurations (Table 2.3), with significant differences found in the 1 km and 2 km integrations. This leads to a cautious suggestion that blocks that originate near mountains last longer on average than those that do not. However, the modest differences found in the 3 km and 4 km integrations must be considered, and the nonlinear response of block duration to linear changes in topography attests the systems own internal variability.

	Mean block duration (days) and number of events		
	All Midlatitude Blocks	East blocks	Other blocks
Aquaplanet	7.53 (227)	-	-
1 km mountain	7.78 (206)	8.65 (58)	7.44 (148)
2 km mountain	7.93 (234)	8.54 (75)	7.64 (159)
3 km mountain	7.55 (266)	7.91 (103)	7.31 (163)
4 km mountain	7.78 (244)	7.99 (81)	7.68 (163)
Two 3 km mountains (TwoMtn)	8.17 (238)	Wide Basin	8.35 (81)
		Short Basin	7.65 (68)

Table 2.3. Mean block duration and number of events in parentheses for midlatitude, cool season blocks in each idealized model configuration.

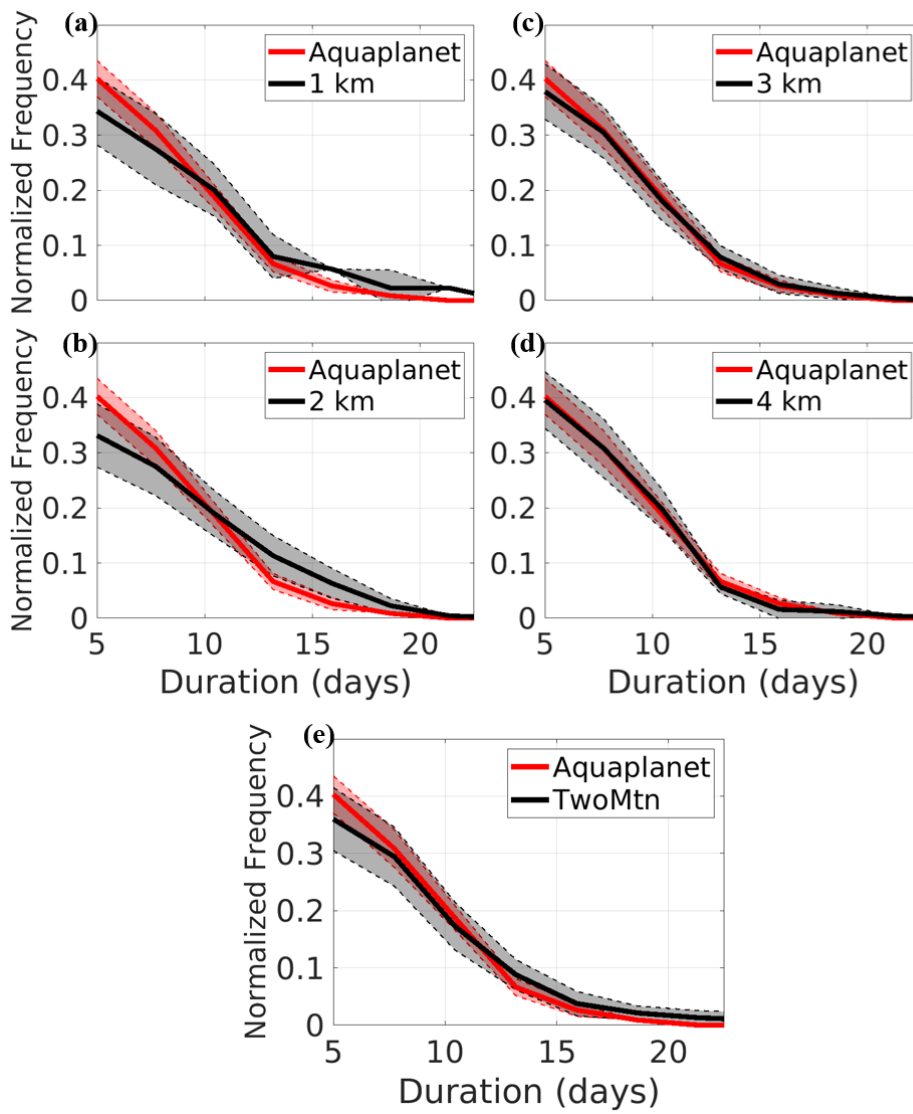


Figure 2.8. Block duration probability density distributions for the aquaplanet and “East” blocks (defined in table 2.1) in (a) SingleMtn 1 km, (b) SingleMtn 2 km, (c) SingleMtn 3 km, (d) SingleMtn 4 km, and (e) TwoMtn configurations. Thick lines denote the mean probability density distribution for each configuration. Shaded regions bordered by dotted lines outline +/- 1 full standard deviation from the mean.

The response of the TwoMtn configuration is much less straightforward. This integration is divided into 3 regions, Wide Basin East, Wide Basin Other, and Short Basin (Fig. 2.1b and Table 2.1); Note the Short Basin does not have distinct “East” and “Other” regions because of its shortened zonal extent. Average block duration in the “Other” region in the Wide Basin is slightly longer than the “East”, but both regions are significantly greater than the Short Basin. This coupled with more Wide Basin East events (Table 2.3) is consistent with the weaker maximum in the

blocking climatology for the Short Basin (Fig. 2.7b). Perhaps this is related to the inhibition of blocking by the nearby storm track and $\overline{U250}$ maximum in the Short Basin, but we do not seek to attribute a causal relationship here.

Our results suggest that blocks starting near mountains last longer on average than those that do not (Table 2.3). In reality we see a similar situation where the NH has more orographic forcing compared to the SH, and also a longer average block duration (8.0 days for the NH and 6.9 days for the SH). In the idealized model, the compositing analysis for the aquaplanet shows similar forcing patterns by low frequency eddies ($\nabla \cdot \vec{W}$) when compared to the SingleMtn East blocks (Figs. 2.3d-i), despite having a shorter average block duration. Perhaps these duration differences can be accounted for by considering block maintenance by high frequency transients (Shutts, 1983; Nakamura et al., 1997; TN01; Yamazaki and Itoh, 2013; Wang and Kuang, 2019). High frequency eddy forcing has yet to be investigated in these experiments, but this will be a topic of future work.

2.4 Discussion

To add some perspective on the role of mountains as compared to land masses with no orographic features, we analyze the response of an idealized model configuration with a single flat land mass, herein referred to as 0 km (Fig. 2.9). The results of 0 km are briefly mentioned here to primarily serve as a benchmark for this setup. This configuration is like the others that include mountains in that it imposes zonally asymmetric forcing in land-sea contrast; The difference, however, is that that the flat land does not act a direct barrier that deflects the flow as the mountains do, generating a unique stationary wave response (e.g. Held et al. 2002) (Figs 2.6a-d, 2.7a, and 2.9).

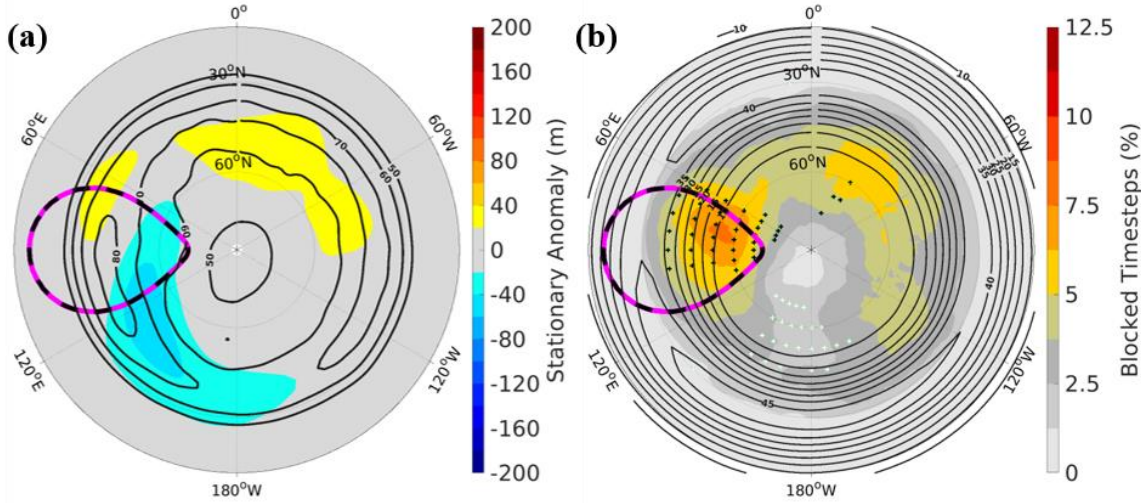


Figure 2.9. For an integration with 1 flat landmass, (a) the cool season stationary wave (shading) and storm track (heavy black contours), and (b) the cool season blocking climatology (shading) and $\overline{U250}$ (heavy black contours). In (a) storm track contours are in 10 m intervals where the outer contour is 50 m. In (b) $\overline{U250}$ contours are in 5 m/s intervals where the outer contour is 10 m s^{-1} . Black (white) stippling in b indicates significantly greater (less) block frequency at nearby gridpoints when compared to a 250-year aquaplanet integration. The pink and black dotted contours represent the outer edge of the land-mask.

The response of $\overline{U250}$ and the storm track (Fig. 2.9) in 0 km agree with results by Brayshaw et al. (2009). Compared to the single mountain runs, the stationary wave pattern is shifted upstream in 0 km (Figs. 2.6 and 2.9). The blocking climatology maximizes (minimizes) poleward of regions where the midlatitude $\overline{U250}$ minimizes (maximizes) (Fig. 2.9b). In the single mountain integrations, the maximum in the blocking climatology is nearly co-located with the maximum in the stationary wave; For the 0 km integration, it is not. The high-pressure stationary anomaly seemingly plays less of a role in the flat case. The 0 km integration has a 3.42 % hemispherically averaged block frequency, which is greater than the aquaplanet and 1 km configurations but less than the others with taller mountains (Table 2.2).

2.5 Summary and Conclusions

This work utilizes an idealized moist GCM to better understand atmospheric blocking. We start with an analysis of blocking in an aquaplanet, then systematically add mountains to investigate the influence of orography on blocking frequency and duration. Below, we recap the answers to the research questions posed in the introduction, followed by concluding remarks.

With regards to question 1, using the aquaplanet we confirm that blocks can be generated without any zonally asymmetric forcing from the surface, consistent with onset governed by eddy-eddy interactions. This result substantiates the results of Hu et al. (2008), Hassanzadeh et al. (2014), and Nabizadeh et al. (2019). To expand on the results of those previous studies, we examined the dynamical life cycle of the blocks in the aquaplanet. Block centered composites of $Z500'$ and \vec{W} show that block lifecycles in the aquaplanet include:

- (1) Large-scale Rossby wave features with \vec{W} entering the block and converging on the downstream-equatorward flank during onset
- (2) Stronger \vec{W} convergence and greater concentrations of \vec{W} inside the block during peak strength
- (3) A net divergence of \vec{W} emitted downstream of the block into low-pressure regions during decay

Similar behavior is shown for reanalysis and the idealized model configurations that include orography, affirming the usefulness of a simple idealized aquaplanet model in better understanding blocks observed in reality.

With regards to questions 2, 3, and 4, in experiments with orographic forcing we modified the aquaplanet model in the following ways: (1) adding a single mountain of different heights in

separate integrations; and (2) in another integration, adding two 3-km high mountains placed in a manner that creates one wide and one short ocean basin. The addition of mountains to the idealized model led to several changes in blocking when compared to the aquaplanet integration:

- There is a significant increase in hemispherically averaged blocking frequency in integrations with mountains of height 2 km and greater (Question 2).
- There are localized maxima in blocking, upstream of mountains; near the high-pressure maximum of the stationary waves; poleward and near climatological minima in $\overline{U250}$ (Question 3).
- There are localized minima in blocking, downstream of mountains; near the low-pressure anomaly of the stationary wave; poleward and near climatological maxima in $\overline{U250}$ (Question 3).
- There is an increase in block duration for blocks originating near mountains, though the statistics are not robust (Question 4).

Based on ERA-Interim reanalysis, these results mirror what is observed for the NH and SH, where the NH contains more topography and blocking. In the idealized model, the enhancement of block frequency near the stationary wave maximum and $\overline{U250}$ minimum is consistent with these regions being conducive to the convergence (or “traffic jamming”) of wave activity fluxes. These regions are found to be far from the storm track exit however, which is dissimilar to the NH in reanalysis. At the storm track exit region, previous work has shown that extratropical cyclones can seed blocks (Colucci 1985) or maintain them, Pfahl et al. (2015). However, in those studies the storm track exit coincides, or sits spatially close to the stationary wave maxima. In our single mountain experiments, the storm track exit is far from the stationary wave maxima, and the result is that the blocks preferentially occur at the stationary wave maxima region. This suggests that the role of the

cyclones in nature may be secondary to the role of the large-scale flow. That being said, secondary blocking maxima are found near the storm track exit in the idealized model, suggesting that this location also plays a key role in anchoring where blocks most frequently occur.

We note that the differences in blocking for model configurations with and without mountains is not identical to the differences between the NH and SH in observations. First, from the block-centered composites (Fig. 2.3), it is clear that the NH versus SH differences in observations for Z500 anomalies and wave activity flux are larger than those found for the aquaplanet as compared to the idealized configurations with orography. This is true for the case shown in Fig. 2.3 (3 km single mountain) and all other model configurations with orography. Additionally, as compared to the aquaplanet versus idealized model configurations with orography (Figs. 2.4, 2.6), the hemispherically-averaged blocking frequency in the NH is much larger than the SH in observations (Fig. 2.5). That being said, there are important aspects of the climatological blocking frequency in observations that are captured well by the model: there is a minimum at the storm track entrance and maximum near the anticyclonic peak of the stationary wave. For the NH, this behavior is clear in the ocean basins. For the SH, the storm track entrance is difficult to pinpoint, but the blocking minima (Fig. 2.5d) corresponds with a local-maxima in near-surface baroclinicity (Nakamura and Shimpo 2004).

Differences in blocking between the different idealized model configurations accentuate the primary role of the stationary wave in determining the preferred location of blocking. Furthermore, the fact that the compositing did not show the same differences for aquaplanet versus mountains cases as SH versus NH implies that the subtleties of the block-centered compositing dynamics do not determine the spatial distribution of the blocks. At the same time, secondary blocking maxima at the storm track exits in the single mountain integrations suggest that synoptic

forcing indeed plays an important role in blocking, consistent with the findings of previous work (Colucci 1985, Nakamura et al. 1997, Yamazaki and Itoh 2013, Pfahl et al. 2015).

One important caveat to these experiments is that land does not include orographic drag. Pithan et al. 2016 showed that orographic drag plays a key role in the tilting of the North Atlantic storm track and the frequency of European blocking episodes. The absence of drag in these experiments could be a reason for the relatively modest changes in hemispherically averaged blocking statistics, as well as the lack of regional variation in blocking within the idealized model. Furthermore, especially for the TwoMtn experiment, one must keep in mind the highly idealized nature of the orography, which does not contain Greenland nor elongated Eurasian and North American continents. Other differences (i.e. treatment of ocean, etc.) could also play a role in discrepancies in blocking between the idealized and reanalysis models, and more systematic investigation is needed.

Overall, this work elucidates fundamental information on the formation, dynamical evolution, spatial distribution, and duration of atmospheric blocking – both in an aquaplanet and configurations with zonally asymmetric forcing. One limitation in the two-mountain experiment, is that each mountain simultaneously affects the stationary wave, jet, and storm track, making it difficult to tell the order of influence each has on the blocking climatology. Understanding the interplay and individual effects of these flow features is key to predicting the behavior of blocks in future climates, which is a topic of future work.

Acknowledgements

This study is supported and monitored by The National Oceanic and Atmospheric Administration – Cooperative Science Center for Earth System Sciences and Remote Sensing Technologies under

the Cooperative Agreement Grant #: NA16SEC4810008. The authors would like to thank The City College of New York, NOAA Center for Earth System Sciences and Remote Sensing Technologies, and NOAA Office of Education, Educational Partnership Program for fellowship support for Veeshan Narinesingh, and the American Society for Engineering Education for their support of Spencer K. Clark through a National Defense Science and Engineering Graduate Fellowship. The statements contained within the manuscript are not the opinions of the funding agency or the U.S. government but reflect the authors 'opinions.

Chapter 3

Blocking and General Circulation in GFDL Comprehensive Climate Models

Veeshan Narinesingh, James F. Booth, Yi Ming

Abstract

This study examines the climatology and dynamics of atmospheric blocking, and the general circulation features that influence blocks in GFDL's atmosphere-only (AM4) and coupled atmosphere-ocean (CM4) comprehensive models. We compare AM4 and CM4 with reanalysis, focusing on winter in the Northern Hemisphere. Both models generate the correct blocking climatology and planetary-scale signatures of the stationary wave. However, at regional scales some biases exist. In the eastern Pacific and over western North America, both models generate excessive blocking frequency and too strong of a stationary wave. In the Atlantic, the models generate too little blocking and a weakened stationary wave. A block-centered compositing analysis of block-onset dynamics reveals that the models: (i) produce realistic patterns of high-frequency (1-6 day) eddy forcing; and (ii) capture the notable differences in the 500-hPa geopotential height field between Pacific and Atlantic blocking. However, the models fail to reproduce stronger wave activity flux convergence in the Atlantic compared to the Pacific. Overall, biases in the blocking climatology, in terms of location and frequency, are quite similar between AM4 and CM4 despite the models having large differences in sea surface temperatures and climatological zonal circulation. This could suggest that other factors could be more dominant in generating blocking biases for these GCMs.

3.1 Introduction

Atmospheric blocks are persistent, quasi-stationary anticyclones (Rex 1950) that can impact midlatitude weather hazards (Sillman 2011; Pfahl and Wernli 2012; Booth et al 2021), cyclonic weather systems (Mattingly et al. 2015; Yamazaki et al. 2015; Booth et al. 2017), and climate (reviewed in Lupo 2020). As such, it is important to understand how blocking will respond to anthropogenic climate change (e.g., Woollings et al. 2018b). However, we first need to understand and quantify the skill of the most recent generation of general circulation models (GCMs) in capturing blocking in current climates and determine how the representation of blocking depends on model general circulation features. Therefore, the work herein analyzes the climatological and dynamical features of blocking in integrations of GFDL's atmosphere-only and coupled atmosphere-ocean comprehensive models for the recent past, i.e., historical integrations from the model intercomparison projects.

Past assessments of GCMs show that the models have issues in capturing blocking. For instance, D'Andrea et al. (1998) analyzed how well the climatological features of blocking were captured in the first Atmospheric Model Intercomparison Project (AMIP). They found that all 15 models underestimated blocking in both the Pacific and Atlantic regions. Since then, various studies have assessed the climatology of blocking across different generations of coupled models that participated in Coupled Model Intercomparison Project (CMIP) experiments (Scaife et al. 2010; Barnes et al. 2012; Masato et al. 2013; Anstey et al. 2013; Davini and D'Andrea 2020). In all cases modeled blocking climatology did not quantitatively match reanalysis. Furthermore, biases in blocking have been found to vary greatly across models, with the Pacific and Atlantic sometimes showing opposite signs in biases (Matsueda et al. 2009; Masato et al. 2013; Jiang et al. 2019).

In the multi-model mean of the CMIP6 models, blocking across the Northern Hemisphere is biased low in terms of blocking frequency (Davini and D’Andrea 2020; Schiemann et al. 2020). These biases have been attributed to mean-state biases (Scaife et al. 2010; Davini and D’Andrea 2016; Kleiner et al 2021). Other more targeted studies, however, suggest that sub-grid scale processes that would likely be more accurately represented by increasing horizontal resolution could be causing biases in a model’s representation of blocking (Jung et al. 2012; Anstey et al. 2013; Davini et al. 2017; Jiang et al. 2019; Steinfeld et al. 2020). Thus, the current state of the literature suggests that both the large-scale and small-scale dynamical features of GCMs might explain model blocking biases.

Theoretical work on blocking offers additional motivation as one considers potential mechanisms for model biases. The recent idealized modeling work of Paradise et al. (2019) suggests that the dynamical details of the models could have important impacts on the blocking climatology. The authors systematically analyze the stationary wave, jet, and high frequency eddy feedback using the “traffic jam” theory introduced by Nakamura and Huang (2018). Paradise et al. (2019) found that the stationary wave and high frequency eddy forcing exhibited a direct relationship with blocking, whereas stronger jets led to less blocking.

Other authors have found the position of the jet, and thus waveguide, to be key to blocking. In work with early models and observations, Yeh (1949) found blocking to be more persistent for higher jet latitudes. Recently, Wang and Kuang (2019) expanded upon the idealized modeling work of Shutts (1983) to show that the orientation of high frequency eddies, not their presence alone, plays a pivotal role in maintaining blocks; yielding results in agreement with Yeh in terms jet latitude, eddy orientation, and blocking (1949). Using comprehensive models, however, Barnes and Hartmann (2010) found a decrease in blocking for higher jet latitudes. Clearly, a full theory of

blocking frequency and its relationship to the mean state is not yet settled. These studies provide context and motivation for more detailed analysis of the links between large-scale features of GCM atmospheric dynamics and modeled blocking.

With this in mind, the study herein investigates the climatology and dynamics of blocking in GFDL's Atmosphere-only Model Version 4 (AM4) and Coupled-ocean Model Version 4 (CM4). The remainder of the paper is organized as follows: Section 2 covers the Data and Methods. In Section 3.a, we analyze model simulation of the stationary wave and upper-level jet. In Section 3.b, we evaluate the blocking climatology. In Section 3.c, block area and duration in the GFDL models is compared to reanalysis. The background flow and transient eddy forcing during block onset is investigated in Sections 3.d and 3.e, respectively; For this, block-centered compositing analyses of geopotential height, low-frequency zonal wind, and high-frequency eddy forcing is separately carried out for Pacific and Atlantic blocking. Section 4 provides a discussion of consistencies and inconsistencies in general circulation and blocking biases in the models. Section 5 is the conclusion.

3.2 Data and Methods

3.2a General Circulation Models (GCM's)

This work analyzes general circulation and blocking in Geophysical Fluid Dynamics Laboratory's (GFDL) atmosphere-only model AM4 (Zhao et al. 2018) and coupled atmosphere-ocean model CM4 (Held et al. 2019). Previous studies have shown strong agreement between GFDL blocking simulations and corresponding CMIP ensemble means (Masato et al. 2013; Davini et al. 2016). AM4 is computed at roughly 100-km resolution with 33 vertical levels. AM4 is forced with prescribed time-evolving sea surface temperatures (SST's) and sea-ice distributions. AM4

serves as the atmospheric component for the coupled model CM4, which is part of the Coupled Model Intercomparison Project 6 (CMIP6) ensemble. CM4 consists of AM4 coupled to the ocean model version 4, i.e., OM4 (Adcroft et al. 2019).

Atmospheric features produced by the GFDL models are compared with ECMWF ERA5 reanalysis (Hersbach et al. 2020). ERA5 is produced at roughly 30 km horizontal resolution with 137 vertical levels. For all models in this paper, daily mean data is interpolated into 2.0° by 2.5° latitude by longitude grids. We focus only on winter defined as December, January, and February (DJF) from 1980-2014.

3.2b Stationary Wave and Mean Zonal Wind

Two blocking-relevant general circulation features are examined within this paper: the stationary wave and zonal wind. Results presented in this paper for the stationary wave and the zonal wind were not strongly impacted by the inclusion or removal of blocked gridpoints in each respective calculation.

The stationary wave is calculated using the 500 hPa geopotential height field (Z_{500}). The stationary wave at each gridpoint, Z_{500}^* , is defined using the equation $Z_{500}^* = \overline{Z_{500}} - [\overline{Z_{500}}]$. Here, overbars indicate the DJF time-mean, and brackets indicate the zonal mean. The time mean of the 250 hPa zonal wind is defined as, $\overline{U_{250}}$. This is the DJF climatology of the upper-level jet. We also analyze the zonal mean of the zonal wind climatology: $[\overline{U}]$.

3.2c Block Tracking, Climatology, and Regional Sorting

To identify and track blocks, this work implements the Z_{500} metric described by Dunn-Sigouin and Son (2013, DS13 herein). This hybrid metric searches for strong positive anomalies in Z_{500} (Z_{500}') that reverse the meridional gradient of Z_{500} . The anomalies are calculated at each

point in space by removing a running annual mean and mean seasonal cycle, similar to a 30-day high-pass filter. To identify blocking candidates, the tracking algorithm implements several thresholds on contiguous Z_{500}' anomalies:

6. Positive anomaly amplitude of at least 1.5 standard deviations
7. Area of at least $2.5 \times 10^6 \text{ km}^2$
8. Meridional Gradient Reversal of Z_{500} as described in DS13
9. Quasi-stationary condition: 50 % area overlap between successive timesteps
10. Satisfaction of the above criteria for at least 5 days

We choose this metric due to its straightforward implementation, as well as its ability to capture high-amplitude wave breaking events (DS13). Barnes et al. (2012) found that similar Z_{500} metrics yield similar blocking properties and climatological features compared to potential temperature or vorticity-based metrics. For specific details of the tracking algorithm, the reader is referred to DS13.

For each timestep at each gridpoint, the block tracker yields a block identification flag of 1 or 0 corresponding to the presence and absence, respectively, of blocking. Climatological spatial distributions of blocking frequency, hereinafter referred to as the blocking climatology, are computed by averaging 2D, lat-lon grids of block identification flags over all DJF days. Note, in this work, blocking frequency indicates the percentage of DJF timesteps that a gridpoint was identified as blocked, not the number of individual events. The blocking climatology for DJF in ERA5 from 1980-2014 is shown in Figure 3.1a.

Previous studies have found distinct differences between Pacific and Atlantic blocking in the Northern Hemisphere (Hartmann and Ghan 1980; Nakamura et al. 1997). Furthermore, within general circulation models, blocking simulation biases in the Pacific and Atlantic are often in

disagreement in terms of sign and magnitude (Matsueda et al. 2009; Masato et al. 2013). Thus, for this study, blocking is sorted into two major regions of study: the Pacific region, and the Atlantic region. These regions are indicated by the red boxes in Figure 3.1a.

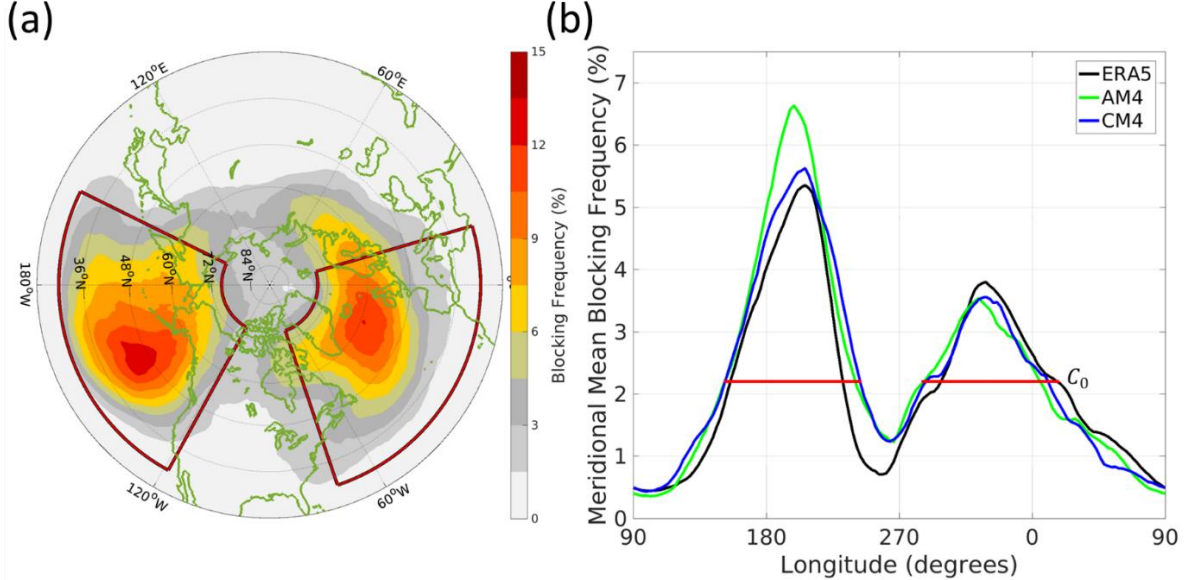


Figure 3.1. (a) Blocking climatology (shading), C , for ERA5 averaged over December, January, and February (DJF). Red boxes show the boundaries used to define the Pacific and Atlantic regions. (b) Area-weighted meridional mean of the midlatitude DJF blocking climatology, \tilde{C} , in ERA5, AM4, and CM4. The horizontal red lines denote the Pacific and Atlantic regions. C_0 is the minimum blocking frequency used to define each region.

The spatial extent of these regions is determined as follows. The DJF blocking climatology, C , for ERA5, AM4, and CM4 is separately calculated. Next, the area-weighted meridional-mean of C , \tilde{C} , is calculated between 30° N - 75° N for reanalysis and for each GFDL model (Fig. 3.1b); For this, the southern boundary of 30° N is set by the tracking algorithm and the northern limit is chosen to exclude polar blocking (see Berrisford et al. 2007 for more discussion on polar blocking). $[\tilde{C}]$ is the zonal mean of \tilde{C} , and it represents the area-weighted blocking frequency within the midlatitudes of each model. For ERA5, AM4, and CM4, $[\tilde{C}]$ is equal to 2.0, 2.17, and 2.16 % respectively.

Fig. 3.1b shows two distinct peaks in \tilde{C} where blocking is most ubiquitous. These correspond to the Pacific and Atlantic blocking maxima in Fig. 3.1a. To define the Atlantic and Pacific regions, peaks in \tilde{C} with values above a threshold C_0 are identified in each model. C_0 is defined as the minimum of $[\tilde{C}]$ across all models and equals 2.0%. The eastern and western limits of each region are defined as the longitudes at which any model exceeds C_0 (the horizontal line in Fig. 3.1b). This is done to capture the greatest area and account for any zonal shifts in blocking. Based on this methodology, the Pacific and Atlantic regions span 153.75° - 241.25° and 288.75° - 16.25° , respectively.

In our analysis of block duration, we have to account for the fact that some blocks move out of the study region during their individual lifecycles. In order to avoid miscounting, we classify the blocks based on their origin, and we keep track of their lifecycles based on their time within the study regions as follows. A block is classified as originating in the Pacific or Atlantic if the location of its Z_{500}' maximum falls within the respective region during the block's first timestep. Block area is defined as the contiguous area of blocked pixels – even if some of the block is located outside of the study region. For Pacific and Atlantic classified blocks, regional block duration is defined as continuous timesteps from the onset of the block until the block area has less than 50 % of the tracking algorithm's area threshold ($2.6 \cdot 10^6 \text{ km}^2$) within the region. Block area, duration, and compositing results are robust to changes +/- 10° to the region boundaries.

3.2d Transient Eddy Forcing: Wave Activity Flux

Wave activity flux, \mathbf{W} (Takaya and Nakamura 2001, TN01 hereinafter), can be described as the “ageostrophic flux of geopotential” and represents the pseudo-momentum of Rossby waves. Convergent \mathbf{W} indicates the halted propagation and absorption of these waves (TN01). \mathbf{W}

convergence tends to decrease zonal flow, increase the amplitude of quasi-stationary Rossby waves, and accompanies wavebreaking (Wolf and Wirth 2017), reinforcing blocked flows (TN01).

\mathbf{W} is defined as follows:

$$\mathbf{W} = \frac{p \cos \phi}{2|\mathbf{U}|} \begin{pmatrix} U \left(v'^2 - \frac{\Phi'}{f} \frac{\partial v'}{\partial x} \right) + V \left(-u'v' - \frac{\Phi'}{f} \frac{\partial v'}{\partial y} \right) \\ U \left(-u'v' + \frac{\Phi'}{f} \frac{\partial u'}{\partial x} \right) + V \left(u'^2 + \frac{\Phi'}{f} \frac{\partial u'}{\partial y} \right) \end{pmatrix} \quad (\text{Eq. 1})$$

At a given pressure level, u' , v' , and Φ' are the 6-day high-pass filtered zonal wind, meridional wind, and geopotential, respectively. The background flow, \mathbf{U} , contains 30-day low-pass-filtered zonal wind, U , and meridional wind, V . p is the pressure, f is the Coriolis parameter, and ϕ is latitude. This quantity is computed at 5 pressure levels between 950-250 hPa and then vertically integrated for the block-centered compositing analyses in this paper.

We note that the phase propagation term in the TN01 formulation is omitted in our analysis. This is due to difficulties in accurately calculating phase speed on all pressure levels for each model. However, in a comparison with the results of Wolf and Wirth (2017), the stationary term was found to dominate (not shown). In addition, case study analyses of blocking using \mathbf{W} as calculated above (Figure 3.2) yield results that are physically consistent with previous dynamical descriptions of blocking (e.g., TN01 and Paradise et al. 2019).

During block onset, the 6-day high-pass-filtered geopotential height field (Fig. 3.2a) features high-pressure within a Rossby wave pattern entering the blocked region, joining pre-existing anticyclonic air south of Greenland (Fig. 3.2b). Here, \mathbf{W} points along the direction of the alternating cyclonic/anticyclonic anomalies (Fig. 3.2a). On the upstream-equatorward flank of the block there is strong \mathbf{W} convergence (Fig. 3.2b). This convergence of eddy momentum indicates

transient eddy forcing of the block as it strengthens (Shutts 1983; Takaya and Nakamura 2001; Yamazaki and Itoh 2013a; Yamazaki and Itoh 2013b).

Block-centered compositing results, which average over many wave phases, also show results consistent with the case study described above during block onset. In addition, it is generally true that phase speed tends to zero near the upstream flank of blocked flows (Nakamura and Huang 2018), which would act to suppress the phase propagation term in the complete TN01 formulation. Thus, we take \mathbf{W} , as described above to suffice for the analysis within this paper.

3.2e Block-centered Compositing

To assess any biases in background flow and high-frequency forcing during blocking onset, block-centered compositing is implemented following the methods of Narinesingh et al. (2020). In this work, Z_{500} , Z_{500}' , 250 hPa U (U_{250}), and vertically integrated \mathbf{W} are composited. Note, U_{250} represents the 30-day lowpass filtered zonal wind field as described in the \mathbf{W} formulation.

To construct the composites, a given field around the Z_{500}' maximum of each block is collected and projected onto an equal-area grid. This is carried out for the onset phase of each block, defined as the first two days the block was recognized by the tracking algorithm. Then, the average over all blocks originating in a given region (Atlantic or Pacific) is computed.

3.2f Statistical Significance Testing

To discern statistically significant differences between the GFDL models (AM4 and CM4) and reanalysis (ERA5), the Mann-Whitney u test is employed. One advantage of the u test over other methods such as the t test, is that it the u test is non-parametric. For each year in each model, the blocking climatology is calculated. Then, for each gridpoint, u tests are performed between the distributions of the annual blocking frequency in ERA5 and the distributions of annual blocking frequency in AM4 or CM4 at that gridpoint. The comparison of the distributions gives a robust,

non-parametric approach for quantifying the differences in the blocking climatologies. A 95 % confidence interval is imposed throughout this paper. The same procedure is followed for the stationary wave and jet analyses.

The block-centered compositing analysis also utilizes the u test. For ERA5, a given field around the centroid of each block in the region of interest is collected and put into a three-dimensional matrix with dimensions longitude by latitude by block number. The same is done for the GFDL models. Then at each corresponding gridpoint relative to the block centroid, u tests are performed between ERA5 and the GFDL models.

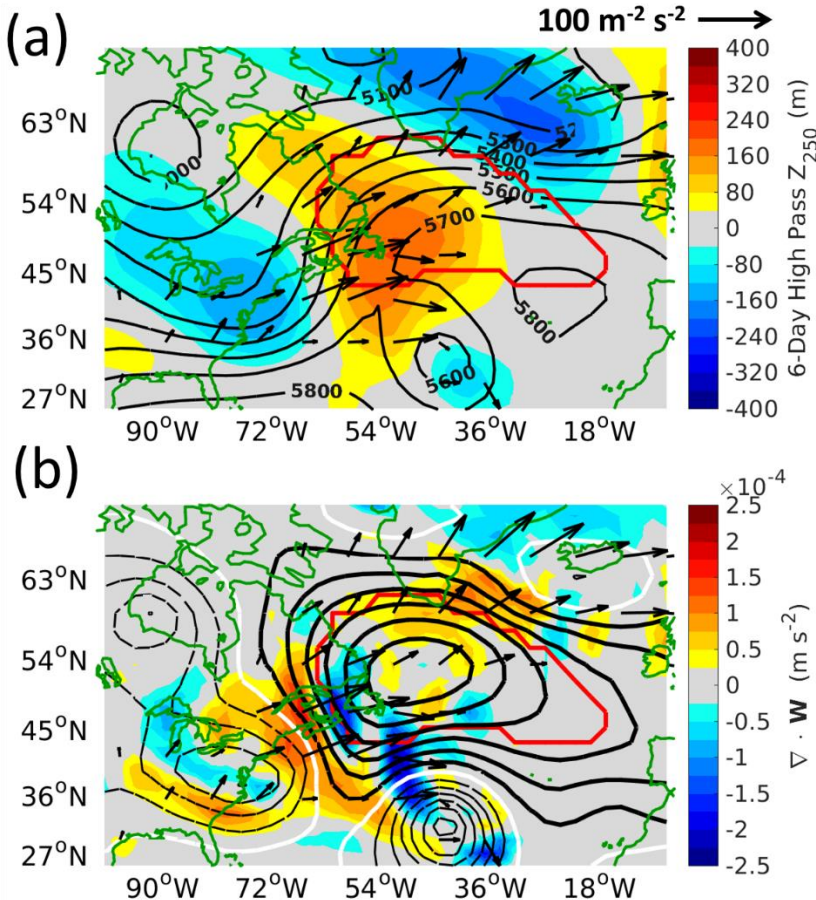


Figure 3.2. Case-study example for the first day of an Atlantic blocking episode on 4 February 1983: (a) 6-day high-pass-filtered 250 hPa geopotential height, Z_{250} (shading), and unfiltered 500 hPa geopotential height in meters (contours). (b) Divergence of 6-day high-pass-filtered wave activity flux, $\nabla \cdot \mathbf{W}$ (shading), and 500 hPa geopotential

height anomaly as defined by the DS13 block tracking algorithm (contours). In (b), thick (thin dashed) black contours indicate positive (negative) geopotential height anomalies with outer contour 50 m (-50 m) and a 50 m (-50 m) contour interval. Thick white contour in (b) indicates 0 m height anomalies. In (a) and (b) the red contour indicates the blocked region as detected by the DS13 algorithm and black arrows show 6-day high-pass-filtered \mathbf{W} .

3.3 Results

3.3a General Circulation Features

Tung and Lindzen (1979) suggested that blocking is the product of resonant amplification of stationary waves by transient eddies. Also, stronger stationary waves in idealized models lead to a non-linear increase in blocking (Paradise et al. 2019; Narinesingh et al. 2020). The zonal wind also plays a key role in blocking: on one hand a stronger instantaneous jet carries greater momentum and is thus more difficult to halt; but on the other hand, blocking frequency is greater in winter than summer (e.g., Pfahl and Wernli, 2012), when the time-mean jet (and baroclinicity) is stronger as compared to summer (explored in idealized models in Hassanzadeh et al. 2014). Due to the importance of the stationary wave and upper-tropospheric zonal wind to blocking, we begin by analyzing their representation in the models.

3.3a.i Stationary Wave

The stationary wave pattern (Fig. 3.3) over the northern Pacific basin is generated by the orography and land-sea forcing of Asia and North America, as well as forcing from the tropical Pacific (Held et al. 2002; White et al. 2017; Park and Lee 2021). It features a low pressure, baroclinically rich region in the basin entrance (Chang et al. 2002) that is flanked on its equatorward side by the Pacific upper-level jet maximum (Figs. 3.3 and 3.5). On the downstream side of the ocean basin, there is an anticyclonic stationary wave anomaly forced primarily by the

Rocky Mountains and the overall North American topography (Broccoli and Manabe 1992). In the Atlantic Basin, an east-west, high-low stationary wave dipole is observed (Fig. 3.3), similar to the Pacific. This is primarily due to land-sea contrast and topography of both North America and Europe (Seager et al. 2002), and to a lesser extent, the Gulf Stream (Brayshaw et al. 2009).

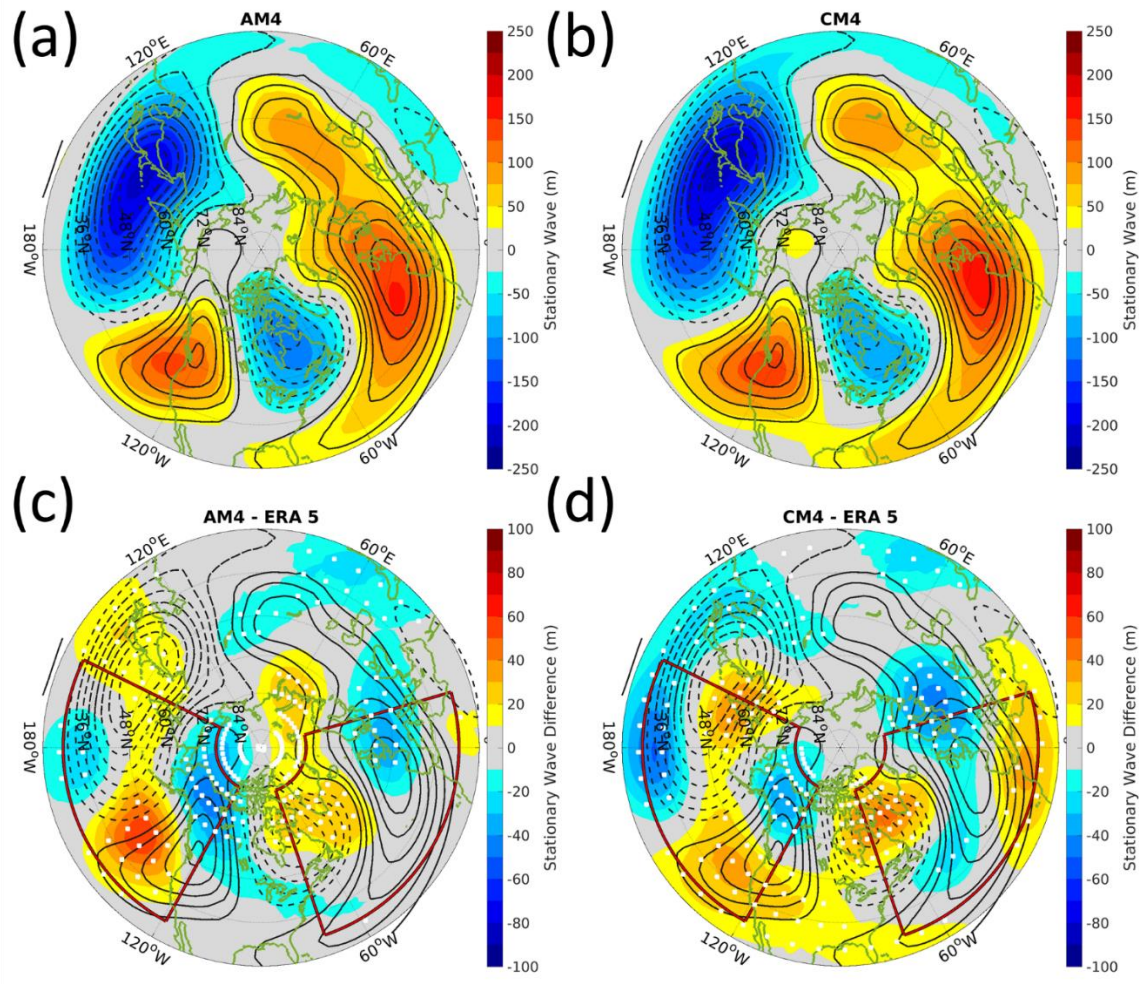
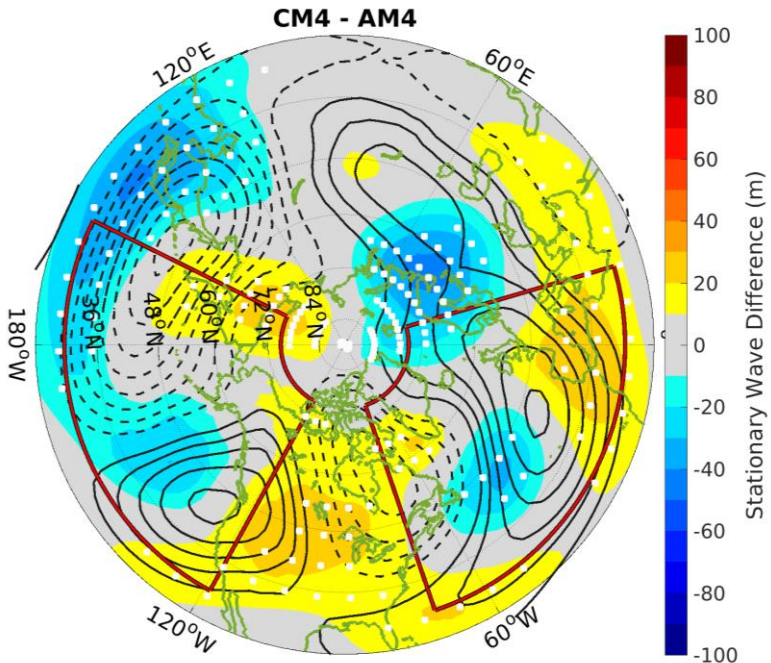


Figure 3.3. (a-b) DJF Stationary wave at 500 hPa (Z_{500}^*) for ERA5 (contours), and the GFDL models (shading): (a) AM4, and (b) CM4. (c-d) Z_{500}^* for ERA5 (contours) and Z_{500}^* in the GFDL models minus reanalysis (shading) for (c) AM4 and (d) CM4. Solid and dashed contours in (a-d) show the positive and negative Z_{500}^* , respectively. The outer contour for the solid (dashed) contours is 25 m (-25 m) and the contour interval is 25 m (-25 m). White stippling in (c-d) denotes regions where Z_{500}^* in the GFDL models differ significantly from ERA5 reanalysis.

Figure 3.4. Z_{500}^* for AM4 (contours) and Z_{500}^* in CM4 minus AM4 (shading). Solid and dashed contours show the positive and negative Z_{500}^* , respectively. The outer contour for the solid (dashed) contours is 25 m (-25 m) and the contour interval is 25 m (-25 m). White stippling denotes regions where Z_{500}^* in the CM4 differs significantly from AM4.



AM4 and CM4 produce qualitatively similar stationary wave patterns compared to reanalysis (Figs. 3.3a-b), though some biases exist (Figs. 3.3c-d). Near the Atlantic and Pacific blocking maxima (Fig. 3.1a), both models share similar biases (Figs. 3.3c-d). In the Pacific, the positive stationary anomaly over the eastern Pacific Ocean is significantly enhanced and biased towards the southwest in both models but decreases over land towards the pole (Figs. 3.3c-d). For the Atlantic dipole pattern in Z_{500}^* , a significant decrease in amplitude is found within the GFDL models, i.e., the low-pressure anomaly is not low enough and the high-pressure anomaly is not high enough.

Overall, AM4 has less stationary wave biases than CM4, but both models share similar biases in regions where blocking is most ubiquitous (Fig. 3.1 and Fig. 3.3). In the Pacific region, AM4 contains a rms error of 24.8 m whereas CM4 contains an error of 23.4 m. Little significant difference is found between the models in this region (Fig. 3.4). In the Atlantic region, CM4 contains a higher regional rms error value (20.2 m) compared to AM4 (15.8 m), however, this disagreement is not significant over the whole region; It is driven locally by a more positive

stationary wave around Northern Africa (Fig. 3.3 and Fig. 3.4), where blocking occurs only 0-3% of winter days (Fig. 3.1).

3.3a.ii Zonal Background Flow

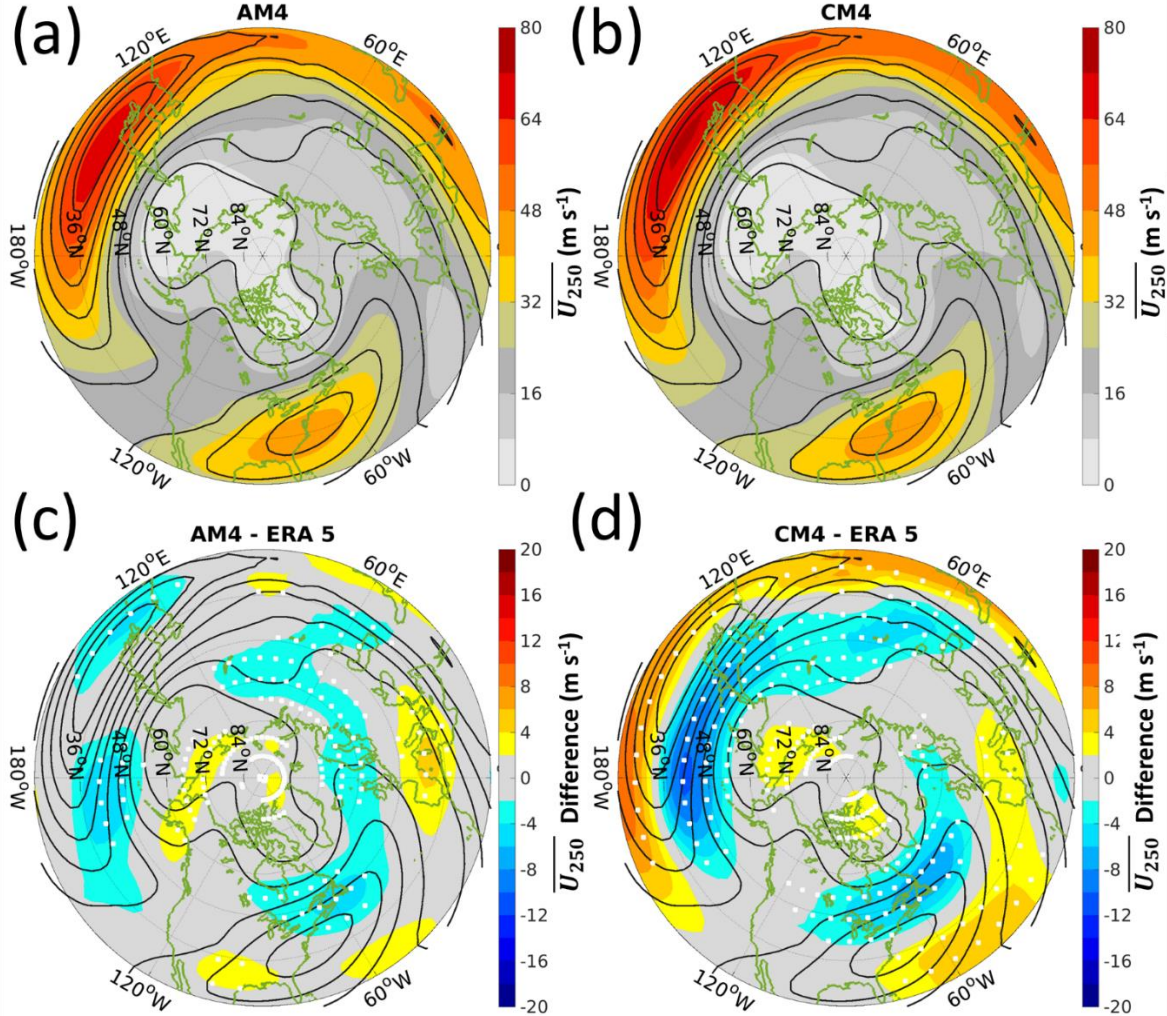


Figure 3.5. (a-b) DJF mean zonal wind at 250 hPa, $\overline{U_{250}}$ for ERA5 (contours) and the GFDL models (shading): (a) AM4, and (b) CM4. (c-d) $\overline{U_{250}}$ for ERA5 (contours) and $\overline{U_{250}}$ in the GFDL models minus ERA5 (shading): (c) AM4 and (d) CM4. The outer contour is 8 m s⁻¹, and the contour interval is 8 m s⁻¹. White stippling in (c-d) denotes regions where the $\overline{U_{250}}$ in the GFDL models differs significantly from ERA5 reanalysis.

Figure 3.5 shows the time mean zonal wind at 250 hPa ($\overline{U_{250}}$) for the GFDL models. Both models capture two localized jet maxima, one in the Pacific, and another, tilted jet maximum in

the Atlantic (Figs. 3.5 a-d). For reference, we note that just poleward and downstream of these jet maxima lie the storm tracks, where transient eddy activity maximizes (Hoskins and Hodges 2002; Narinesingh et al. 2020).

Overall, the jet in CM4 has a much larger bias than AM4 (Figs. 3.5c-d). In the Pacific, the jet maximum is equatorward of that in reanalysis (Fig. 3.5d), whereas the jet in AM4 has no such bias (Fig. 3.5c). In the Atlantic, the equatorward bias of the jet maxima in CM4 is greater than AM4 (Fig. 3.6a). Consistent with this, differences in the zonal mean zonal wind in AM4 are minimal (Fig 3.6b), whereas the biases in CM4 indicates a notable equatorward shift in the jet (Fig 3.6c).

In a previous version of the GFDL GCM, Delworth et al. (2006) also found an equatorward shift in zonal circulation when comparing a coupled model with an atmosphere-only model. This shift was associated with an equatorward contraction of the subtropical gyre and Hadley cell, and it contributed to cold biases in SST in the coupled model (Delworth et al. 2006). Clearly, CM4 exhibits a similar contraction of midlatitude circulation compared to AM4, and this has been documented previously (Held et al. 2019). Consistent with this atmospheric circulation change, there is a cold bias in the coupled model SST in both the Atlantic and Pacific (Fig. 3.7a). Held et al. (2019) suggest that the contraction of CM4's midlatitude circulation is a result of tropical cold biases in the upper troposphere, with lesser contribution from extratropical SST biases. The causes of the equatorward shift in CM4's zonal winds pose interesting research questions; however, it is beyond the scope of this work. With relevance to blocking, one main message of this section is that CM4's zonal background flow has a much larger bias than AM4.

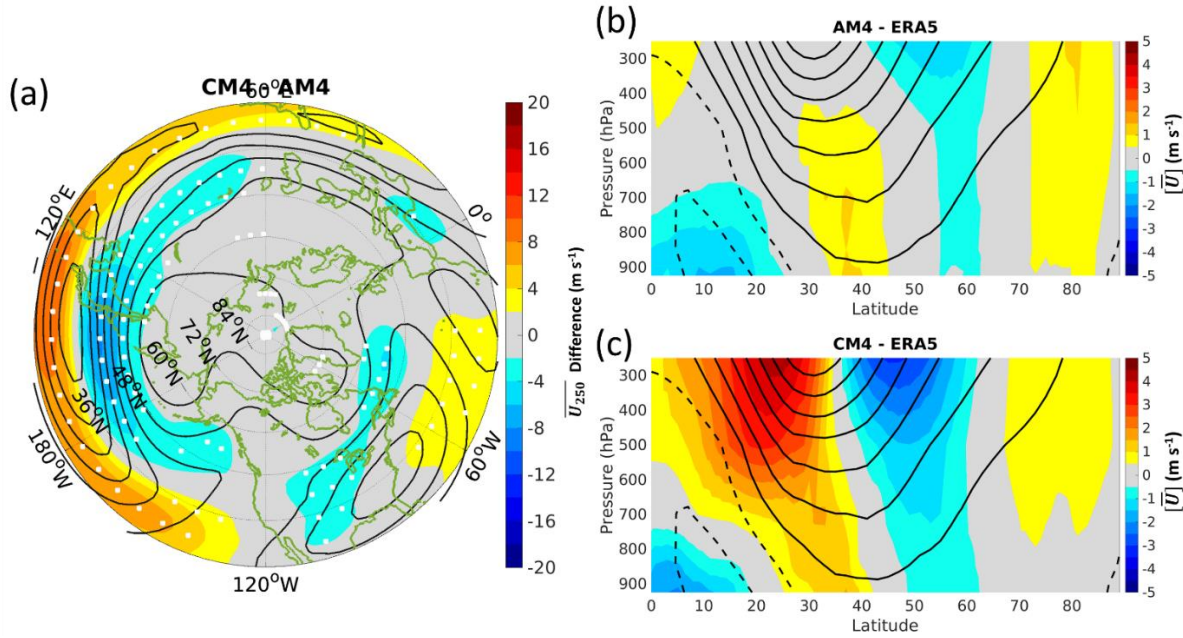


Figure 3.6. (a) \overline{U}_{250} for AM4 (contours) and \overline{U}_{250} in CM4 minus AM4 (shading). The outer contour is 8 m s^{-1} , and the contour interval is 8 m s^{-1} . White stippling indicates regions where \overline{U}_{250} in CM4 differs significantly from AM4. (b-c) DJF zonal mean zonal wind, $[\overline{U}]$, for ERA5 (contours) and DJF zonal mean zonal wind for (b) AM4 and (c) CM4 minus ERA5 (shading). Solid (dashed) contours in (b-c) indicate positive (zero and negative) zonal wind values with outer contour 5 m s^{-1} (0 m s^{-1}) and contour interval 5 m s^{-1} (-5 m s^{-1}).

The forcing of the midlatitude atmosphere by the ocean in the winter is strongly related to meridional SST gradients, especially at the western boundary currents (e.g., Hoskins and Valdes 1990). Therefore, we also analyzed SST gradients for the models (Fig. 3.7b-c). Over the west Pacific and Atlantic Oceans CM4 has weaker gradients in the midlatitudes compared to AM4. These differences in SST gradients likely contribute to the biases in the zonal wind. But it is interesting to note that the Atlantic SST biases are as large as those in the Pacific, whereas the zonal wind biases are much larger in the Pacific. This supports the suggestions of Held et al. (2019) discussed above, which states that the zonal wind biases are more dependent on tropical forcing

biases than midlatitude SST biases. For the purposes of this paper, a key takeaway is this: due to biases in the coupled model, the SST gradients in CM4 are weaker than those in AM4.

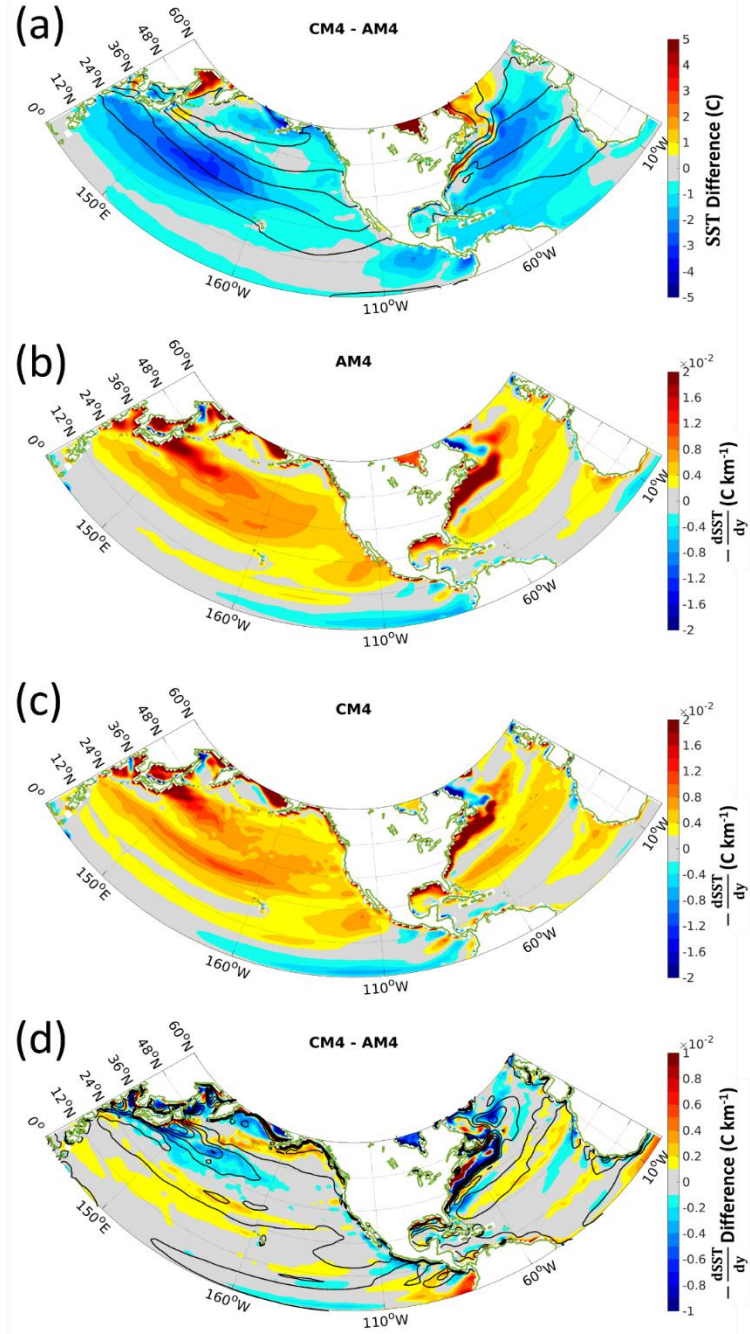


Figure 3.7. (a) Sea surface temperature (SST) in AM4 (contours) and difference in SST between CM4 and AM4 (shading). The outermost contour is 30°C and the contour interval is 5°C. (b-c) Negative of the meridional gradient of SST (shading) in (b) AM4 and (c) CM4. (d) Negative meridional gradient of SST in AM4 (contours) and difference between CM4 and AM4 (shading). The outer contour is 0°C km $^{-1}$ and the contour interval is .01°C km $^{-1}$.

3.3b Blocking Climatology

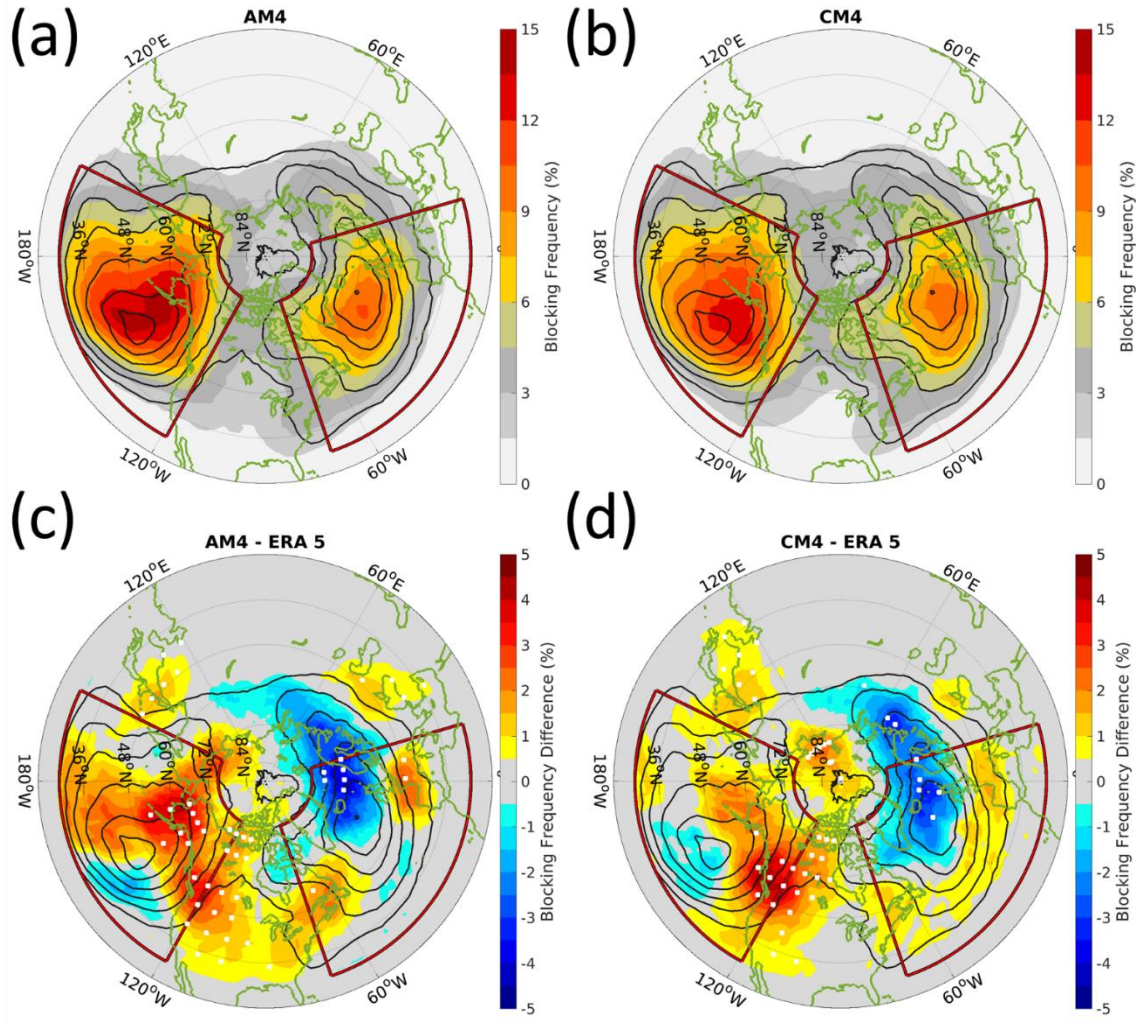


Figure 3.8. (a-b) DJF blocking climatology for ERA5 (contours) and in the GFDL models (shading): (a) AM4, and (b) CM4. (c-d) Blocking climatology for ERA5 (contours) and GFDL models minus ERA5 (shading): (c) AM4 and (d) CM4. The outer contour and contour interval are both 2 %. White stippling in (c-d) denotes regions where the blocking climatology in the GFDL models differs significantly from ERA5 reanalysis.

Figure 3.8 shows the winter blocking climatology for ERA5, AM4, and CM4. Both GFDL models produce a pattern in the blocking climatology that is qualitatively similar to reanalysis (Figs. 3.8a-b) and consistent with previous findings (Tyrrell and Hoskins 2008; Dunn-Sigouin and Son 2013). The blocking climatology features a bimodal pattern with a Pacific maximum just

equatorward of the Aleutian Peninsula, and an Atlantic maximum near Greenland that extends into Europe.

Overall, the blocking climatologies of AM4 and CM4 are similar and share various common biases. In both models too much blocking is generated along the northeastern Pacific coastline (Figs. 3.8c-d), with significant excess found near the Rocky Mountains. In the Atlantic region, both GFDL models simulate a significant lack of blocking in the Icelandic Basin extending into Northern Europe, and an excess of blocking near the Azores High. In line with those biases, the Atlantic blocking maximum is shifted roughly 7.5° south in both GFDL models (Figs. 3.8c-d).

Figure 3.9a shows the differences in the blocking climatology between CM4 and AM4. In the Pacific region CM4 produces less blocking than AM4, however this is not significant and occurs within a region of large interannual blocking variability (Fig. 3.9b; Tyrlis and Hoskins 2008). In fact, no significant differences are found between the blocking climatologies of AM4 and CM4 in the Pacific and Atlantic regions.

To quantify regional biases in blocking frequency, for a given region we define the Normalized Root Mean Square Error, F as the following:

$$F = \frac{\sqrt{\frac{1}{A} \sum_{n=1}^N (f_n - \hat{f}_n)^2 \cdot a_n}}{\frac{1}{A} \sum_{n=1}^N \hat{f}_n \cdot a_n} \quad (\text{Eq. 2})$$

A is total area, N is number of gridpoints, f_n is the GFDL blocking frequency at a gridpoint n , \hat{f}_n is the ERA5 blocking frequency, and a_n is area of n . F is essentially a measure of the error in blocking frequency normalized by the area weighted average of blocking frequency in the region (denominator in Eq. 2).

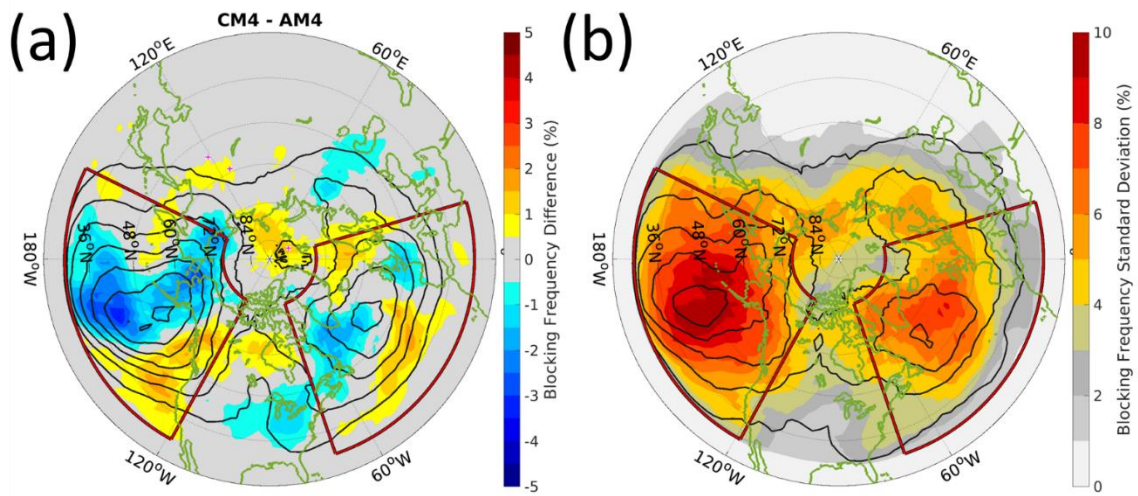


Figure 3.9. (a) Blocking climatology for AM4 (contours) and CM4 minus AM4 (shading). Magenta stippling indicates regions where the blocking climatology in CM4 differs significantly from AM4. (b) Standard deviation of the blocking climatology in AM4 (contours) and CM4 (shading). The outer contours and contour interval are both 2 % in (a) and (b).

Both models show similar amounts of error (Table 3.1) except in the Pacific region, where CM4 has roughly 25 % less error than AM4. This is significant using a u-test across all years. Still, the errors found here are similar in terms of relative magnitude, and within a region of high variability (Fig. 3.9b). The Atlantic and entire midlatitude regions also contain less error in CM4 than AM4, however these differences are not significant. These results were found to be robust to changes +/- 10 degrees in the eastern and western limits, +/- 5 degrees to the northern limit, and +/- 5 degrees to the southern limit of each region. Note that the block tracking algorithm only searches for blocks poleward of 30 degrees.

The relative agreement in error over the entire midlatitudes further emphasizes the similarities in climatological blocking biases between the models, albeit with some compensating errors. This is despite there being major disagreement between the zonal circulation (Figs. 3.5 and 3.6) and SST (Fig. 3.7) in both models. This will be commented on further in the discussion section.

	Pacific Region	Atlantic Region	All Midlatitudes
AM4	.29*	.27	.34
CM4	.23	.23	.32

Table 3.1. Normalized RMS error, F (Eq. 2), for regional blocking in AM4 and CM4 compared against ERA5 reanalysis.

All regions cover only the midlatitudes (30° - 75° N). The Pacific, Atlantic, and All Midlatitude regions extends longitudinally from 153.75° - 241.25° , 288.75° - 16.25° , and 0° - 360° , respectively. “*” indicates significant differences between the models.

3.3c Block Count, Duration, and Area

To gain better insight into the drivers of the blocking frequency biases, we next analyze block event statistics. Table 3.2 shows the duration and mean number of blocking events per year for the reanalysis and GFDL models by region. In the Pacific region, the GFDL models are in close agreement with ERA5 in terms of number of events per year but simulate an almost 1-day longer average duration. This difference is not statistically significant, however, due to a large standard deviation in block duration, but the difference is consistent with the enhanced amount of blocking in the Pacific. AM4 and CM4 also produce Pacific blocks whose individual sizes are roughly 0.5 and 0.4 million km² larger than those in reanalysis, respectively (Table 3.3). This difference is not statistically significant because of the large spread in block sizes.

In the Atlantic region, less blocking is simulated in the GFDL models compared to reanalysis (Table 3.2). A similar number of events per year is found, but the GFDL models have a lower, albeit not significant, average duration of .6-.7 days (Table 3.2). This decrease in duration agrees with the decrease in blocking frequency (Figs. 3.8c-d). In terms of area, Atlantic blocks

tend to be similar in size across all models and have a smaller average area than Pacific blocks (Table 3.3).

	Pacific Region Regional Block Duration (days) / Standard Deviation (days) / Mean # of Events per DJF	Atlantic Region Regional Block Duration (days) / Standard Deviation (days) / Mean # of Events per DJF
ERA5	8.3 / 5.2 / 3.8	8.5 / 3.9 / 1.9
AM4	9.2 / 6.2 / 4.1	7.8 / 3.5 / 2.2
CM4	9.0 / 6.0 / 3.9	7.9 / 4.9 / 2.0

Table 3.2. For ERA5 reanalysis and both GFDL models (AM4 and CM4), block duration, standard deviation of block duration, and mean number of events per DJF in each region.

To summarize, Pacific blocks in the GFDL models are, on average, slightly more persistent and larger and those in reanalysis. Atlantic blocks in the GFDL models are similar in size to reanalysis, but there is suggestion of shorter average durations. However, we cannot discount the possibility that these differences for the both the Pacific and Atlantic are due to natural variability rather than being a systematic bias. That being said, these results are consistent with biases in the blocking climatology (which are statistically significant) –too much blocking in the Pacific, and too little in the Atlantic.

	Pacific Region Mean Block Area (10^6 km^2) / Standard Deviation (10^6 km^2)	Atlantic Region Mean Block Area (10^6 km^2) / Standard Deviation (10^6 km^2)
ERA5	6.19 / 1.81	5.45 / 1.32
AM4	6.69 / 2.04	5.49 / 1.79

CM4	6.59 / 1.86	5.44 / 1.41
------------	--------------------	--------------------

Table 3.3. For ERA5 reanalysis and both GFDL models (AM4 and CM4), mean block area and standard deviation of block area in each region.

3.3d Zonal Background Flow During Block Onset

To assess background flow properties during the onset phase of blocking, compositing analysis of 30-day lowpass filtered zonal wind at 250 hPa (U_{250}) is performed. Figures 3.10a and 10b show these composites for the Pacific and Atlantic regions, respectively, using ERA5.

Both the Pacific and Atlantic regions feature U_{250} composite maxima upstream and poleward from the blocking center (Fig. 3.10a-b). There are also minima in composite U_{250} , downstream-equatorward of the block center for both regions. Similar patterns are found when raw 250 hPa zonal wind is composited for 30 days prior to blocking onset (not shown).

In terms of differences between regions, the Pacific Z_{500} composite during the onset phase resembles an omega or amplified ridge shape, and U_{250} is stronger (Fig. 3.10a). In the Atlantic, the diffluent flow pattern is more pronounced (Fig. 3.10b) and the Z_{500} composite contours exhibit more of an overturning consistent with anticyclonic wavebreaking (Masato et al. 2012).

AM4 (Fig. 3.10c-d) and CM4 (Fig. 3.10e-f) both capture an anticyclonic wavebreaking signature in the Atlantic and amplified ridge behavior in the Pacific. In the Pacific, AM4 exhibits no significant biases, but CM4 has an equatorward shift in composite U_{250} (Fig. 3.10e) mirroring what was found for the climatological location of the jet (Fig. 3.5b, d).

The Atlantic blocks feature no significant biases in the upstream and central blocking region for both AM4 and CM4. Downstream-equatorward of the composite block center, however, both models have enhanced zonal flow compared to reanalysis. In addition, AM4 has suppressed zonal flow downstream-poleward of the block center.

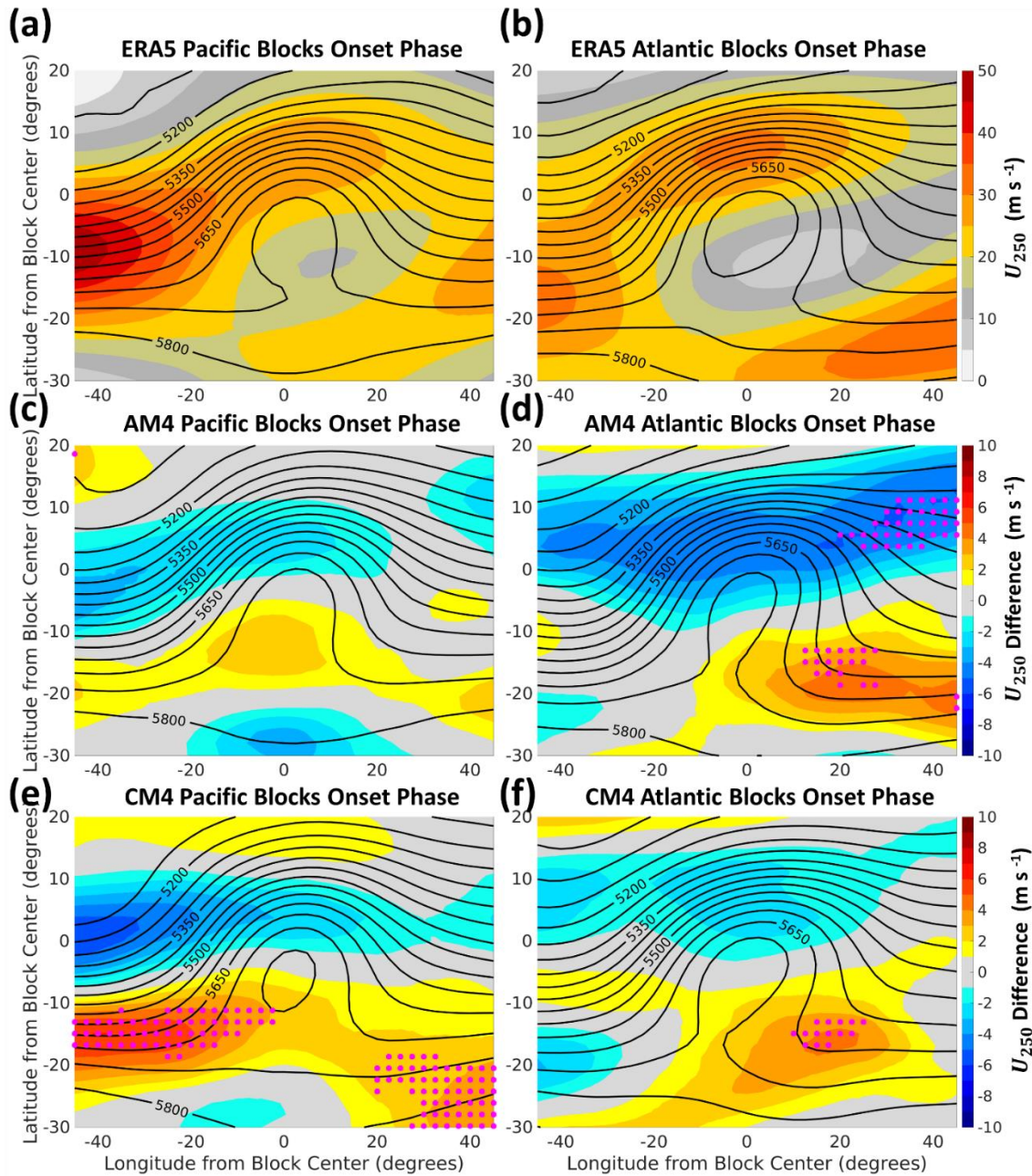


Figure 3.10. (a, b) For the block onset phase, block-centered composites of unfiltered 500 hPa geopotential height (m) (contours) and 30-day low-pass-filtered 250 hPa zonal wind, U_{250} (shading) for (a) Pacific and (b) Atlantic blocks in ERA5. (c-f) For the block onset phase, block-centered composites of unfiltered 500 hPa geopotential height (contours) and difference between block-center composited U_{250} in the GFDL models and ERA5 (shading). (c-d) Computed using AM4 for (c) Pacific and (d) Atlantic blocks. (e-f) Computed using CM4 for (e) Pacific and (f) Atlantic blocks. Magenta stippling in (c-f) indicate significant differences between the corresponding GFDL model and ERA5.

3.3e Transient Eddy Forcing During Block Onset

Convergence of transient eddy pseudo-momentum acts to reinforce blocking by slowing down the westerly flow (Hoskins et al 1983; Trenberth 1986; Takaya and Nakamura 2001) and replenishing anomalous PV (Shutts 1983; Nakamura and Wallace 1993; Yamazaki and Itoh 2013). Here, we assess the high frequency (6-day high-pass-filtered) eddy forcing of blocking in the models using the wave activity flux pseudo-momentum, \mathbf{W} .

Figure 3.11 shows block-centered composites of Z_{500}' , \mathbf{W} , and $\nabla \cdot \mathbf{W}$ for Pacific and Atlantic blocks during the onset phase. In ERA5, low pressure minima lie upstream from the composite block centers (Fig. 3.11 a-b), in agreement with previous findings (Colucci 1985, Nakamura and Wallace 1993). Similar to the case study in Figure 3.2, both regions feature a convergence of \mathbf{W} on the upstream-equatorward flank of the blocking center.

Both the Pacific (Fig. 3.11a) and Atlantic (Fig. 3.11b) high pressure centers are flanked by low-pressure minima on their equatorward sides. In the Atlantic, however, the North-South dipole axis is tilted compared to the Pacific region, perhaps related to the southwest-to-northeast orientation in the N. Atlantic's climatological circulation. The Atlantic blocks in ERA5 (Fig. 3.11b) demonstrate significantly stronger convergence compared to those in the Pacific (Fig. 3.11a).

The GFDL models (Fig. 3.11c-f) capture the same patterns of \mathbf{W} convergence as reanalysis (Fig. 3.11a-b). There is some suggestion, however, that the Atlantic blocks in AM4 (Fig. 3.11d) and CM4 (Fig. 3.11f) demonstrate less forcing, though these differences are not significant throughout the upstream-equatorward convergence area. Both models also reproduce the

differences in Atlantic (Fig. 3.11d, f) and Pacific (Fig. 3.11c, e) blocking in terms of high-low dipole orientation.

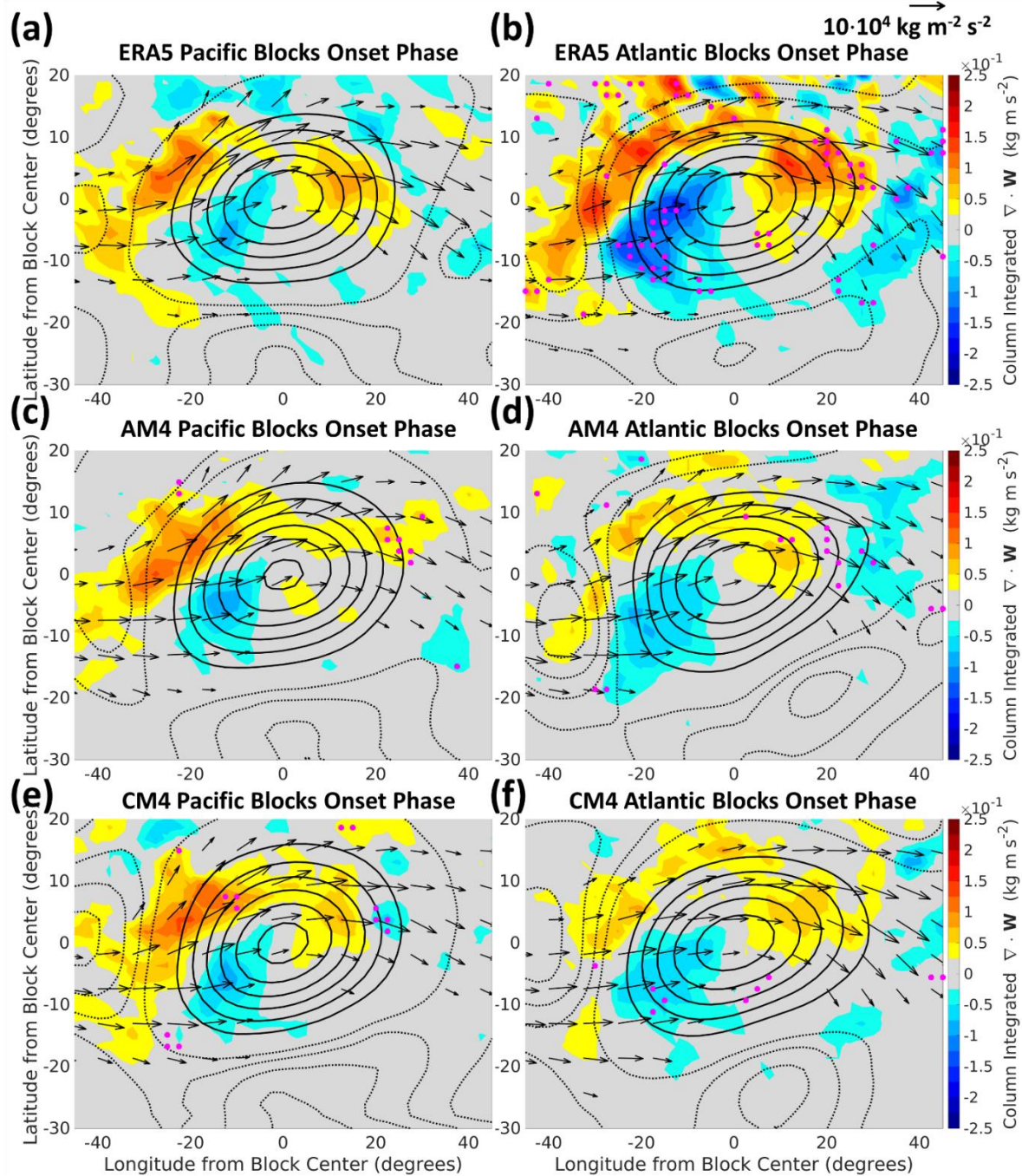


Figure 3.11. (a, c, e) For the onset phase of Pacific blocking events, block-centered composites of positive 500 hPa geopotential height anomalies (solid contours), negative 500 hPa geopotential height anomalies (dashed contours), column integrated wave activity flux, \mathbf{W} (arrows), and $\nabla \cdot \mathbf{W}$ (shading) for (a) ERA5, (c) AM4, and (e) CM4. (b, d, f) As

in (a, c, e) but for Atlantic blocks in (b) ERA5, (d) AM4, and (f) CM4. Positive (negative) geopotential height contours have an outer contour of 50 m (-20 m) and contour interval of 50 m (-20 m). \mathbf{W} is calculated using 6-day high-pass-filtered fields. Vectors with magnitudes less than $5 \cdot 10^4 \text{ kg m}^{-2} \text{ s}^{-2}$ are masked. Magenta stippling indicates significant differences in $\nabla \cdot \mathbf{W}$ between (b) ERA5's Pacific and Atlantic blocks, and (c-f) the corresponding GFDL model and ERA5.

One aspect the models fail to reproduce is the differences in magnitude of \mathbf{W} convergence between the Atlantic and Pacific regions. Aside from this however, the results of this subsection suggest that the GFDL models properly represent the onset phases of both Pacific and Atlantic blocking in terms of transient eddy forcing and geopotential height evolution.

3.4 Discussion

Using an idealized traffic-jam model, Paradise et al. (2019) and others found blocking occurrence responds to changes in the stationary wave (Tung and Lindzen 1979; Luo 2005), jet (Barnes and Hartmann 2010; De Vries et al. 2013), and eddy forcing (Shutts 1983; Yamazaki and Itoh 2013). As such, here we discuss consistencies and inconsistencies in the GFDL models regarding blocking and the aforementioned circulation features. As a reminder, we note that the jet and stationary wave analysis discussed throughout this paper were found to be insensitive to the removal or inclusion of the timesteps with blocks.

The models generate too much blocking in the Pacific region and too little blocking in the Atlantic (Fig. 3.8). In both models, this result is consistent with the enhanced positive stationary wave anomaly found in the Pacific and weakened stationary wave in the Atlantic (Fig. 3.3). This also agrees with Paradise et al. (2019), who found a positive relationship between blocking and stationary wave amplitude.

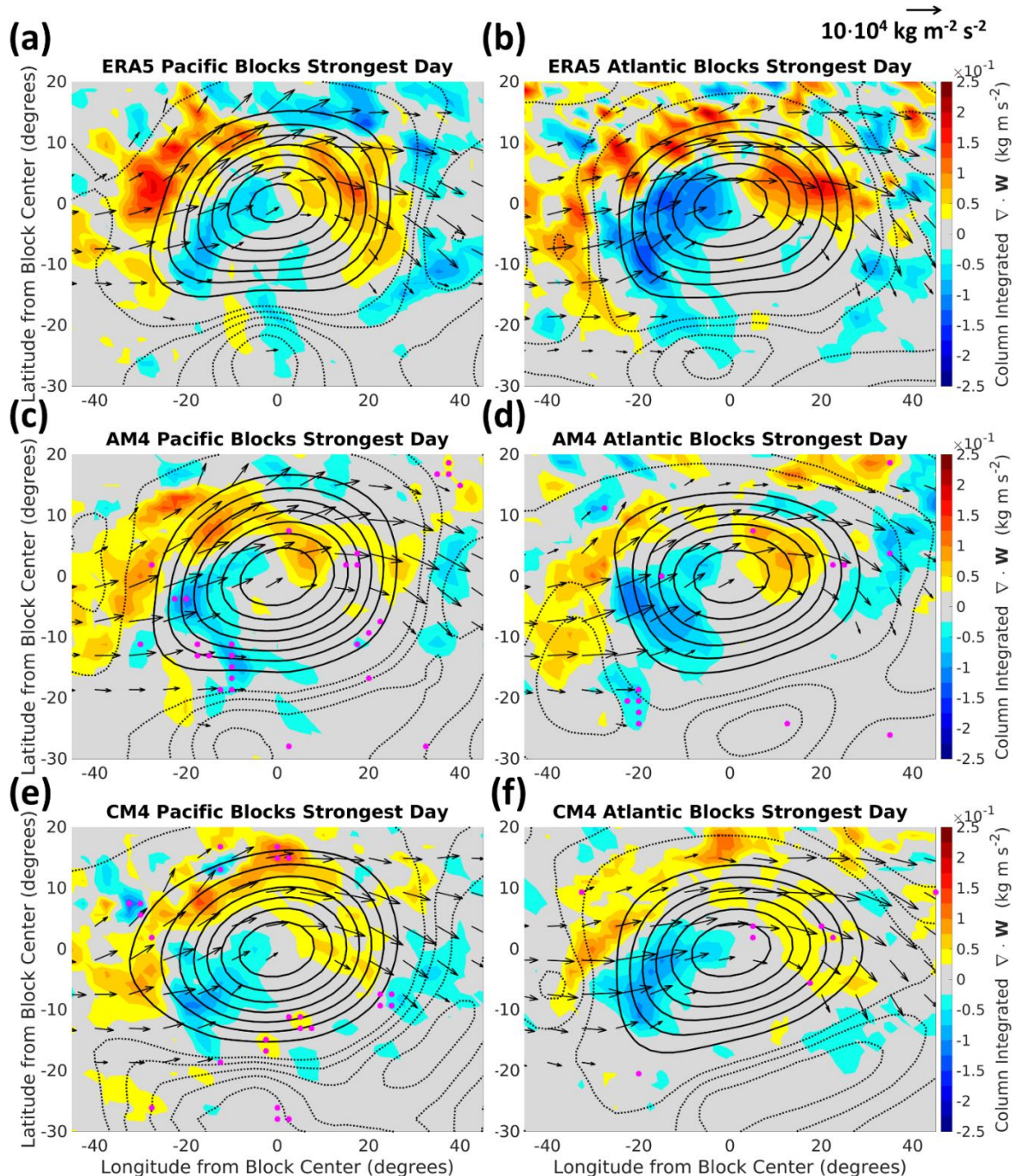


Figure 3.12. (a, c, e) For the strongest days of Pacific blocking events, block-centered composites of positive 500 hPa geopotential height anomalies (solid contours), negative 500 hPa geopotential height anomalies (dashed contours), column integrated wave activity flux, \mathbf{W} (arrows), and $\nabla \cdot \mathbf{W}$ (shading) for (a) ERA5, (c) AM4, and (e) CM4. (b, d, f) As in (a, c, e) but for Atlantic blocks in (b) ERA5, (d) AM4, and (f) CM4. Positive (negative) geopotential height contours have an outer contour of 50 m (-20 m) and contour interval of 50 m (-20 m). \mathbf{W} is calculated using 6-day high-pass-

filtered fields. Vectors with magnitudes less than $5 \cdot 10^4 \text{ kg m}^{-2} \text{ s}^{-2}$ are masked. Magenta stippling in (c-f) indicates significant differences in $\nabla \cdot \mathbf{W}$ between the corresponding GFDL model and ERA5.

The Pacific and Atlantic blocking biases shared by AM4 and CM4 are also in agreement with theory and other previous results regarding stationary waves. In the wave activity traffic jam theory of blocking developed by Nakamura and Huang (2018), an enhanced stationary wave results in a region's decreased capacity for wave activity fluxes, thus leading to blocking. Furthermore, Narinesingh et al. (2020) also found increases in blocking when an idealized moist GCM was configured into a strong stationary wave regime compared to zonally symmetric and weaker stationary wave integrations.

The relationship between the blocking climatology and the zonal wind in AM4 and CM4 are not so clear, however. Despite CM4 containing an equatorward shifted zonal flow compared to AM4 (Fig. 3.6), the models exhibit similar biases in terms of their blocking climatologies (Fig. 3.8). Barnes and Hartmann (2010) found higher blocking frequencies corresponded to equatorward jets in CMIP models. Their result agrees with the Pacific over-generation of blocks in CM4 but disagrees with CM4 and AM4's Atlantic blocking deficiencies.

CM4's Pacific blocks also contain enhanced zonal background flow on the upstream-equatorward flank of the blocking high (Fig. 3.10e), near the meridional high-low dipole (Fig. 3.11e). This is inconsistent with the findings of Paradise et al. (2019), who found decreased blocking in stronger zonal flows. In the Atlantic, the decrease in blocking near Iceland is also not expected given the weakened background flow (Fig. 3.5). In terms of transient eddy forcing during the onset phase of blocking, the GFDL models show little difference from reanalysis (Fig. 3.11). This is despite various jet biases between the models. Yamazaki and Itoh (2013b) also found results consistent to ours, where transient eddy forcing of blocks was found to be insensitive to jet strength

and placement. Taken together, these results regarding the zonal winds suggest the model biases in blocking may come from:

- (1) mean-state biases in the stationary wave or physics that is not fully captured by the models, or,
- (2) blocks in the Pacific and Atlantic having substantial differences in their interaction with the background flow, or,
- (3) aspects of blocking onset and maintenance that have not yet been considered.

Maintenance of blocking is also critical to blocking longevity (Shutts 1983; Pfahl et al. 2015). Figure 3.12 shows block centered composites of $\nabla \cdot \mathbf{W}$ during the strongest days of blocks as defined by the maximum Z_{500}' field over block lifecycles. Here we only consider blocks that remain in their region of origin based on the duration criteria described in the methods section (Section 2c). Across models, on average the strongest block days occur between days 3.5-4 in the Atlantic and days 5-5.5 in the Pacific.

Little difference is found between the GFDL models and ERA5 during the strongest day, except there is some suggestion that AM4's Pacific \mathbf{W} convergence is greater (Fig 3.12c). This could indicate enhanced transient eddy forcing, consistent with the overgeneration of blocking in the region. However, a similar difference is not found in CM4.

Herein we focus on the transient eddy maintenance of blocking through wave-activity fluxes, but other studies have found latent heating (Pfahl et al. 2015) to play a prominent role as well. Thus, a more comprehensive look at the dynamic and thermodynamic maintenance of blocking throughout their lifecycle is warranted in future study.

Overall, stationary wave biases remain the most consistent with blocking biases for the GFDL models, but the work here cannot attribute causality without more rigorous testing of the models. In future work, we plan on investigating the response of blocking to changes in the stationary wave and jet as well as dynamic and thermodynamic maintenance mechanisms. We note that such a study would need to consider the coupling between the general circulation features themselves, as well as block maintenance mechanisms.

3.5 Summary and Conclusions

GFDL's atmosphere only (AM4) and coupled atmosphere-ocean (CM4) general circulation models reproduce the overall spatial pattern of the blocking climatology (Fig. 3.8) with a similar number of events per DJF (Table 3.2). In the Pacific, however, the modeled blocking frequency is biased high compared to reanalysis. This could be due to each model's tendency to generate blocks that are spatially too large and last too long; though the large variability in block duration and area makes it difficult to conclusively say so.

In the Atlantic region, AM4 and CM4 both have less blocking than reanalysis. Here, the distribution of spatial size of individual blocks are similar to reanalysis, but there is suggestion that they are slightly less persistent, albeit with high uncertainty.

Blocking onset dynamics is also assessed within the models. In terms of the 500-hPa geopotential height field, both models produce differences between Pacific and Atlantic blocking that match with observations (Fig. 3.10). In the Pacific, the Z_{500} field features an amplified ridge during blocking onset, whereas in the Atlantic, a signature of anticyclonic wavebreaking is found.

The background zonal flow during block onset is generally captured within the models (Fig. 3.10), except CM4 features an equatorward shift for Pacific blocks. In terms of high-frequency

eddy forcing during blocking onset, both models produce similar patterns in wave activity flux convergence compared to reanalysis (Fig. 3.11). The models do not, however, produce the stronger convergence found for Atlantic blocking compared to Pacific.

Our analysis of general circulation features previously shown to influence blocking revealed a mixture of results. First, both models capture the overall spatial pattern of the stationary wave (Z_{500}^* ; Fig. 3.3), however some biases exist. In the Pacific region, AM4 and CM4 produce an enhanced positive stationary wave anomaly. In the Atlantic, the amplitude of the stationary wave is too small in both models (Fig. 3.3). These biases match in location and sign with the biases in blocking, and the biases are present even if only the timesteps without blocking are considered.

For the zonal wind, there were differences between the models that did not align with differences in blocking. CM4 features an equatorward bias in the Pacific jet location ($\overline{U_{250}}$; Fig. 3.5) that is not found in AM4 (Fig. 3.5). The southwest-to-northeast tilt of the Atlantic jet is captured by AM4 and CM4, but the jet maximum is biased equatorward in both models. The Atlantic shifting is more extreme in CM4 than AM4 (Fig. 3.6a). CM4's equatorward shifted zonal flow is consistent with contracted Hadley circulation (Fig. 3.6b-c). This is also accompanied by generally colder SSTs in CM4 compared to AM4 (Fig. 3.7).

Despite large differences in the jet and SSTs between AM4 and CM4, the two models produce similar blocking climatologies (Fig. 3.8). Overall, the commonalities in blocking climatology biases in AM4 and CM4 suggest a weak sensitivity to the difference in zonal flow (Fig. 3.6) and ocean forcing (Fig. 3.7) between the models –or some compensating biases. At the same time, both models exhibit similar stationary wave and blocking climatology biases, and little transient eddy forcing biases (Figs. 3.11 and 3.12). This could suggest that the stationary wave could play the

more prevalent role in driving the biases in blocking. However further study is required to test this hypothesis.

Acknowledgements

This publication was supported through NOAA Educational Partnership Program/Minority-Serving Institutions award number NA16SEC4810008 to the Center for Earth System Sciences and Remote Sensing Technologies at The City College of New York. The authors thank The City College of New York, NOAA Center for Earth System Sciences and Remote Sensing Technologies, and NOAA Office of Education, Educational Partnership Program for fellowship support for Veeshan Narinesingh. Contents are solely the responsibility of the award recipient and may not represent official views of NOAA or the U.S. Department of Commerce. The authors thank Wenhao Dong and Spencer Clark for facilitating the process of obtaining the model data directly. We thank the reviewers and editor, whose feedback helped improve the manuscript.

Data Availability Statement.

ERA5 reanalysis data utilized for this work can be accessed from the European Center for Medium-Range Weather Forecasts (ECMWF; <https://www.ecmwf.int/en/forecasts/datasets/reanalysis-datasets/era5>). GFDL AM4 and CM4 data can be accessed from the World Climate Research Programme (WRCP) Coupled Model Intercomparison Project 6 (CMIP6; <https://esgf-node.llnl.gov/search/cmip6/>).

Chapter 4

Connections Between Atmospheric Blocking and Heat Extremes in Current and Possible Future Climates

Veeshan Narinesingh, James F. Booth, Yi Ming

Abstract

Atmospheric blocks are persistent high-pressure systems that can drive extreme heat events, leading to adverse impacts. The connections between blocking and heat extremes, however, is not fully understood. This work examines the climatology, dynamics, and connections between persistent extreme heat events and atmospheric blocking using reanalysis and GFDL's coupled atmosphere-ocean model, CM4. Throughout the Northern Hemisphere, strong regional variation in the association of blocking and heat events are found. In addition, blocked heat events over northeastern North America are found to be 1-2 K warmer and last a day longer, on average, than non-blocked events. In the historical integration of CM4, the model accurately simulates summer blocking over most of the hemisphere as well as the regional variation in heat extreme association. For the CM4 climate change projection using Representation Concentration Pathway 8.5, a reduction in blocking throughout the hemisphere is found, leading to less block and heat extreme association. In a comparison of northeastern North America heat extremes in the historical and climate change integrations, it is found that the 2 m temperature anomalies in the extreme heat events are 1-2 K weaker in the climate change projection in agreement with less blocking. However, this damping of the anomalies is largely outweighed by warming of the mean-state temperatures.

4.1. Introduction

Extreme heat events are known to have adverse, and even deadly effects on ecosystems and society (Garcia-Herrera et al. 2010; Wegren 2011; Shaposhnikov 2014). Yet despite the dangers they pose, many questions remain regarding the dynamical and thermodynamic aspects of these events, and how they will evolve in future climates (Perkins 2015; Horton et al. 2016). One dynamical phenomena of the atmosphere that is known to have some impact on heat extremes is atmospheric blocking (Trenberth and Fasullo 2012; Pfahl and Wernli 2012; Chan et al. 2019; Suarez-Gutierrez 2020). Atmospheric blocks are persistent, quasi-stationary anticyclones (Rex 1950; Lupo 2021). They occur over land and ocean and can influence the winds and temperatures over a large expanse. The association of blocking with heat extremes exhibits strong regional variability (Pfahl and Wernli 2012; Brunner 2018), with most studies focused primarily on Europe. Less attention has been given to the association and dynamics of blocking and heat extremes across the Northern Hemisphere and in future possible climates, and these elements will be the focus of the study herein.

The future of heat extremes is a question of great societal and ecological importance. On one hand, heat extremes are predicted to increase in future climates (Collins and Knutti 2013; Fischer and Knutti 2015). On the other hand, blocking is predicted to decrease (Woollings 2018; Davini and D'Andrea 2020). This could have implications for the overall behavior of extreme heat events. If, for example, less extreme heat events are driven by blocking, will the properties of heat extremes change?

As such, the work herein investigates the climatology, dynamics and association between persistent extreme heat events and atmospheric blocking. Following this introduction is section 4.2, the methods section. Then, in the results section (Section 4.3), we first investigate the co-

location of heat events and blocking across the Northern Hemisphere in reanalysis data (Section 4.3a). In Section 4.3b the dynamic and thermodynamic evolution of heat extremes in northeastern North America is compared for blocked and non-blocked events. After, having established the association and time evolution of heat extremes and blocking in reanalysis, we then analyze GFDL's coupled atmosphere-ocean model, CM4 (Section 4.3c). CM4 is part of the Coupled Model Intercomparison Project 6 (CMIP6). The model's simulation of blocking and its association with heat extremes is assessed. Finally, Section 4.3d looks at blocking and persistent extreme heat events in a climate projection using CM4 following representative concentration pathway 8.5 (RCP 8.5). For this, anomalous temperature and duration of persistent extreme heat events is compared between the climate change projection and historical integration. Section 4.4 contains a discussion of causality between blocking and persistent extreme heat events. Section 4.5 contains a summary and conclusions.

4.2. Methods

4.2a. Reanalysis and General Circulation Models

ERA5 reanalysis (Hersbach et al. 2020) is used to characterize the relationship between atmospheric blocking and persistent heat extremes. ERA5 is integrated using a horizontal resolution of approximately 30 km with 137 vertical levels. Model output is nudged by the assimilation of satellite and in situ observational data sets to achieve a close reconstruction of reality. The analysis herein utilizes daily mean data interpolated into 2.0 by 2.5 latitude by longitude grids. We focus on Northern Hemisphere summer defined as the months of June, July, and August for the years 1980-2014.

Following the analysis of blocking and heat extremes in reanalysis, we analyze these events in a comprehensive general circulation model. For this, the Geophysical Fluid Dynamics Laboratory's (GFDL) coupled atmosphere-ocean model, CM4 (Held et al. 2019), is used. CM4 is part of the Coupled Model Intercomparison Project 6 (CMIP6; Eyring et al. 2016). CM4 consists of the atmosphere model AM4 (Zhao et al. 2018) coupled to the ocean model OM4 (Adcroft et al. 2019). The atmosphere is integrated using roughly 100 km horizontal resolution on 33 vertical levels. Two separate climate simulations are analyzed, one historical and one climate projection.

The first climate simulation is a historical integration that includes time-evolving solar irradiance, aerosol precursor emissions, and green-house gas concentrations. These features provide realistic forcing conditions and follow CMIP specifications (documented here: <http://goo.gl/r8up31>). The model period spanning 1980-2014 is analyzed and referred to herein as the historical integration of CM4.

To investigate the effects of anthropogenic climate change on blocking and heat extremes, a representative concentration pathway 8.5 (RCP 8.5; Riahi et al. 2011) simulation of CM4 is analyzed. RCP 8.5 assumes a continued rise of greenhouse gas emissions throughout the 21st century and is sometimes referred to as the “business as usual” scenario (Riahi et al. 2011). RCP 8.5 leads to a radiative forcing of 8.5 W m⁻² by the year 2100. The analyses in this paper focus on the projection for years 2065-2099. As was done for the reanalysis, we use CM4 daily mean data interpolated onto 2.0 and 2.5 latitude by longitude grids.

4.2b. Block Tracking and Climatology

To identify and track summer blocking, the methodology described in Chan et al. (2019) is implemented. This metric is a modification of the 500 hPa geopotential height (Z_{500}) metric in Dunn-Sigouin and Son (2013). Both versions are hybrid metrics, meaning they search for

contiguous, positive, high amplitude Z_{500} anomalies that also reverse the meridional gradient of Z_{500} . The modification in Chan et al. (2019), however, is more apt for summer blocking, where both the anomaly amplitude and area thresholds are reduced compared to Dunn-Sigouin and Son (2013).

Details of the algorithm can be found in Chan et al. (2019) and Dunn-Sigouin and Son (2013), but here we summarize its implementation. First, Z_{500} anomalies are calculated by subtracting a running annual mean and mean seasonal cycle. Then, several criteria are imposed on contiguous positive Z_{500} anomalies:

1. Anomaly amplitude of 1.0 standard deviation or greater
2. Contiguous area of $1.0 \times 10^6 \text{ km}^2$ or greater
3. Reversal of the meridional gradient of Z_{500} as in Dunn-Sigouin and Son (2013)
4. To isolate quasi-stationary anomalies: area overlap of 50 % between successive daily timesteps for regions that satisfy elements 1-3.
5. Persistence criteria: meeting the above conditions for 5 days or longer

At each point in space and time, the tracking algorithm yields a block identification flag of 1 or 0 indicating the presence or absence of blocking. Throughout this paper, the blocking climatology, $P(B)$, is calculated by averaging block identification flag matrices for all summer timesteps (Fig. 4.1). $P(B)$ is the percent of summer days where blocking is present at a given grid-cell.

4.2c. Persistent Extreme Heat Events: Tracking and Block Association

The persistent heat event metric described in Chan et al. (2019) is used for the analyses herein. First, a 5-day running mean is applied to daily maximum 2 m temperature data, T , yielding the smoothed field \tilde{T} (Eq. 4.1). This is done to isolate persistent events. Then, a 29-day by 11-year

running mean, \hat{T} (Eq. 4.2), is subtracted to remove the seasonal cycle and long-term trend. Note, \hat{T} and \tilde{T} are functions of day, d , and can also be written as a function of the corresponding year, y . Subtracting \hat{T} from \tilde{T} yields the 2 m temperature anomaly field, T' (Eq. 4.3). At the data endpoints, all running averages use the data that is available when there are fewer elements than the window size.

$$\tilde{T}(d) = \frac{1}{5} \sum_{\delta=d-2}^{d+2} T(\delta) \quad (\text{Eq. 4.1})$$

$$\hat{T}(d) = \frac{1}{11} \sum_{v=y-5}^{y+5} \frac{1}{29} \sum_{\delta=d-14}^{d+14} \tilde{T}(\delta, v) \quad (\text{Eq. 4.2})$$

$$T'(d) = \tilde{T} - \hat{T} \quad (\text{Eq. 4.3})$$

For the analyses in this paper, 70th, 80th, 90th, and 99th percentile temperature anomalies are examined. For these events the conditional probability, $P(B|H)$, is calculated at each grid-cell. $P(B|H)$ is defined as the following: given a persistent heat event, the probability of blocking being co-located (Fig. 4.1).

Persistent heat events are separated into events that are associated with blocking and those that are not. First, the days of 90th percentile heat extremes in the grid-cell containing New York City are identified. Consecutive days are then grouped as distinct events. Then, at any point throughout each event, if 50 % of the boxed area between 38°-48° N and 73.5°-81.5° W contains blocking, the event is considered blocked. Here, a range of latitude and longitudes is used to leave room for any vertical misalignment between 2 m temperature and Z_{500} anomalies. In ERA5 101 distinct heat events were identified. Of this, 36 were blocked and 65 were not (Table 4.1). The results of this paper are insensitive to +/- 10 % of the boxed area threshold and +/- 5° in its boundaries.

4.2d. Significance Testing

A 95 % significance level is imposed for all significance testing throughout this paper. A Monte-Carlo method is used to determine the significance of differences between $P(B|H)$ and $P(B)$. To do this, we define n as the number of days over all summer days corresponding to a given percentile event (e.g., from 1980-2014 there are 3220 summer days, $n = 322$ constitutes the 90th percentile heat events). For our Monte-Carlo analysis, n days are randomly selected from all summer days. For this selection of days, grids of block identification flags are averaged to compute the blocking probability $P(B)$ at each grid point. This is then repeated $N = 1000$ times yielding distributions of $P(B)$ at each grid point. Right-sided z-tests are used to determine the significance of enhanced blocking probabilities in $P(B|H)$ relative to distributions in $P(B)$. This approach allows us to determine if there is a significant enhancement of blocking given a heat event relative to the probability of blocking for any given summer day

To test the significance of differences in duration and temperature anomalies for the heat extremes associated with blocking and those that are not, Mann-Whitney u-tests are implemented. The u-test is chosen because it does not assume the data fits to any specific parametric distribution. An example calculation is as follows. The temperature anomaly for the first day of all blocked heat events is gathered. Then, the same is done for all non-blocked events. U-tests are performed between the blocked and non-blocked data sets at each gridpoint.

We also compare the atmospheric jet and blocking climatology between ERA5 and CM4, as well as the CM4 historical and RCP 8.5 integrations. For a given model/integration, the mean zonal wind at 250 hPa is calculated for each summer. Then, to compare models/integrations, u-tests are performed at each gridpoint between the mean zonal winds computed for each summer. The same procedure is used to test for significance in summer blocking climatologies.

4.3. Results

4.3a The Association of Blocking and Heat Extremes in Reanalysis

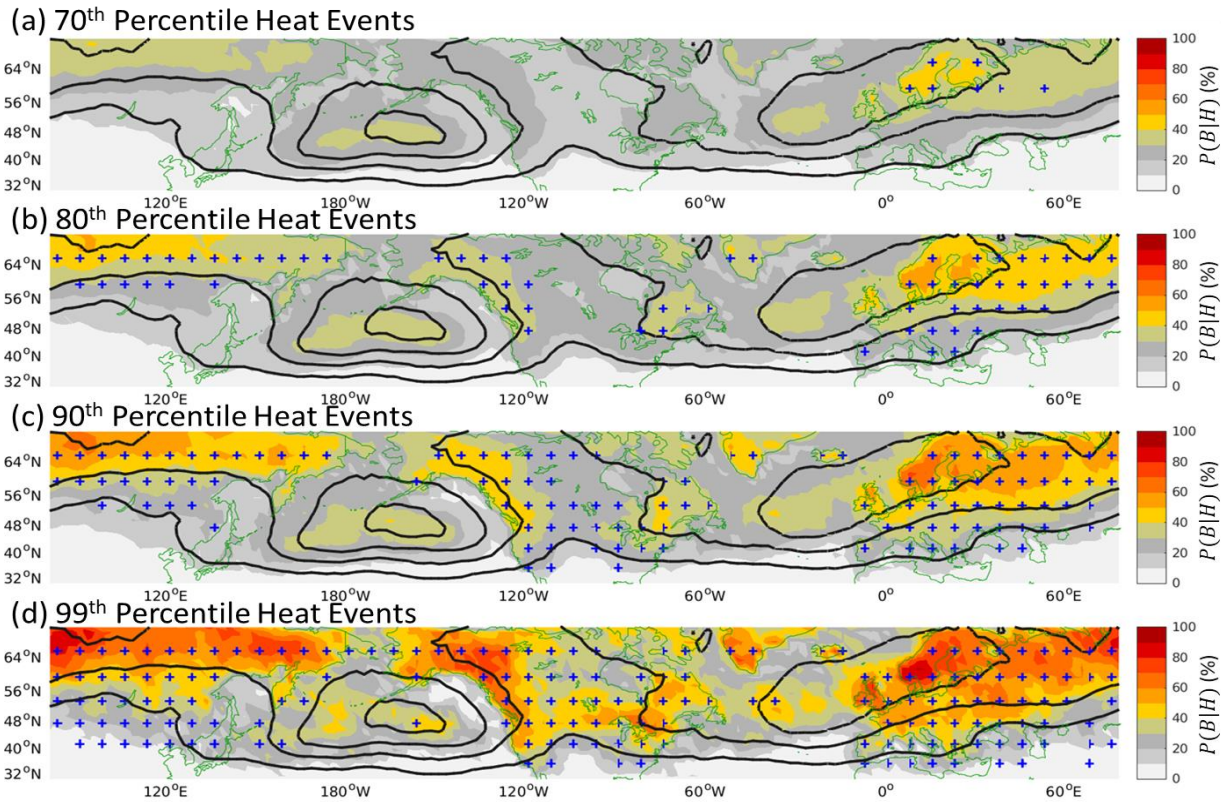


Figure 4.1. Percent of heat extreme days that include blocking (shading), $P(B|H)$, for (a) 70th, (b) 80th, (c) 90th, and (d) 99th percentile heat events. Contours indicate the percent of all summer days that are blocked, $P(B)$. The outer contour and contour interval is 5 %. Stippling indicates significant differences between $P(B|H)$ and $P(B)$.

Blocking occurs approximately 5-10 % of summer days over most of North America (Fig. 4.1).

During heat extremes, however, this frequency increases significantly. For example, 90th percentile heat extremes have blocks present 20-30 % of the time in central North America and 30-50 % of the time in the NE and NW parts of the continent. For 99th percentile events this increases to 30-50 % and 40-70 %, respectively.

Next, we focus on Eurasia, where summer blocking is occurs more frequently than in North America. In southern Eurasia blocking frequency ranges from 5-10 % of summer days, and in Northern Eurasia blocking occurs 10-20 % of the time. For 90th percentile heat events, blocking

frequency is 30-70 % throughout the continent. For 99th percentile events these values increase by about 10%. Thus, for both North America and Eurasia, as the severity of the heat extremes increases, so does the percentage of events associated with blocking (Fig. 4.1).

Also note, for the more extreme heat events (e.g., the 90th (Fig. 4.1c) and 99th (Fig. 4.1d) percentile events), there are more heat extreme events associated with blocking over land than there is over ocean. In North America, the number of heat extremes associated with blocks maximizes in the northwestern (NW) and northeastern (NE) parts of the continent. In Europe the coincidence between blocking and heat extremes is strongest over Scandinavia.

Figure 4.2 shows the reverse of the conditional analyzed in Figure 4.1: given the occurrence of blocking, what percentage of the timesteps are coincident with heat extremes. As in Figure 4.1, the co-location of heat extremes and blocking is more prevalent over land than ocean. For land, blocking leads to 70th percentile or greater heat extreme events 70-100% of the time. For increased heat extreme severity (i.e., 90th and 99th percentile events), the probability of having heat extremes given blocking decreases because there are less heat events.

Clearly there is a strong connection with summer heat extremes and blocking (Figs. 4.1-4.2). This, by itself, has been found in previous literature (Pfahl and Wernli 2012; Chan et al. 2019), however, our analysis showing how this changes for different strengths of the heat extremes is new. However, from Fig. 4.1, one sees that extremes can occur with and without the presence of blocking. This, then, begs the question: are there any differences between heat extremes driven by blocking and those that are not? We next explore this for northeastern North America.

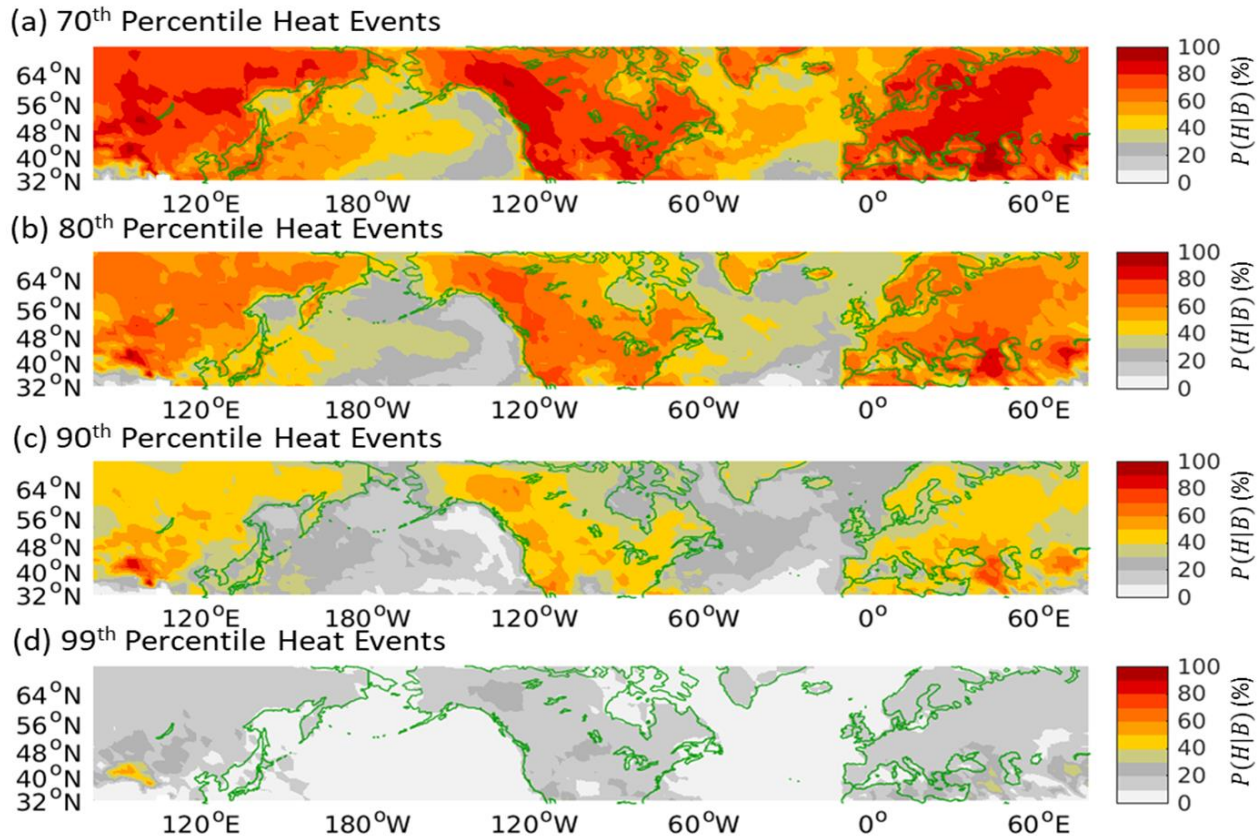


Figure 4.2. $P(H|B)$, the percent of blocked days that also include a (a) 70th, (b) 80th, (c) 90th, and (d) 99th percentile heat event.

4.3b Dynamical Comparison of Heat Extremes with and without Blocking

This analysis focuses on 90th percentile heat extremes in the reanalysis gridpoint containing New York City from 1980-2014. Although this analysis is specifically applied to New York City, one can see that these same events affect much of northeastern North America (Figs. 4.3-4.5). 90th percentile heat extremes account for 322 days out of the dataset, roughly 10 % of all summer days, by definition.

These heat extremes consist of 101 individual continuous events. This includes 65 non-blocked events and 36 blocked events (Table 4.1). The time evolution of anomalous 2 m temperature during these events can be seen in Figure 4.3 (note, the temperature anomalies are the

same ones calculated for identifying the heat extremes). 1 day before the start of heat events, the temperature of the region is enhanced by at least 2 K (Fig. 4.3a). The temperature anomaly is stronger for blocked events compared to non-blocked events, especially north of the Great Lakes region.

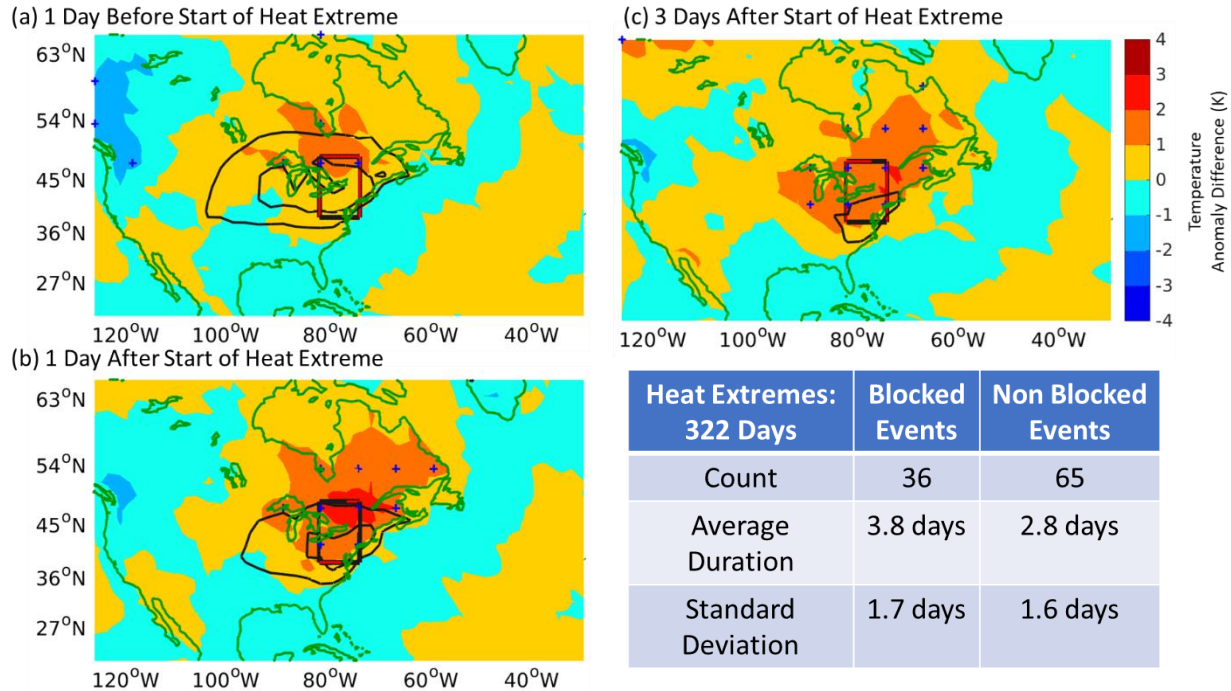


Figure 4.3. Temperature anomalies for non-blocked 90th percentile heat events in New York City (contours) and difference between blocked and non-blocked events (shading) composited (a) one day before event onset, (b) one day after event onset, and (c) 3 days after event onset. The outer contours and contour interval are 1 K.

Table 4.1. Duration statistics for blocked and non-blocked 90th percentile heat events in New York City. Difference in average duration between blocked and non-blocked events are found to be statistically significant by the parameters used within this paper.

Two days later, which is one day after the start of the heat extreme events, the warm anomaly weakens slightly during non-blocked events and strengthens for those that are blocked (Fig. 4.3b). For this, much of NE North America experiences an increase of 3-5 K for blocked events compared to 1-3 K for non-blocked events. Three days after event onset, the warm anomaly in the composite non-blocked case is nearly dissipated (Fig. 4.3c). For the blocked cases, however, a warming of 2-3 K persists in the region.

In terms of duration, blocked heat extreme events were found to last about 4 days on average, whereas non-blocked events were found to last for roughly 3 days (Table 4.1). This difference is statistically significant. Overall, blocked events tend to last longer and induce warmer temperature anomalies compared to non-blocked events. This likely is related to differences in the evolution of high-pressure anomalies within the region (Figs. 4.4-4.5).

Next, we examine the dynamical evolution of composited blocked and non-blocked extreme heat events (Fig. 4.4-4.5). Three days prior to the onset of blocked events, anomalous 2m temperatures (Fig. 4.4a) over the central U.S. are accompanied by an upper-level geopotential height anomaly within a planetary wave (Fig. 4.4b). The upper-level geopotential height anomaly is slightly downstream of the surface temperature anomaly. In terms of SLP (Fig. 4.4c), a closed high has already formed over the NYC region and a high SLP anomaly is also found downstream from the upper-level height anomaly.

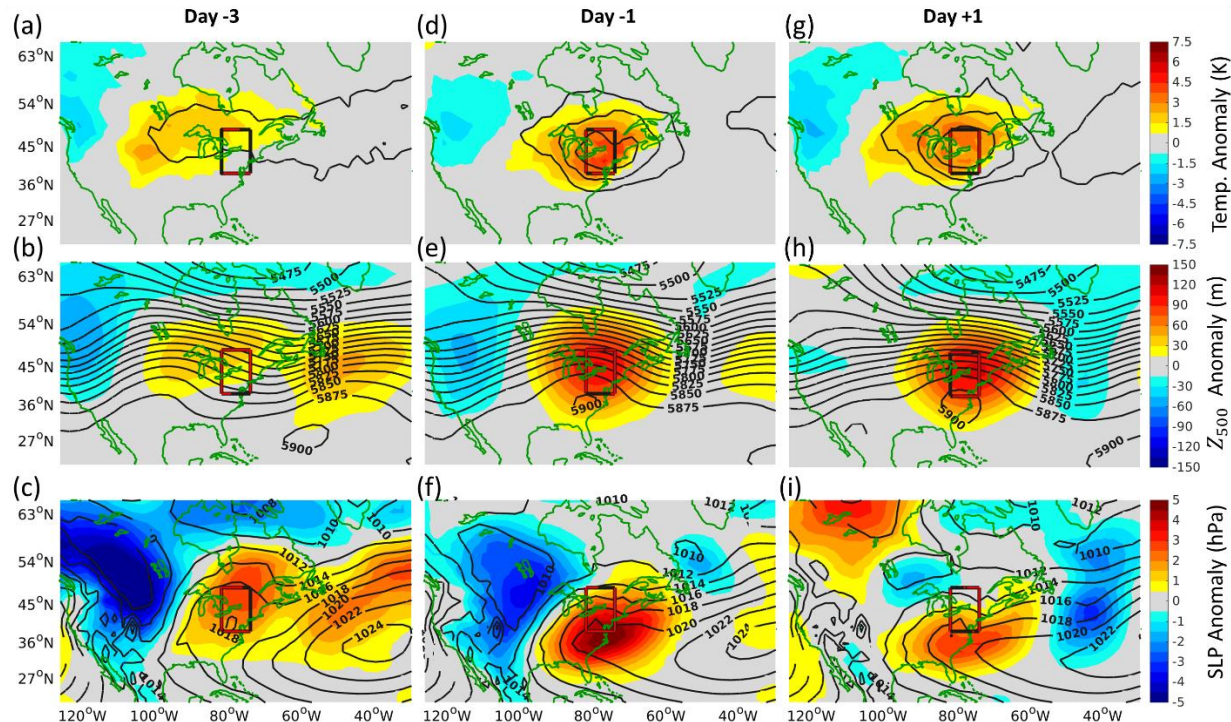


Figure 4.4. (a-c) Three days before the onset of blocked 90th percentile heat extremes in the grid-cell containing New York City, composited (a) 2 m temperature anomaly (shading) and blocking probability, $P(B)$ (contours), (b) Z_{500} (contours) and anomalous

Z_{500} (shading), and (c) SLP (contours) and anomalous SLP (shading). Panels (d-f) and (g-i) are as in (a-c) but instead composited one day before onset and one day after event onset, respectively. The outer contour and contour interval in (a), (d), and (g) is 20 %.

One day prior to event onset, the 2m temperature warms over NE North America (Fig. 4.4d). The upper-level height anomaly has amplified and propagated further downstream (Fig. 4.4e) where a block is established in the region 60-80 % of the time (Fig 4.4d). This is consistent with the strong ridge over the northeastern United States. The anomalies are now more barotropic in structure, where the 2 m temperature (Fig. 4.4d), upper-level height (Fig. 4.4e) and SLP anomalies (Fig. 4.4f) are vertically aligned. This structure remains in place and persists over the region (Figs. 4.4g-i).

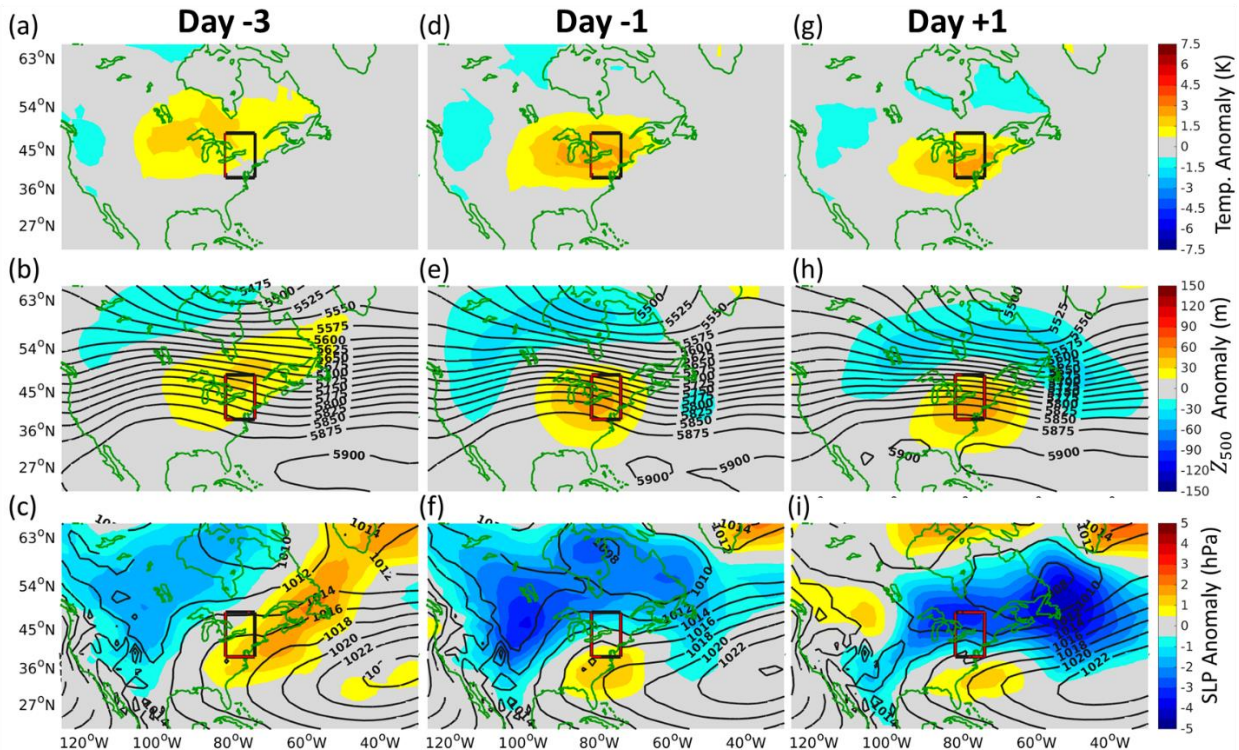


Figure 4.5. (a-c) Three days before the onset of non-blocked 90th percentile heat extremes in New York City, composited (a) 2 m temperature anomaly (shading), (b) Z_{500} (contours) and anomalous Z_{500} (shading), and (c) SLP (contours) and anomalous SLP (shading). Panels (d-f) and (g-i) are as in (a-c) but instead composited one day before onset and one day after event onset, respectively.

The composite for the non-blocked extreme heat events (Fig. 4.5) exhibits similar, yet considerably weaker anomalous patterns in 2 m temperature, upper-level height, and SLP compared to blocked events (Fig. 4.4). One major difference besides strength, however, is in the anomalous SLP field. Composited non-blocked events yield an SLP maxima that is farther south compared to blocked events. Anomalous low-pressure can also be found poleward of the region for the non-blocked events, whereas blocked events contain a more organized high-pressure anomaly.

One day after the onset of non-blocked heat extreme events, the temperature anomaly is weaker (Figs. 4.5g-i) compared to blocked events (Fig. 4.4g-i). This is consistent with the shorter average heat extreme duration for non-blocked events found earlier (Table 4.1).

Blocks can sustain warm temperatures through enhanced insolation associated with clear skies (Trigo et al. 2004), adiabatic warming via subsidence and horizontal advection (Nabizadeh et al. 2021), and through positive feedbacks involving soil-moisture (Fischer et al. 2007; Miralles et al. 2014). The relative contributions of these forcings, however, are found to vary by region (see review by Horton et al. 2016).

To better understand the thermodynamic drivers of extreme heat events in northeastern North America, the budget of temperature tendency is examined. The temperature tendency equation can be written as (Yanai et al. 1973; Yanai and Tomita 1998; Nabizadeh et al. 2021):

$$\frac{\partial T}{\partial t} = -\mathbf{u} \cdot \nabla T + \omega\sigma + Q \quad (\text{Eq. 4.4})$$

$$\frac{\partial T}{\partial t} = A + Q \quad (\text{Eq. 4.5})$$

Here \mathbf{u} is the horizontal wind $\mathbf{u} = (u, v)$ and ω is the vertical velocity in pressure coordinates, p . $\sigma = -\frac{T}{\theta} \frac{\partial \theta}{\partial p}$ is the static stability and θ is the potential temperature. The first and

second terms on the right-hand side of Eq. 4.4 represents horizontal and vertical thermal advection, respectively. The third term, Q , represents all other processes including diabatic energy exchange through phase changes, sensible heating, and long-wave radiation, as well as dissipation, diffusion, and numerical errors. In Eq. 4.5 we group the advection terms as $A = -\mathbf{u} \cdot \nabla T + \omega\sigma$ to express the temperature tendency as the sum of an adiabatic term plus Q .

For the temperature tendency analysis, we use 1000-hPa temperature instead of the 2-meter temperature. This is because focusing on a fixed pressure level removes any temperature changes forced by pressure changes. The 1000 hPa temperature and temperature tendency budget composited over blocked and non-blocked heat events in New York City is shown in Fig. 4.6. For blocked events, the peak in composite temperature is broader and warmer compared to composite non-blocked events. This is consistent with our earlier results which found blocked events to be warmer and longer. On average, blocked events also generate greater rates of warming, $\frac{\partial T}{\partial t}$, compared to non-blocked events.

Horizontal advection primarily has a cooling effect on local temperature throughout the composite lifecycles of blocked and non-blocked heat events (Figs. 4.6a and 4.6c). In the three days leading up to heat events, Q terms outweigh horizontal advection, resulting in a net heating effect. Around the onset of heat events through several days after, warm advection in the vertical direction helps to sustain the elevated temperatures. Note, heating from vertical advection is greater and more sustained for blocked (Fig. 4.6a) versus non-blocked (Fig. 4.6c) events, on average. During decay, Q terms and horizontal advection work together to rapidly cool the region.

From this analysis it can be seen that extreme heat events are not purely driven by advection. During the onset of these events Q terms tend to have a net heating effect on the

region, and during decay these terms result in a net cooling. This agrees with previous work which found heating related to soil-moisture, sensible heating, and long-wave radiation to be key in driving heat extremes (reviewed in Horton et al. 2016). Future work is planned to decompose Q into its diabatic and residual components to further understand the relative scales of various thermal contributions of these events.

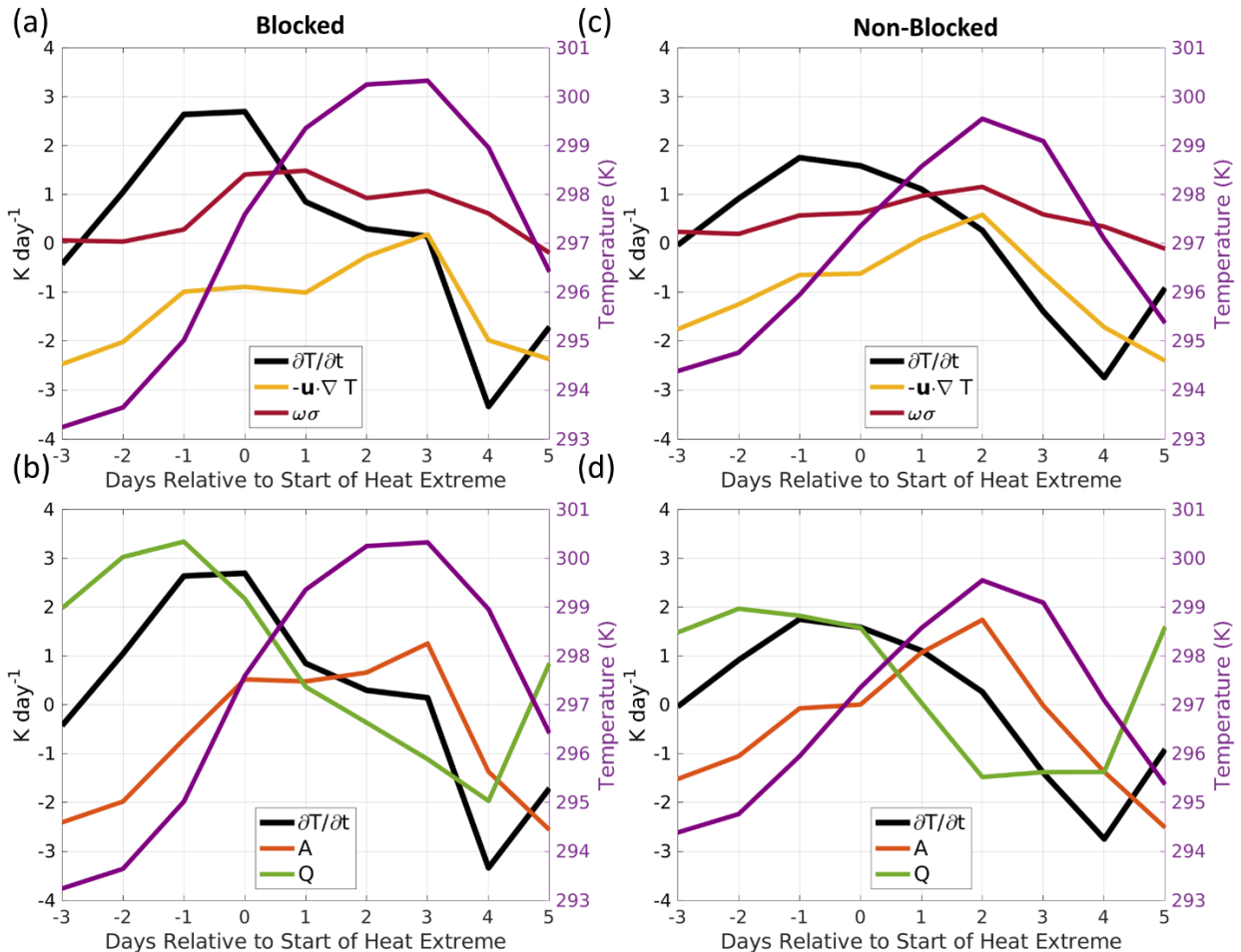


Figure 4.6. (a-b) For block associated heat events in the grid-cell containing New York City, composited 1000 hPa temperature budget terms: (a) Horizontal and vertical advection terms (b) Adiabatic advection terms, A , plus all other terms, Q . (c-d) As in (a-b) but for heat events not associated with blocking.

4.3c Blocking and Heat Extremes in CM4: Historical Simulation

Now that we have established the connection and dynamical evolution of blocking and persistent heat extremes in reanalysis, we next examine these events in the comprehensive GCM, CM4. We begin by noting the model's representation of the upper-level mean zonal flow (Fig. 4.7a-b) and blocking climatology (Figs. 4.7c-d) due to their connection with one another (Paradise et al. 2019; Barnes and Hartmann 2010).

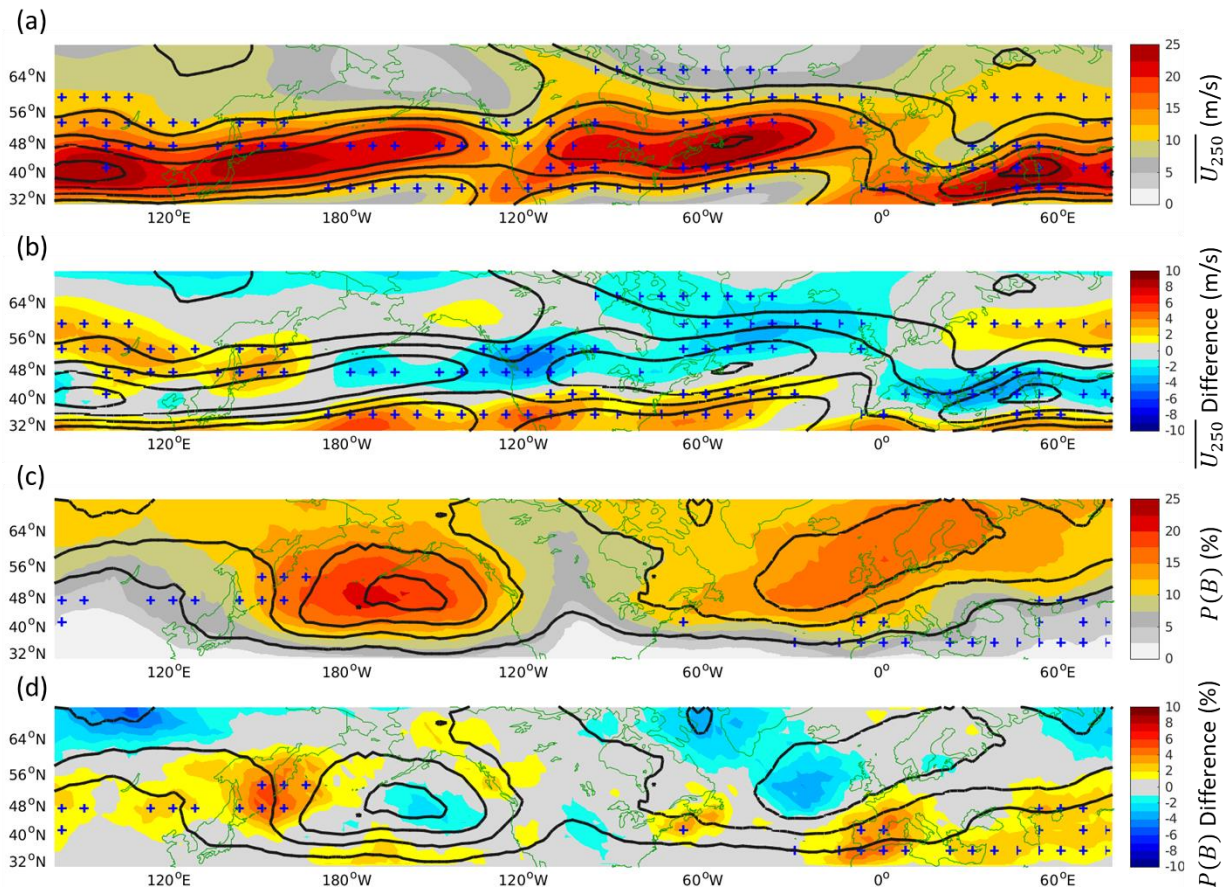


Figure 4.7. (a) Mean 250 hPa zonal wind, $\overline{U_{250}}$, for June, July, and August from 1980-2014 in ERA5 reanalysis (contours) and CM4 historical simulation (shading). (b) CM4 historical $\overline{U_{250}}$ subtracting ERA5 reanalysis (shading). $\overline{U_{250}}$ in ERA5 reanalysis (contours). (c) Percent of blocked June, July, and August days, $P(B)$, from 1980-2014 in ERA5 reanalysis (contours) and CM4 historical integration (shading). (d) CM4 historical $P(B)$ subtracting ERA5 reanalysis (shading). $P(B)$ in ERA5 reanalysis (contours). Outer contour and contour interval in (a-b) is 5 m/s. Outer contour and contour interval in (c-d) is 5 %.

The model captures the overall spatial structure of the jet (Fig. 4.7a). A tilted Atlantic jet maximum extends from North America eastward over the northern Atlantic Ocean, and starting in the Middle East, another jet maximum extends eastward through Asia and into the northern Pacific. CM4 also contains some biases in its mean circulation, however. As seen in Fig. 4.7b, the mean zonal flow is contracted equatorward in CM4 compared to ERA5. This is consistent with the findings of Narinesingh et al. (2022) and Held et al. (2019), the latter of which found contracted Hadley circulation in CM4. Held et al. (2019) speculated that this contracted circulation was more so a result of a warmer tropical upper troposphere than by sea surface temperature biases.

Despite the jet biases, the model contains much less bias in the blocking climatology (Fig. 4.7c). No significant blocking biases over North America and Northern Eurasia are apparent. This is an improvement over wintertime in these regions for this model (Narinesingh et al. 2022). However, near southern Europe and extending eastward into the western Pacific there is an overgeneration of blocking. This area of blocking biases compared to other regions could suggest mechanistic differences in blocking from region to region. For example, the weakened jet in southern Eurasia (Fig. 4.7b) is consistent with an enhancement of blocking (Fig. 4.7d) as in the idealized modelling work of Paradise et al. (2019), but the same behavior is not found over North America and the North Atlantic.

Next, we assess CM4's association of heat extremes and blocking events. Fig. 4.8 shows the percentage of extreme heat events that coincide with blocking in ERA5 (Fig. 4.8a-c) and CM4 (Fig. 4.8d-f). The model demonstrates similar event association compared to reanalysis. It also captures the properties that: (1) as the severity of heat threshold is raised, more heat events coincide with blocking, and (2), more events heat events over land are associated with blocking as compared to over the ocean.

The regional variation in heat extreme and blocking association is also captured by CM4 (Fig. 4.8). For example, the northeastern and northwestern coasts of North America have greater association of heat extremes and blocking compared to central parts of the continent. In addition, CM4 also simulates that heat extremes over Scandinavia are most co-located with blocking compared to the rest of Eurasia.

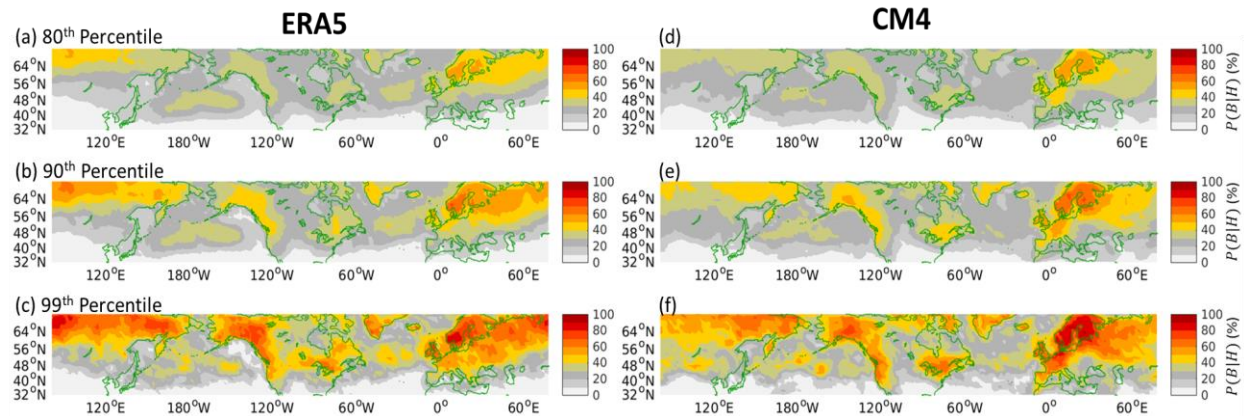


Figure 4.8. (a-c) In ERA5 reanalysis, percent of heat extreme days that include blocking (shading), $P(B|H)$, for (a) 80th, (b) 90th, (c) and 99th percentile heat events. (d-f) As in (a-c) but for CM4 historical integration.

Overall, CM4 reliably reproduces the frequency of blocking over North America and northern Eurasia but deviates for southern Eurasia. Nonetheless, CM4 produces a similar association of heat extremes with atmospheric blocking compared to reanalysis throughout the hemisphere. We next shift to the model's simulation of blocking and heat extremes in the climate change scenario now that its behavior in the historical integration has been established.

4.3d Blocking and Heat Extremes in CM4: Climate Change Projection, RCP 8.5

By the end of the 21st century, RCP 8.5 exhibits weaker upper-level mean zonal flow and a reduction in blocking compared to the historical integration (Fig. 4.9a-c). This is inconsistent with the findings of Paradise et al. (2019) who found more blocking for weaker zonal background

flows, but it is consistent with the differences between summer and winter in the present climate. This could point to other factors such as transient eddy forcing or stationary wave changes leading to the reduction in blocking, but here we do not attribute causality.

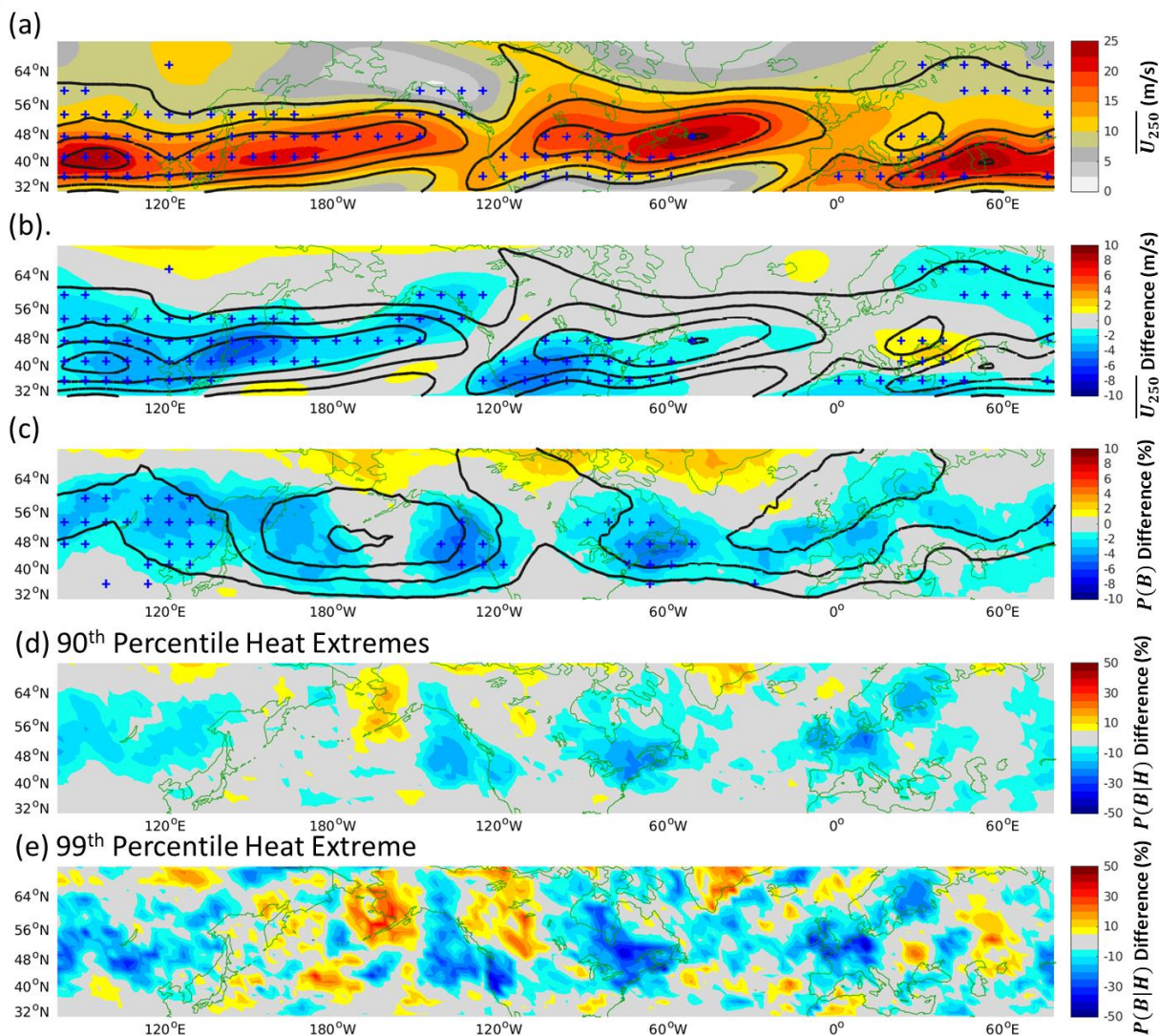


Figure 4.9. (a) Mean 250 hPa zonal wind, $\overline{U_{250}}$, for all June, July, and August in CM4 historical integration (contours) and CM4 RCP 8.5 simulation (shading). (b) CM4 RCP 8.5 $\overline{U_{250}}$ subtracting CM4 historical (shading). $\overline{U_{250}}$ in CM4 historical (contours). (c) Difference in $P(B)$ for CM4 RCP 8.5 subtracting CM4 historical (shading). $P(B)$ in CM4 historical (contours). (d-e) Difference in

$P(B|H)$, CM4 RCP 8.5 subtracting CM4 historical (shading) for (d) 90th, and (e) 99th percentile heat events. Outer contour and contour interval in (a-b) is 5 m/s. Outer contour and contour interval in (c) is 5 %.

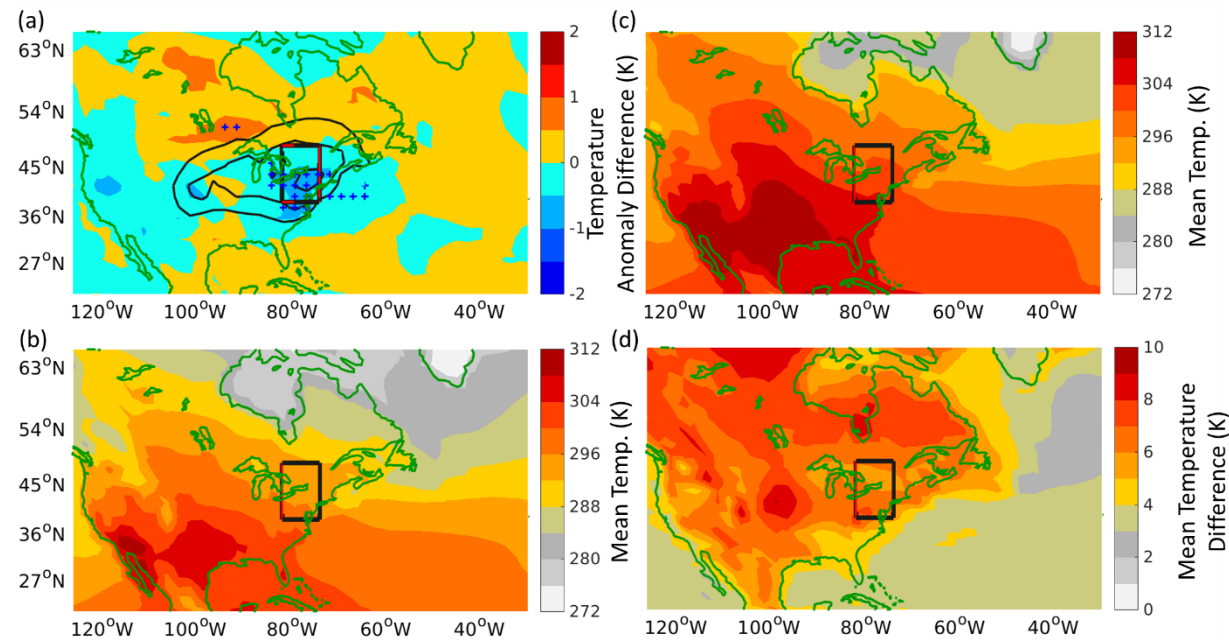


Figure 4.10. (a) Composite 2 m temperature anomaly for one day after the onset of all 90th percentile New York City heat events in CM4's historical integration (contours). The outer contour and contour interval is 1 K. Difference in 2 m temperature anomaly composite one day before all 90th percentile New York City heat events, CM4 RCP 8.5 subtracting CM4 historical integration (shading). Blue stippling indicates significant differences. (b-c) Mean 2 m temperature for June, July August in (b) CM4 historical integration from 1980-2014, and (c) CM4 RCP 8.5 integration from years 2065-2099. (d) Difference between (c) and (b), CM4 RCP 8.5 subtracting CM4 historical integration.

On a regional basis, significant decreases in blocking occur near the northwestern and northeastern coasts of the United States as well as in East Asia (Fig. 4.9c). Decreases in blocking were found to be robust to the exclusion of the gradient reversal criteria as well as increases in anomaly and area thresholds used in the blocking detection metric. Also in RCP 8.5, less extreme heat events are associated with blocking (Fig. 4.9d-e), consistent with the reduction in blocking.

The decrease in frequency of block-heat extreme association exhibits a similar spatial pattern to the reduction found in the blocking climatology (Fig. 4.9c). The biggest change in block-

heat extreme association is found for 99th percentile events (Fig. 4.9f), where in some regions there is nearly a 50 % reduction in event association.

Earlier, block associated heat extremes were found to be warmer and longer in duration than those without blocks. Next, we examine how the temperature and duration of heat extremes change in the warmer climate, given the reduction in blocking. A temperature comparison of all 90th percentile New York City (NYC) heat events is shown in Fig. 4.10a along with event duration statistics in Table 4.2.

	Historical Integration		RCP 8.5 Integration	
	Blocked Events	Non-Blocked Events	Blocked Events	Non-Blocked Events
Count	41	63	33	64
Average Duration (days)	4.0	2.5	3.7	3.1
Standard Deviation (days)	1.8	1.4	2.1	1.9
All Events: Average Duration (Standard Deviation)	3.1 Days (1.7 Days)		3.3 Days (2.0 Days)	

Table 4.2. Average and standard deviation for blocked and non-blocked 90th percentile heat events in the New York City grid cell of the CM4 historical and RCP 8.5 integrations.

In the northeastern United States, the composited temperature anomaly for heat events in RCP 8.5 is up to a degree cooler compared to the historical integration (Fig. 4.10a). This agrees with the association of 20 % less blocking events in RCP 8.5 (Table 4.2) and weaker Z_{500} anomalies for both blocked and non-blocked events (not shown). The decrease in anomalous temperature, however, is strongly offset by changes in the mean temperature (Figs. 4.10b-d). Across North America as well as the rest of the hemisphere, the mean temperature increases everywhere (Figs. 4.10b-d). This heating is spatially non-uniform, with certain regions, such as the central U.S., experiencing more warming than others (Fig. 4.10d). In the northeastern U.S., the mean temperature increases by 6-7 K. RCP 8.5 also exhibits a decrease in meridional temperature gradient over the U.S., consistent with the weaker jet discussed earlier (Fig. 4.9b).

In terms of average duration, heat extremes in the warmer climate are similar to those in the historical simulation (Table 4.2). This is despite the decreased association of heat extremes with blocking in RCP 8.5.

To summarize, an overall decrease in blocking is found for the RCP 8.5 scenario. This leads to a 20 % decrease in atmospheric blocks driving 90th percentile heat events. In agreement with decreased block association, heat events in RCP 8.5 have cooler composited temperature anomalies. Note however, mean temperature increases for the northeastern United States outweighs decreases in anomalous temperature by 6-7 K. In addition, the average duration over all heat events remains essentially the same across both climate integrations, despite less blocking in RCP 8.5.

4.4. Causality Between Blocking and Persistent Extreme Heat Events

Here we discuss causality: Are the blocks generating the persistent extreme heat events, or is it the other way around?

From an atmospheric perspective, heat events are driven by several factors: (1) vertical and horizontal advection of warm air, (2) adiabatic warming through the compression of sinking air, and (3) clear skies which optimize solar insolation and thus diabatic heating from the surface (e.g., Horton et al. 2016). All of these factors are consistent with blocking, where large columns of high-pressure are associated with subsidence (Colucci 1985; Lupo and Bosart 1999; Nabizadeh et al. 2021) and thus clear-sky conditions (Trigo 2004). With this in mind, we revisit our analysis of blocked heat events in northeastern North America (Figs. 4-5).

Three days before the onset of blocked heat events, an upper-level anticyclonic anomaly travels across North America (Fig. 4.4b). Near the surface, warm temperatures lie directly below

and slightly upstream of the anticyclone (4-4a) and a high-pressure anomaly is located slightly downstream, over the northeast. The temperature tendency equation during this time shows warming primarily driven by Q (i.e., diabatic and non-conservative sources; Fig. 4.5b). This could suggest that diabatic effects associated with the surface high begins to warm the region prior to the arrival/formation of the block.

The upper-level anticyclone then travels further downstream, amplifies, and stalls one day before event onset (Fig. 4.4e). A block is present 60-80 % of the time (Fig. 4.4d), consistent with vertical motion now working with Q to accelerate warming in the region (Fig. 4.5a-b). Vertical motion continues to help sustain warm temperatures throughout the rest of the composite lifecycle as the block persists.

Our results show warming begins in the region prior to blocking (Figs. 4.4a-c and 5a-b). Upon the arrival/formation of blocking, however, warming accelerates and heat events initiate 1-2 days later. This is consistent with Neal et al. 2021, which found that block formation preceded the formation of a heat dome. Taken together, these results suggest that blocking is indeed causal of persistent extreme heat events but heating at the surface prior to block formation may too be essential.

Positive feedback at the surface has also been proposed to play a role in driving heat events. For example, suppressed latent cooling from desiccated soils acts to drive warmer temperatures (Fischer et al. 2007; Miralles et al. 2014). Thus, though this paper suggests that atmospheric blocking is the key ingredient driving persistent extreme heat events, further study is required to rule out other factors.

4.5. Summary and Conclusions

This paper investigates the climatology, dynamics, and connections between persistent heat events and atmospheric blocking in reanalysis and the GFDL climate model. Over land, we confirm that atmospheric blocking is often co-located with persistent surface heat events (Fig. 4.1). This relationship is strongest over northeastern and northwestern North America and northern Eurasia. There, 99th percentile heat events are co-located with blocking over 50 % of the time. In addition, we find that blocking leads to 70th percentile heat events over 80 % of the time (Fig. 4.2). The exceptions to this are over central North America and East Asia, where the link between blocking and heat extremes is not strong.

We also compare temperature, duration, and the dynamics of blocked and non-blocked persistent heat events in the northeastern United States. On average, blocked events are 1-2 K warmer (Fig. 4.3) and last one day longer (Table 4.1). The dynamics of composited blocked events (Fig. 4.4) are as follows:

- Three days before onset (Fig. 4.4a-c) - Wave train pattern in composite 500 hPa geopotential height over North America. An upper-level anticyclone over central North America is accompanied by a warm 2 m temperature anomaly slightly upstream and an anomalous SLP maxima slightly downstream.
- One day before onset (Fig. 4.4d-f) - The composite anticyclone has propagated downstream to northeastern North America and amplified. The warm 2 m temperature anomaly, upper-level height anomaly, and high-pressure SLP anomaly are now vertically aligned. Blocking is now formed over the region 60-80 % of the time.

- One day after event onset (Fig. 4.4g-i) - Structure from one day before onset remains in place. The upper-level anticyclone strengthens and high-pressure SLP anomaly weakens.

Composited non-blocked persistent heat events (Fig. 4.5) exhibit a weaker but similar evolution of 2 m temperature and anomalous upper-level geopotential height compared to blocked events (Fig. 4.4). Regarding SLP, however, non-blocked events have a high-pressure maximum that is further south and flanked poleward by low-pressure.

An analysis of the temperature tendency equation at 1000 hPa confirms that blocked heat events are indeed warmer and longer in duration, on average (Fig. 4.6). Nonetheless, the various terms in the temperature tendency equation have a similar time evolution for non-blocked versus blocked events; the terms in the non-blocked case are just weaker.

We write the temperature tendency as the sum of horizontal and vertical advection, A , plus diabatic and non-conservative effects, Q (Eq. 4.5). In the days leading into extreme heat events, Q dominates as the source of warming. Then, during event onset and for several days after, vertical motion acts to sustain warmer temperatures as horizontal advection and Q have cooling effects.

After examining atmospheric blocking and persistent heat events in reanalysis, we then shifted to the comprehensive general circulation model, CM4. We first assessed the model's fidelity in reproducing blocking, heat events, and the relationship between the two in a historical integration. We then examined how blocking and heat events might change in a climate change projection.

CM4 historical does well in capturing the blocking climatology over northern Eurasia and North America but generates too much blocking over southern Europe eastward over Asia (Fig. 4.7). This is accompanied by an equatorward shift in mean zonal circulation throughout the

hemisphere (Fig. 4.7a-b). Taken together, these results suggest that the blocking climatology over northern Eurasia and North America is not strongly affected by the equatorward jet bias. Overall, there is regional dependence regarding biases in the blocking climatology over land –some regions do rather well while others are biased high.

The association of blocking with persistent extreme heat events is also captured by CM4 (Fig. 4.8). Just as in reanalysis, as the amplitude of heat events increases so does the association with blocking. In addition, the model captures regional differences in the association of blocking and heat events. Over Scandinavia as well as northeastern and northwestern North America, for example, the association of events is strongest.

In the climate change projection of CM4 (RCP 8.5) there is decreased blocking and mean zonal circulation throughout the hemisphere (Fig. 4.9). Consistent with the decrease in blocking, less persistent heat events are associated with blocking. This prompted further examination of differences between heat events in the historical integration versus the climate change projection.

In northeastern North America, 20 % less persistent heat events are associated with blocking (Table 4.2). Consistent with this, persistent heat events in the climate change projection have 2 m temperature anomalies that are 1-2 K weaker, on average (Fig. 4.10a). This weakening, however, is outweighed by changes in the mean state (Fig. 4.10b-d), which increases by 6-7 K.

In terms of duration, persistent heat events in the climate change projection are similar to those in the historical, inconsistent with the decreased association of blocking. There is suggestion of an increased duration of non-blocked events in the climate change projection (Table 4.2), which could compensate for less blocking, though this result is not significant. Altogether, persistent heat events in the climate change projection are similar in duration, but warmer than the historical integration mostly due to mean state changes.

Chapter 5

Conclusion and Discussion:

This thesis investigated the dynamical and climatological aspects of atmospheric blocking. What follows is a summary of each research component along with plans for future work.

5.1 Research Component 1: Atmospheric Blocking in an Aquaplanet and the Impact of Orography

Research Component 1 tackles fundamental questions about blocking through idealized modeling experiments. Two main research themes emerge within this paper. The first, assessing the idealized model's fidelity in simulating the climatology and dynamics of blocking, and the second, understanding the roles of orography and mean circulation features in generating the observed spatial distribution in blocking.

For this, an idealized moist general circulation model is configured as an aquaplanet and in separate integrations, various orographic configurations are introduced. For these experiments, single mountains of varying height are added to the aquaplanet, and then two mountains are added.

The model reproduces the climatology of blocking with physical consistency. In the aquaplanet, blocking mostly occurs in a zonally symmetric latitude band between 40-60°. Upon adding mountains, blocking then becomes anchored primarily on the upstream side of mountains near the high-pressure anomaly in the stationary wave. This mirrors what is seen in reality near the Rocky Mountains.

The dynamical processes of blocking life cycles are also captured by the model, and this is true regardless of the presence of orography. Block-centered compositing of geopotential height and 8-to-30-day wave activity fluxes shows that the model demonstrates a realistic dynamical evolution of blocking (Fig. 2.3):

1. Blocking onset: large-scale Rossby wave-like features in the region with wave activity fluxes converging on the down-stream equatorward flank
2. Strongest phase: wave activity flux convergence maximizes
3. Decay: an absence of wave activity flux entering the blocked region and a net divergence of wave activity flux out of the block into downstream regions of low-
This affirms the model's utility with regards to understanding the physics of blocking in reality.

The orographic integrations elucidate the importance of stationary forcing in anchoring and generating blocking (Fig. 2.6). Enhanced amounts of blocking were found near high-pressure stationary wave anomalies and at storm track exit regions, while blocking was suppressed near the stationary wave low and zonal wind maxima on the lee of mountains. For mountains of 2 km and greater, significantly more blocking was generated in the model compared to the aquaplanet integration.

These results are consistent with reality, where the Northern Hemisphere contains more orographic forcing and more blocking compared to the Southern Hemisphere. This work also emphasizes the importance of the stationary wave to blocking. Although we found in the aquaplanet that stationary waves are not necessary to generate blocking, we also found that strong stationary waves lead to enhanced amounts of blocking. Generally, this work provides insight into why blocks occur where they do.

Overall, this work required an understanding of the idealized moist GCM and how to configure it to perform experiments. The addition of orography required the development of land-masks that were then imposed as model boundary conditions. Model stability was affected by the height of orographic forcing. To achieve stability, the 4-km single mountain run required a model timestep of 600 seconds. This timestep was then used for all other model integrations to ensure experimentally consistent results. Though not explored here, I also learned how to vary other aspects of the model such as solar insolation, seasonal cycle, and greenhouse gas concentrations.

Based on the results of how orography influences the spatial distribution of blocking, another research idea came to mind. What is the dependence of the blocking on the magnitude, orientation, and latitude of stationary waves and storm tracks? Fig 5.1 shows a schematic of where blocking is most ubiquitous in relevance to this question.

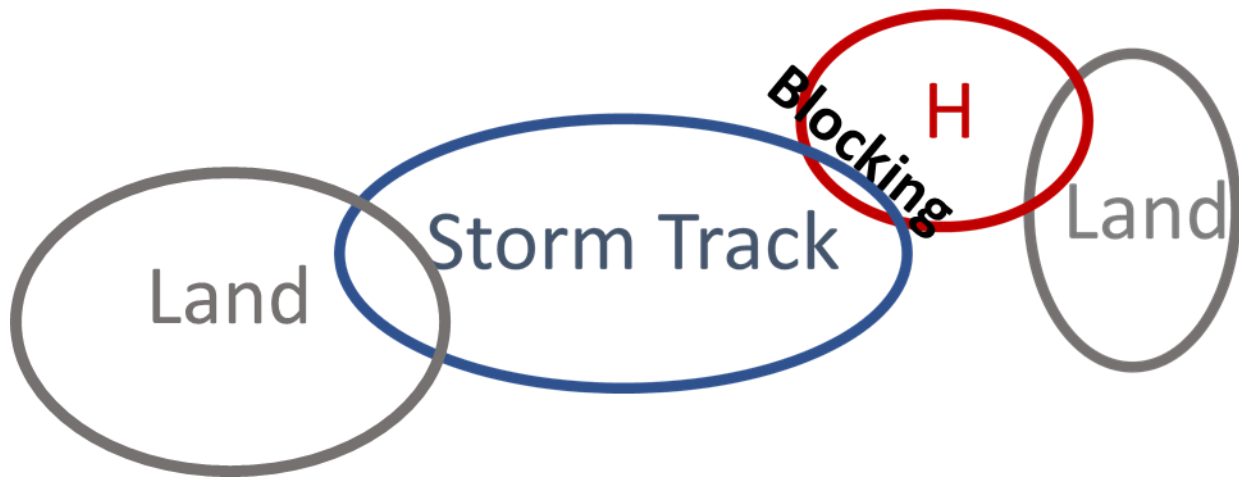


Figure 5.1. A schematic of where blocking is most ubiquitous. H represents the high-pressure anomaly of the stationary wave. In reality blocking occurs near the high-pressure stationary wave anomaly and end of the storm track.

Previous work (Tung and Lindzen 1979) has suggested that blocking is the product of the resonant amplification of stationary waves and boundary forcing. In this work, we showed that stronger stationary waves in idealized models led to a non-linear increase in blocking. This is consistent with Tung and Lindzen (1979); In our result, as mountain height was increased, the

stationary wave increased in amplitude and upstream zonal flow decreased, resulting in more blocking.

As previously mentioned, transient eddies also play an important role in blocking (Shutts 1983).

The orientation of these eddies is also key (Wang and Kuang 2019), and the frequency of blocking is dependent on storm track location and amplitude. In future work, it would be interesting to use the idealized model to manipulate the amplitude and location of the storm track and stationary wave relative to one another, noting the response of blocking. This might provide insight into how blocking could evolve in future climates as these atmospheric mean state features are altered.

5.2 Research Component 2: Blocking and General Circulation in GFDL Comprehensive Climate Models

Stepping up in the model hierarchy, Research Component 2 focuses on blocking in comprehensive general circulation models: one atmosphere only and one coupled atmosphere-ocean. Climate models like these are important tools for understanding and predicting how the earth's climate will change in the future. However, to guide our interpretation of model results in future climates, it is important to first assess any model biases in current climates.

In this paper, we assess model biases in the climatology and dynamics of blocking, and possible connections to biases in mean circulation. This is done for historical integrations of the GFDL atmosphere-only model AM4 and coupled atmosphere-ocean model CM4. For the historical integration of AM4, forcing is provided by time-evolving SST and sea ice distributions observed from 1980-2014. For CM4's historical integration, AM4 is instead forced by a dynamic ocean model (OM4) over the same time period.

We first focus on mean circulation biases, specifically the stationary wave defined using the 500 hPa geopotential height field, and the mean zonal wind at 250 hPa. The models exhibit similar stationary wave biases in regions where blocking is most ubiquitous. Near the Pacific maxima, the anticyclonic stationary wave is biased high compared to reanalysis; In the Atlantic, the stationary wave is too weak.

Both model integrations capture the Pacific and Atlantic jet maxima, however CM4 contains much more bias than AM4 when compared to reanalysis data. The biggest difference between the models is that CM4 has equatorward shifted, contracted zonal circulation (Fig. 3.6). This extends both vertically and zonally throughout the midlatitude troposphere.

Despite very different ocean forcing and jet biases between AM4 and CM4, however, the models exhibit similar blocking climatology biases: too much blocking in the Pacific and too little in the Atlantic (Fig. 3.8). In terms of blocking dynamics, the models reproduce realistic geopotential height and transient eddy forcing compared to reanalysis.

Paradise et al. (2019) used an idealized traffic jam model to find direct relationships between blocking and stationary wave amplitude as well as eddy forcing. In terms of the jet, Paradise et al. (2019) also found an indirect relationship with blocking.

Taken together, these results suggest that stationary wave biases could be the main driver of atmospheric blocking biases found within these models. In AM4 and CM4 the enhanced (suppressed) Pacific (Atlantic) blocking is consistent with a stronger (weaker) stationary wave. The jet response, however, is less straightforward. In the Atlantic for example, where the jet is biased low, so is the blocking.

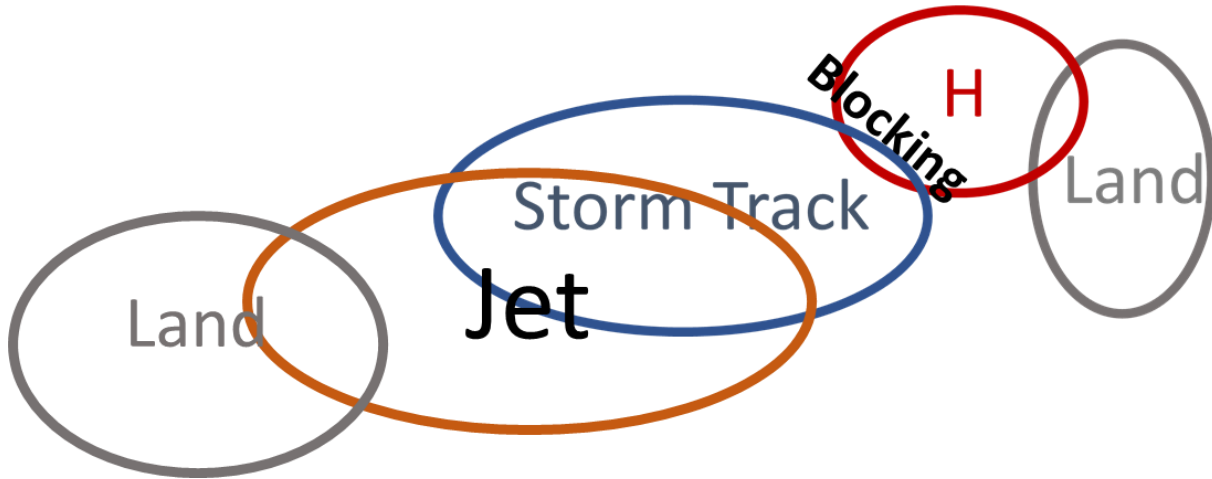


Figure 5.2. Modified version of Fig. 5.1 to explicitly include the jet. This schematic depicts an idealization of where blocking is most ubiquitous relative to the jet, storm track, and high-pressure stationary wave anomaly (H).

Future work is planned to test our theory on the dominance of stationary wave biases driving blocking biases by modulating the stationary wave and jet to test the effects on blocking. Such work would be an extension of the idealized modelling work proposed with the schematic in Fig. 5.1, where now we are explicitly considering the jet (Fig. 5.2). Note, any investigation would need to consider the interplay between mean circulation features, and how changing one could affect others.

5.3 Research Component 3: Connections Between Atmospheric Blocking and Heat Extremes in Current and Possible Future Climates

Atmospheric blocks are known drivers of persistent heat extremes and understanding this relationship can aid us in aptly preparing for these events. As such, this work investigates atmospheric blocking and persistent extreme heat events in reanalysis followed by a historical integration and climate change projection of the coupled atmosphere-ocean model, CM4.

We begin by analyzing regional variation in the association of blocking and heat extremes in reanalysis. We then compare blocked and non-blocked heat events in northeastern North America in terms of temperature, duration, dynamics, and near-surface temperature budget. Next, we assess CM4's simulation of blocking and block-heat extreme association. We also compare heat extremes in historical integration and climate change projection.

Over North America, the connection between blocking and heat extremes maximizes over the northeastern and northwestern parts of the continent, minimizing in the center (Fig. 4.1). Over Eurasia, blocking and heat waves are most co-located over Scandinavia and northern Eurasia, and least associated near southern regions. Generally over land, as intensity of heat extreme is increased so does the probability to be co-located with blocking.

On average, heat extremes over northeastern North America were found to be warmer and longer in duration for blocked events as opposed to non-blocked events. In terms of dynamical evolution (Fig. 4.4), composited blocked heat events feature a planetary wavelike structure over the United States three days before onset. The ridge portion then amplifies and propagates eastward, stalling over the northeast region. A barotropic structure persists where the upper-level geopotential height anomaly is vertically aligned with sea-level pressure and surface temperature. For non-blocked events, the evolution of upper-level flow is similar but much weaker. At

For non-blocked events, a similar but weaker upper-level height evolution is present. At the surface, however, the composited pressure patterns for blocked and non-blocked events differ. For blocked events, surface pressure is more organized with a high directly over the region. For non-blocked events, the surface pressure maximum is further south and flanked poleward by low-pressure. In addition, anomalies for non-blocked events dissipate more quickly.

The 1000 hPa temperature budget is analyzed and compared for blocked and non-blocked events. The analysis confirms blocked events are warmer and longer in duration than non-blocked events. The thermodynamic evolution, however, is similar for both cases; non-blocked events just have weaker terms. Diabatic and non-conservative effects are found to drive temperature increases in the three days leading into the onset of heat events. Then, throughout the lifecycle of heat events, adiabatic subsidence helps to sustain warm temperatures.

Next, we examined blocking and heat events in CM4. Throughout most of the Northern Hemisphere, CM4 accurately reproduces the climatology of blocking in the historical simulation. The exception to this is near southern Europe and Northern Africa extending eastward over Asia, where too much blocking is produced. CM4 also accurately simulates the association of blocking with heat extremes, exhibiting similar association probabilities and regional variation compared to reanalysis.

In the climate change projection of CM4, blocking is less ubiquitous. This leads to a decreased association of blocking with extreme heat events. Consistent with less blocking, heat events in northeastern North America exhibit composited 2 m temperatures anomalies of 1-2 K less in the climate change projection compared to the historical integration. This, however, is outweighed by a 6-7 K increase in mean temperature.

Overall, this work provides insight into regional variation in the association of atmospheric blocking and heat extremes, and the dynamics of these events. We also investigate how these events could evolve in a future possible climate. Although this paper answers several questions, it also raises several more. Future work is planned to further investigate the diabatic contributions to the temperature tendency budget during heat extremes. In particular, I would like to explicitly calculate contributions from outgoing long-wave radiation as well as sensible heat fluxes. This

will then be extended to other regions to get a sense of whether the thermodynamic drivers of heat extremes differ from region to region.

Further work is also needed regarding the dynamics of heat events. For example, in block-associated heat extremes, what causes the anticyclone to propagate eastward and then stall over the region? Also, in conjunction with the diabatic heating analysis, does the near surface temperature anomaly act to reinforce blocked structures? These are both future possible research questions.

Research Component	Key Takeaways
1. Atmospheric Blocking in an Aquaplanet and the Impact of Orography	<ul style="list-style-type: none"> • Blocking can be generated even in the absence of zonally asymmetric forcing • An idealized moist GCM can generate physically consistent blocking climatologies and blocking dynamics • Adding Gaussian mountains ≥ 2 km in height results in significantly more blocking than an aquaplanet configuration • Blocking is anchored near the high-pressure anomaly of stationary waves generated by orography • Blocking is suppressed near low-pressure stationary wave anomalies and regions where background zonal flow maximizes
2. Blocking and General Circulation in GFDL Comprehensive Climate Models	<ul style="list-style-type: none"> • GFDL's coupled atmosphere-ocean model, CM4, has an equatorward shifted zonal flow compared to the atmosphere only model, AM4, consistent with a contraction of Hadley circulation • The models have similar biases in the stationary wave where blocking is most ubiquitous. The stationary wave is too strong in Pacific, and too weak in Atlantic • Despite differences in zonal circulation, the models produce similar blocking climatologies and exhibit shared biases compared to reanalysis. Too much blocking in the Pacific and too little in the Atlantic • Suggestion that blocking biases could be more driven by stationary wave biases than zonal flow biases • The models produce realistic transient eddy forcing and geopotential height fields during blocking onset
3. Connections Between Atmospheric	<ul style="list-style-type: none"> • The association of blocking with heat extremes exhibits strong regional variation

Blocking and Heat Extremes in Current and Possible Future Climates	<ul style="list-style-type: none"> • Heat extremes associated with atmospheric blocking are warmer and longer than those that are not associated with blocking • Leading into the onset of heat events, diabatic processes warm the region. One day prior to onset and throughout lifecycle, subsidence acts to help sustain warming • GFDL CM4 reliably simulates blocking and its association with heat events throughout most of the Northern Hemisphere • In RCP 8.5 simulation of CM4, less blocking is generated compared to historical integration. Less blocking is also associated with heat extremes. On average, heat extremes in RCP 8.5 have less warm anomalous 2 m temperatures, but this is outweighed by a warmer mean state.
--	--

Table 5.1. For each of the three thesis research components, a summary of key takeaways.

5.4 Concluding remarks

This thesis elucidates fundamental information about the climatology, dynamics, and impacts of atmospheric blocking in a variety of models and climate forcing conditions. The knowledge gained from this thesis, however, is not just limited to blocking. In general, this thesis is a study of geophysical fluid dynamics (GFD) and atmospheric science put into the context of blocking.

This all begins with the Navier-Stokes equation on a rotating sphere. After making some simplifying assumptions, an analytical theory of stationary Rossby waves can be derived, which directly relates to blocking. Then to fully understand the physics of blocking, numerous other concepts within GFD are involved. This includes concepts such as stationary wave theory, eddy-eddy interactions, Rossby wave-breaking, conservation of wave activity flux, mean-state features, dry and moist dynamics, as well as many others.

This work also involved other knowledge outside the realms of physics. For example, development of the block tracking algorithm required an understanding of image processing, while analysis of data often required statistical and numerical methods. In terms of generating data, this

work also required learning how to configure and run an idealized model under various forcing conditions.

Performing this Ph.D. research has been an enriching experience where I have further developed numerous skills and established myself as a scientist. My work has documented our best efforts to simulate blocking, as well as furthered our understanding of this phenomenon. Still, there is much work to be done to better understand the physics of blocking and optimize our simulation of them. Such work is necessary to ultimately understand not just how blocking, but weather and climate in general, will change in future climates.

Chapter 6

STEM Education and Diversity Research: Mentoring Youth through COVID and Beyond: Combatting Loneliness, Opportunity Gaps, and Underrepresentation in STEM

Veeshan Narinesingh, Farrah Simpson, Tracy Edwards, and Milena Chakraverti-Wuerthwein
Supervised by Dr. Gillian Bayne and Dr. Stan Altman

Abstract

Purpose

This article describes the structure and benefits of The National Society of Black Physicists and Harlem Gallery of Science Mentoring Program – a culturally relevant, virtual mentoring program for youth from underserved communities. The program was successfully piloted during the COVID-19 pandemic. The goals: combat students' feelings of loneliness, build a community, bridge opportunity gaps, and help address underrepresentation within STEM disciplines.

Design/Methodology/Approach

Middle and high school mentees were matched with university student mentors who shared similar interests and racial, ethnic, and sociocultural backgrounds. Mentors and mentees engaged in weekly structured conversations as well as tri-weekly educational and professional development workshops. IPA analysis (Smith, 1996) was applied to transcripts from focus group interviews and program events to identify superordinate and subordinate themes amongst mentee outcomes.

Findings

Mentees were able to receive numerous benefits from the program. Various superordinate (subordinate) themes were identified: social-emotional support (support with mental health, and family-like bonds and inclusivity), building paths to academic and professional success (demystifying success, and skills for success), and supporting connections to STEM (nurturing interests in STEM, and seeing oneself in STEM careers).

Originality/Value

This article describes a novel, virtual, STEM-focused mentoring program that incorporates and celebrates the identities and cultures of its students. At its base, the program matches youth from underserved communities with mentors who share similar backgrounds and interests. The program model was found to have positive outcomes on mentees and shows great potential to be continued and replicated beyond the COVID-19 pandemic.

6.1 Introduction

For most students, the COVID-19 pandemic has been a stressful time associated with loneliness and isolation (Loades et al. 2021). Beyond the pandemic, however, an even greater crisis has been the historic inequity amongst educational opportunities for members of Black² and Hispanic³ communities (Roscigno 2000). Such inequities ripple across many fields, but particularly affected are Science, Technology, Engineering, and Mathematics (STEM) disciplines.

² “The term Black is used to refer to people of the African Diaspora and to such populations that reside within the United States.” (Bayne 2021)

³ “While it is widely accepted that Hispanic people are those who originate from Spanish speaking countries; Latino people descend from Latin-American countries, but their language is not necessarily Spanish; and that Latinx is a gender-neutral, pan ethnic identifier” (Bayne 2021). For brevity, this article uses Hispanic as an identifier to include the aforementioned groups.

The National Center for Science and Engineering Statistics (2021) reported that in 2018, 57.9% of Science and Engineering bachelor's recipients were White, whereas 15.1% were Hispanic and 8.5% were Black. Furthermore, Pew Research (2021) found that amongst science, technology, engineering, and mathematics (STEM) professionals, a mere 8% were Hispanic and 9% were Black; on the other hand, 67% were White.

The following article explains the organization, implementation, and outcomes from the first-year pilot of the National Society of Black Physicists (NSBP) and Harlem Gallery of Science (HGS) Mentoring Program (2020-2021 academic year), during the height of the pandemic. The goals of this mentoring program were to combat students' feelings of loneliness, build a community, bridge opportunity gaps, and help address underrepresentation within STEM disciplines.

6.1.a A Mentoring Program To Combat Loneliness, Opportunity Gaps, And Underrepresentation

Killgore et al. 2020 found loneliness during COVID-19 to be strongly linked to depression. Among adolescents and young adults, Mai et al. (2021) found that having the support of closely connected individuals was correlated with the implementation of positive coping strategies to combat loneliness. Mai et al. (2021) also found that greater levels of perceived social support lowered students' general anxiety.

In 2008, Page described how diversity within organizations can lead to enhanced successes. Pascarella et al (2014) found that diversity experiences led to higher levels of critical thinking and cognitive abilities amongst college students. In *Fear of a Black Universe: An Outsider's Guide to the Future of Physics* (2021), Stephon Alexander argues that "diversity in science is not just a social justice concern, but that it enhances the quality of the science we accomplish.". Within

diverse spaces, various perspectives, ideas, and cultural lenses are able to coalesce, enhancing the scientific product. Dr. Alexander has spent the last decade working to expand the number of Black students entering the Physics profession, first at Dartmouth College in 2013 as the Director of the E.E. Just Program and starting in 2016 in the Physics Department at Brown University. He is also the 2020-2021 President of NSBP.

In addition to the COVID-19 pandemic and underrepresentation in STEM, several findings motivated the creation of the NSBP-HGS Mentoring Program. Reid and Moore (2008) found that extracurricular activities and mentors help facilitate college readiness amongst first generation students. Extracurriculars have also been found to help students develop skills and show them a variety of career paths (Hines et al. 2019). Furthermore, students are found to foster better relationships with mentors they can identify with (Ensher and Murphy 1997, Armakan et al. 2012).

In Summer of 2020 the NSBP-HGS mentoring program was conceived by Dr. Stephon Alexander. This program utilizes culturally relevant (Bayne 2012; Emdin, Beacon Press 2016) contexts to connect middle and high school students with STEM mentors who “remind them of themselves”. Throughout the academic year, mentors and mentees held weekly virtual meetings over two 12-week semesters. The goal: to build sustained, academic focused relationships. These conversations were designed to empower both mentors and mentees to be successful academically, professionally, socially, and emotionally. Mentors and mentees also took part in academic and professional development workshops throughout the year. These workshops bring together STEM disciplines, along with student culture and identities.

6.1.b INSTITUTIONS IN COALITION

6.1.b.i THE NATIONAL SOCIETY OF BLACK PHYSICISTS

NSBP was founded in 1977 at Morgan State University as a response to systemic racism in the physics community. In 1972, African American physicists curated an event celebrating the successes of African American physicists. These meetings led to the creation of a national organization for Black physicists eventually known as NSBP. NSBP aims to promote the wellness of Black physicists and scientists by developing and supporting efforts that increase their opportunities in physics. NSBP is the largest and most renowned organization dedicated to the advancement and wellness of Black physicists. Most notably, NSBP holds an annual conference that brings together Black physicists from all over the country to share and engage with each other's research.

6.1.b.ii Science And Arts Engagement New York’s Harlem Gallery Of Science

Science and Arts Engagement New York, Inc. (SAENY), a not-for-profit organization, working in collaboration with the City College of New York (CCNY), created the Harlem Gallery of Science. HGS is as a free venue to facilitate access and engagement of underrepresented communities to STEM fields. To date the HGS has held two public exhibits: *Dunk! The Science of Basketball* and *The Science of Music: From Jazz to Hip Hop*. To facilitate pathways into higher education, HGS has also completed a study on the connections of Black and Hispanic students to video games, and partners with NSBP to create and deliver the NSBP-HGS Mentoring Program.

6.2 Methodology

6.2.a Program Structure

The NSBP-HGS mentoring program utilizes a multi-level group mentoring model (Fig. 6.1). At its base, the program matches one middle (MS; 6-8th Grade) and one high school (HS; 9-12th Grade) mentee with a university student mentor. Mentors can be either undergraduate or graduate students. Within this structure, mentees interact vertically with their mentor, but also horizontally with their co-mentee.

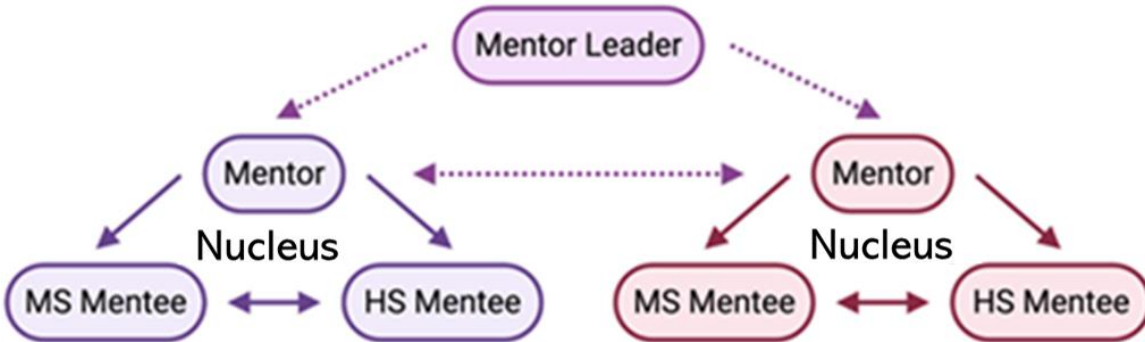


Figure 6.1. Schematic of the multi-level group mentoring model used by the National Society of Black Physicists and Harlem Gallery of Science Mentoring Program. MS denotes middle school students; HS denotes high school students.

A single group consisting of one mentor with two mentees is referred to as a mentoring nucleus or small group. We note, however, that there is some degree of flexibility to this structure based on mentee needs and mentor availability. Mentoring nuclei are matched based on common interests and sociocultural backgrounds. Matching information is extracted from surveys that are part of the mentor and mentee application processes.

The next level within our model matches groups of two to four mentors with a mentor leader (Fig. 6.1). A mentor leader is a university student who is very experienced in mentoring. The role of the mentor leader is to guide mentors in building and sustaining strong mentoring relationships with their mentees. Mentor leaders also run mentor training workshops and cohort events (see section 6.2.c) and can provide additional support advising mentees. By the conclusion

of the mentoring program's year 1 pilot (2020-2021), the entire cohort consisted of 18 mentees, 12 mentors, 4 mentor leaders

The leadership of NSBP and SAENY oversaw the program and met with mentor leaders to provide guidance as needed. The leadership team consisted of Dr. Stephon Alexander (Brown University professor, 2020-2021 president of NSBP), as well as Dr. Brian Schwartz (SAENY Board Chair) and Dr. Stan Altman (SAENY President), both tenured Professors at the City University of New York.

6.2.b Participants And Identity

6.2.b.i Mentees

Mentees in the program are sourced from institutions based in the Harlem neighborhood of New York City. Harlem has been known to be a great hub of Black and Hispanic culture, but also communities that are underserved (Gill 2011). For year 1, the three source institutions consisted of a public middle school, a public middle and high school, and an outside-of-school academic support program.

For Phase I of the pilot (Fall 2020 semester), mentees were recruited by their teachers. The criteria for recruitment were based on a student's demonstration to show potential. We found that recruiting in this way led to some who were not fully committed. The following semester (Spring 2021), potential mentees were given in-class presentations about the mentoring program and applied based on their own personal interest. Mentor Leaders accepted mentees based on applications, teacher recommendations, and mentor availability. This process helped to increase student engagement.

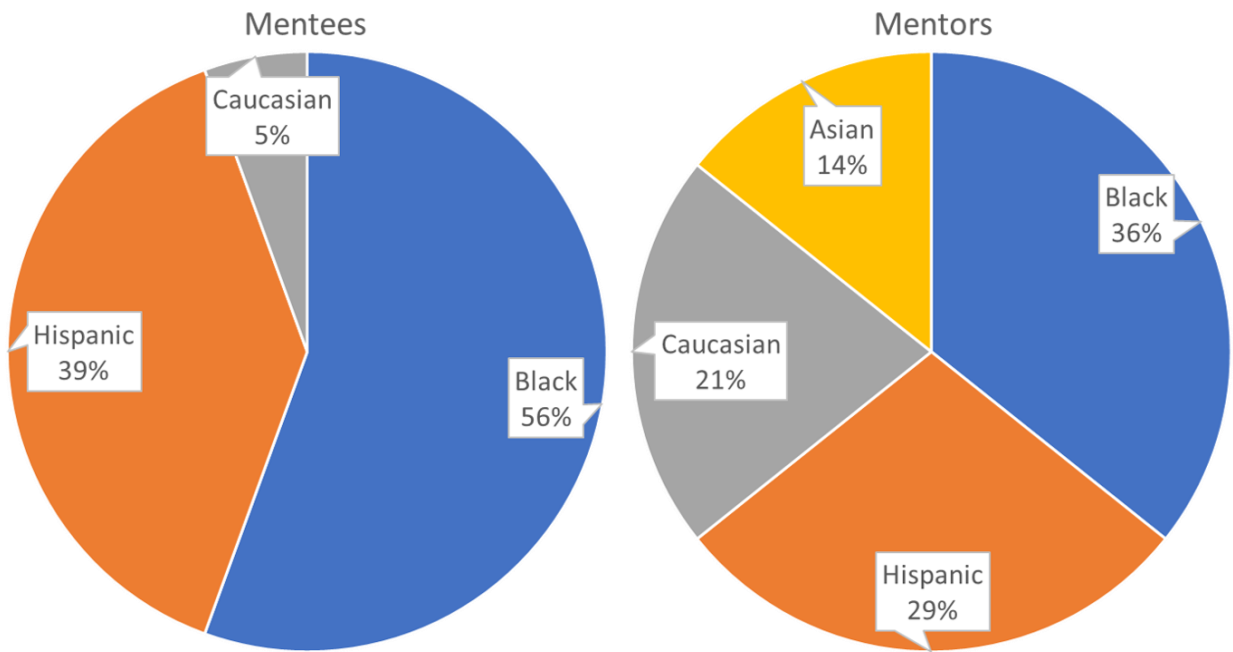


Figure 6.2. Mentee and mentor races and ethnicities by percentages.

Of the 18 Spring mentees, 10 were high school students and 8 were middle school students.

In terms of gender, 7 mentees identified as male and 11 identified as female. In terms of ethnicity and race, 10 mentees identified as black, 7 as Hispanic, and 1 as Caucasian (Fig. 2). 10 mentees identified as being 1st or 2nd generation immigrants; Regions of origin included West Africa, Latin America, and the Caribbean.

6.2.b.ii Mentors

Mentors consisted of 5 undergraduate and 7 graduate students from 7 universities across the United States. Roughly 50% of the mentors were from NSBP and 50% were affiliated with HGS and neighboring universities, particularly The City University of New York. Mentors applied to the program by responding to program solicitation emails. They were then interviewed and selected by mentor leaders. Mentors were selected based on their commitment to helping others, as well as their dedication to building community and advancing the inclusivity of STEM spaces.

The 12 mentors were diverse in terms of gender, ethno-racial background, and major within STEM disciplines. 50% of the mentors were female and 50% were male. 5 mentors identified as Black, 4 as Hispanic, 3 as Caucasian, and 2 as Asian (Fig. 6.2). 2 mentors identified as multiracial. Amongst majors, 7 mentors majored in physics. 3 mentors majored in the earth science related fields of hydrology, oceanography, and geochemistry. 1 mentor majored in mechanical engineering and 1 mentor was an undeclared college freshman.

6.2.b.iii Mentor Leaders

The 4 mentor leaders were split between 2 representatives from NSBP and 2 from HGS. Mentor leaders are graduate students very experienced in mentorship and dedicated to the program's mission of advancing diversity within STEM. For the inaugural year, mentor leaders were hand selected by the presidents of NSBP and SAENY respectively.

During the Fall of 2020, two mentor leaders were female and two were male. In the spring 2021 three mentor leaders were female and one male. The races of the mentor leaders included Black, Asian, and Caucasian with two mentor leaders identifying as mixed-race individuals. Mentor leaders' areas of scholarly specialization included nuclear physics, high-energy physics, biophysics, atmospheric physics, branding and integrated communications and STEM education.

6.2.c Modes Of Supportive Engagement

To help empower students socially and academically, as well as cultivate their interest in STEM pathways, this program engages mentees, mentors, and mentor leaders in several ways. These modes of supportive engagement are designed to be cogenerative (Bayne 2009; Emdin 2016); Or, in other words, mentors and mentees collaborate with mentor leaders to generate programmatic content. The various cultures, or beliefs and practices, within the cohort are incorporated and celebrated. This effectively creates a STEM counter-space (Ong et al. 2018)

rooted in underrepresented cultures, atypical from usual White male dominated STEM spaces. The various modes of supportive engagement are explained below.

6.2.c.i Mentor Training

Starting in August, mentors went through a series of 5 monthly mentor training workshops. These workshops are developed and conducted by mentor leaders. Mentor training workshops are designed to train mentors on building and sustaining successful mentoring relationships, as well as to build a sense of community and camaraderie between mentors and mentor leaders. Workshop topics are cogenerated by the mentors, where mentor input is integrated during workshop development. Table 6.1 shows a curriculum map of the mentor training workshops.

Workshop	Objectives
Workshop 1: Orientation: What are the makings of a good mentor?	1. Meditate 2. Meet: Fellow mentors 3. Define: Mentoring 4. Discuss: The makings of a good mentor 5. Outline: program structure
Workshop 2: Cultural Sensitivity	1. Meditate 2. Recap: 1 st workshop 3. Explore: Challenges students face and how mentors can support to overcome them 4. Set: Boundaries for the mentoring relationship 5. Learn: Cultural Sensitivity

Workshop 3: Makings of a good mentor revisited Prelude to first contact	1. Meditate 2. Recap: Workshops 1 and 2 3. Discuss: What's key in starting up a successful mentoring relationship? 4. Revisit: The makings of a good mentor
Workshop 4: Meta Aspects of Mentoring	1. Meditate 2. Discuss: How is the mentoring going? 3. Brainstorm: What is working, what is not? 4. Look introspectively: How can we improve? 5. Learn: Mentoring sustainment and resilience
Workshop 5: Reflection	1. Meditate 2. Follow up: How have we overcome challenges we were facing as mentors? 3. Reflect: The experience as a mentor 4. Discuss: How do we continue or conclude the mentoring relationship

Table 6.1. Curriculum Map for Mentor Training Workshops.

6.2.c.ii Weekly Meetings

The paramount feature of the program is the weekly meetings between mentors and mentees. These conversations last at least 30 minutes and are held virtually. Conversations center around the mentees' academic goals, professional development, and personal experiences. Mentors have the freedom to freely discuss any topic with their mentees, but they are provided

guidance by the mentor training workshops and conversation starters curated by the mentor leaders. The conversation starters include weekly topics and goals with icebreaker questions and activities to guide the mentor-mentee discussions. The first two weeks focus on an integral part of the mentoring relationship, building trust and getting to know one another (Joplin et al. 2004). The following weeks then focus on a variety of topics from goal setting to studentship, STEM kits, careers, and applying to college.

6.2.c.iii Stem Kits

To develop skills and cultivate student interest in STEM, “STEM kits” containing various hands-on activities are mailed to all mentors and mentees. The kits aim to expose students to new ideas, broadening their understanding of STEM-related material. As a group, each mentoring nucleus chooses 2 kits from a predetermined list of over 12 kits. Examples of kits include ornithology, computer programming and robotics, microscopy, laser optics, and botany. During STEM kit focused sessions, mentors and mentees explore and inquire together, further developing their bond. In addition, students sharpen their problem-solving and tactile skills. Students are able to keep all of their materials, and several mentees described sharing the experience with family members.

6.2.c.iv Cohort Events

The program holds tri-weekly social, academic, and professional development events for the entire mentor-mentee cohort. These cohort events are inclusive and celebratory of the various cultures within the cohort. Events are typically cogenerated and co-led by mentor leaders, mentors, and mentees. Each semester begins with a kickoff event to welcome program members.

Cohort events are hosted with the goal of exposing mentors and mentees to science in their daily lives as well as to develop skills and introduce career paths. The inaugural cohort event was

“The Physics Hip Hop” by Dr. Stephon Alexander. Other examples of cohort events included: “How to Be a Strong Scholar”, “The Art of Hustle and Success”, “Career Day”, and an “End of The Year Fete”.

6.2.c.v Mindfulness Practice

This mentoring program implements mindfulness practice to promote the psychological wellbeing of all students involved. For those from underserved communities, mindfulness can be a powerful tool for mental regulation (Mendelson et al. 2010). Enhanced cognition and attention (Brefczynski-Lewis et al. 2007), as well as a better ability to manage negative emotions and stress are all potential outcomes of mindfulness (Ospina et al 2007).

Mindfulness is featured throughout the program. Mindfulness sessions are led by mindfulness instructor Brian Simmons. Simmons is considered a pioneer in the development of mindfulness programs in NYC public schools. Sessions typically involve 15-minutes of guided meditation and reflective discussion and are held during mentor training workshops as well as cohort events. Outside of instruction by Simmons, mentors are encouraged to involve mindfulness during their weekly mentoring meetings.

6.3 Programmatic Outcomes

To investigate the outcomes of the mentoring program on mentees, their accounts were collected through weekly meeting reports, surveys, cohort event recordings, and focus group interviews. Outcomes centered around three superordinate themes: Emotional and social support, paths to success, and connections to STEM. These superordinate themes were then organized into various subordinate themes (Table 6.2) described below. Pseudonyms are utilized hereinafter to protect the identities of participants.

Superordinate Themes		
Social-Emotional Support	Building Paths to Academic and Professional Success	Supporting Connections to STEM
Subordinate Themes		
<ul style="list-style-type: none"> • Support with mental health • Family-like bonds and inclusivity 	<ul style="list-style-type: none"> • Demystifying Success • Skills for Success 	<ul style="list-style-type: none"> • Nurturing interests in STEM • Seeing oneself in STEM careers

Table 6.2. Regarding outcomes for mentees, superordinate and respective subordinate themes identified from mentee and mentor feedback.

6.3.a Social-Emotional Support

The mentoring program had positive effects on providing emotional and social support to the mentees. Within this superordinate outcome, two subordinate themes were extracted: emotional support with mental health, and family-like bonds and inclusivity.

6.3.a.1 Support With Mental Health

Mentees reported that the mentoring program provided the opportunity to vent, receive feedback, ease anxiety, and build self-confidence. Within one of the focus group interviews, high-schooler Taneisha had the following response when asked what she got out of the program:

It's good, like, it's something to look forward to at the end of the week [...]. Especially because it's like Corona now and you can't really do nothing. [...]. I can tell her [the mentor] about how my days go during the week and whether there was any problems

Taneisha has expressed her desire to remain in the program because with her mentor, “I can also talk to her about anything that is bothering me.”

High schooler Rhonda described how her meetings with her mentor

helped me grow in a way that she's helped me be able to express myself more, be comfortable with myself and be comfortable with my feelings and not be afraid to say it. I'm so glad that she's made our zooms like a safe space for us to tell her anything.

Meeting with mentors also helped mentees deal with anxiety and build confidence. Middle schooler Jayde recounted a movie night with her mentor:

I'm a person who is indecisive, self-conscious, and have a lot of anxiety and I guess that was the perfect day to show me that film because I was a person that didn't really believe in myself and the message of the movie and the encouragement of [Jayde's mentor] was really amazing and that gave me a lot of confidence. [...]. It was a reminder that I should never doubt myself and that I know what I am doing and just believing and trusting in me and who I am I will achieve success.

Other mentees also expressed receiving emotional support. Ayanna, a middle schooler, described the weekly meetings as “very comforting” because “right now not everyone has someone to talk to”. High schooler, Aya, reported that she grew “relationship wise” and “friendship wise” and asked if mentees could spend more time with mentors. Regarding mindfulness, high schooler Lorenzo mentioned how he “learned how to calm down more from the meditation”.

6.3.a.2 Family-Like Bonds And Inclusivity

One of the purposes of the program is to build social skills by engendering feelings of family-like bonds and inclusivity. When mentees were surveyed on what they got out of the program, some mentees explicitly mentioned the program “helped build social skills” and made them “more confident in my speaking skills”.

When asked about his mentor, high schooler Abdullah stated, “I don’t see him as a mentor, I see him as a big brother”. Rhonda shared similar sentiments in one of the focus groups. Rhonda

described Alyssa as an “older sister”, and the entire program as like “a second family”. Rhonda went on to describe the program:

It’s a more laid-back kind of vibe, it’s like a family, and you know with your family you don’t put up an act or character because they’re your family. [...]. The program was very inclusive, and they didn’t make me feel like I had to act a certain way.

Other students also explicitly described feelings of inclusivity within the program. Mentees were surveyed on if they felt part of the community/family within the program. High schoolers Lorenzo and Justin stated, “Yes. I feel that I am a part of the family because everyone feels so inclusive”, and “Yes because people are very nice and include people in everything”. Another student described their experience as being “very well welcomed” and the program as “a community that cares for each other”.

6.3.b Building Paths To Academic And Professional Success

The mentoring program positively affected the academic and professional development of mentees. This development centered around two subordinate themes: demystifying success and skills for success.

6.3.b.1 Demystifying Success

Students from underrepresented groups often face the barrier of not having parents who have successfully pursued higher education (Hines et al. 2020). One outcome of this mentoring program has been showing mentees that college and STEM careers are attainable, even by those from underrepresented groups. The mentors, after all, are living examples of this.

In one of the focus group interviews, high schooler Lorenzo described how his mentor helped ease some of his concerns about attending college:

I always thought that once you finish high school it is just going to be a bunch of complicated stuff. You are going to have no idea about what you want to do. [...]. What I saw when [the mentor] was talking to me about the stuff that he did; he made it seem more streamlined, like what you can do and the way that it flows. [...] It makes me less anxious about finishing high school and going to college.

In addition, when asked about his favorite part of the program, Lorenzo stated:

[...] With the mentors because you find out a lot of relatable things. You find out that they weren't no crazy prodigy. That they were just a normal student that put in work, had good opportunities, and took them.

Abdullah shared similar sentiments. During one of his cohort event presentations, he described the effects of his interaction with a mentor leader:

I want to thank Garlin. He has motivated me in order to believe in myself because he came from nothing to something. [...] I would like to thank this program for putting me on the right path to success in life.

For some students, success was demystified by being redefined completely. In a focus group interview, Rhonda had this to say about how the program helped her redefine success:

The program has helped me not be too hard on myself and it gave me a new understanding of what success is. I feel like especially for my family, this way of thinking, and especially having parents that are immigrants, their idea of success is when you do your school work you have to get all A's [...] so you can become a doctor or lawyer [...] the program has showed me success is not in regards of money, it's not only in regards of grades, because grades don't define who you are [...] You can be successful because you were able to

achieve a goal for yourself that you think you wouldn't be able to achieve. You can be successful because you were able to help somebody.

6.3.b.2 Skills For Success

The mentoring program also helped to equip mentees with some of the skills necessary for academic and professional success. As such, weekly mentor meetings and cohort events centered around topics such as goal setting, time management, communication skills, and studentship.

Goal setting skills were heavily emphasized within the program. Middle schooler Ayanna had this to share:

I also learned important things, one of them being realistic goals that you can get done. 'Cause most of the time as humans we set unrealistic goals that we do not get done, that brings a very unhealthy feeling to us. So that is a thing I practice now.

Another middle schooler, Shirley, shared, “I feel like I’m a lot more organized in goal setting”, when asked about the program’s impact. High schooler Reina was asked if this program helped with being successful academically, she responded:

It's helped me set goals when it came to school. When we first started this part of the program we had to set goals [...] I set goals [...] to help me better understand my coding class. I was able to talk to my mentors and we would catch up on it and it actually helped get a better grade in that class.

Time management was also emphasized. High schooler Taneisha was very expressive about the program’s impact on her when it came to this. In a focus group with her mentor Lisa the following dialogue unfolded:

Taneisha: [...] We were working on, [...] procrastination. We was working on that because I procrastinate a lot.

Lisa: Time management, yeah.

Taneisha: Yeah [...] and I'm getting better at it. But, I mean for real. I am really doing better. In my Spanish class we started semester two yesterday. [...] my Spanish teacher... he put up 20 assignments that was due before the second semester [...] So now I got five assignments left. I did it in two days!

Taneisha was even able to offer advice to Lorenzo, who asked about combatting procrastination at a cohort event. This was her response:

Me and Lisa have talked about it and we were saying that we could do a checklist kind of. [...] Write out what you have to do and cross each thing out as you do them. So like it's getting done, and having your phone off or in another room or something so you can't hear it when it goes off.

Lorenzo then went on to report that with his mentor he “formed a little day schedule that I go through, it feels more organized”.

Mentees reported developing other essential skills as well. In his cohort event presentation about studentship, Abdullah, who is an ESL student, spoke of the program’s impact:

The third bullet point is for elevating my leadership and communication skills. I was not able to do presentations 3 months ago, I was very shy and look at me right now, I'm presenting some topics, [...], in front of many people. [...]

In another example, Sherence described how the program enhanced his general studentship. He described his favorite cohort event in the post survey:

My favorite event was how to be a good student. I liked this because it taught me to be better in class. I upped my grades across the board, I took more notes, and I was able to focus more, and improve all my tests

6.3.c Supporting Connections To Stem

Two subordinate themes emerged upon analyzing mentees' connections to STEM as a result of this program. The first centered on nurturing interests in STEM, and the second was related directly to careers.

6.3.c.1 Nurturing Interests In Stem

Many of the mentees had pre-existing interests in STEM. This is likely due to them being recruited by their science teachers or during science class by the mentor leaders. Still, through this program mentees were able to further explore those interests. Jayde for example, described how she learned that science connected to her everyday life in a focus group interview:

[...] The leader of this program [Dr. Alexander] and he was talking about how music and science relate to one another, and I didn't really know that. [...] in our sessions too, we learned about astronomy and we learned about you being physicists. [...] And we learned about the different sciences [...] I get to know more about science, which helps me a lot with you know the science I do and math as well. So it is really interesting to know that there is a lot of different ways that science has proceeded and it is really awesome!

The STEM kits also provided opportunities for students to cultivate their interests in STEM. In one of Jayde's meeting reports, she noted that for her group's botany experiment "we had a good time and had fun discovering/exploring together". Abdullah and his mentor even put together a highlight reel of their laser optics kit and presented it at the end of the year celebration event. For Shirley and Ayanna, their microscope kits were interesting experiences and their first time ever interacting with such devices. Ayanna noted that it was her favorite part of the program, and she shared the experience with her family.

6.3.c.2 Seeing Oneself In Stem Careers

The program also helped reaffirm mentee interest in STEM careers, excite interests in other STEM fields, and helped guide mentees further along STEM pathways. Shirley's mentor nominated her for the program's STEM Kit Innovation Award, citing how the kit nurtured Shirley's career interests:

[...] After receiving the kits, Shirley has been increasingly interested in biology and creative with using the kit in her everyday life. This first-time experience of being introduced to a science project she had no exposure to, reinforced her desire to pursue a science career in becoming a neonatologist

Others expanded their interests in STEM. In his pre-program survey, middle schooler Manuel originally listed scientist as his career interest. As the year progressed, however, Manuel's interests grew to data scientist, teacher, physician, physicist, and astronomer. Abdullah originally applied to college as a finance major, but ultimately ended up switching to mechanical engineering once he was accepted. Lorenzo had the following to say when asked if the program made him more interested in STEM and STEM careers:

[...] Right now I'm just in the process of trying different things [...] I told you guys I like gaming a lot, you guys got me into a good gaming program [...]. It's like you take my interests and you expand on them. [...] I wouldn't say I have a final decision like I want to do something that involved STEM, but it's more like I want to try out things more that involve STEM

Mentees also reported being able to further their pursuit of STEM careers. In one of the focus group interviews, Reina recounted her interactions with the presenters during career day:

I was already interested in STEM so seeing people actually achieved their goal and being able to ask questions to people that work in this field also made me more interested in it and made me want to do it even more.

In addition, Lorenzo and another high school mentee, Tristan, were able to take part in paid summer research internships as a result of connections made within the mentoring program.

6.4. Discussion And Conclusion

6.4.a Key Takeaways

Holistically speaking, the following quote from Jayde represents the NSBP-HGS Mentoring Program's effect on mentees:

When I first got into this program I thought it was all about science and math and how you help, but it turns out it's a lot more than that... it's about, reaching social skills, building up this foundation, and also, reaching that goal ... I think it is a really good program that really sets a mutual relationship, and it really nurtures students, and teaches them different skills

Positive outcomes pertaining to three superordinate themes were identified as a result of the mentoring program. The first of these themes is social-emotional support. Mentees reported that conversations with mentors helped provide encouragement, ease anxiety, and gave mentees opportunities to express their feelings. Mentees also reported feeling family-like bonds between mentors and other program members in a safe, inclusive space.

The second superordinate theme centered around building paths to success. Given that mentors come from similar sociocultural backgrounds as mentees, mentors serve as living examples of the mentees' future selves. Mentors not only show mentees what it takes to succeed

in STEM career pathways, but also that success is actually attainable. In addition, the program helps develop the social, academic, and professional skills of mentees.

The third superordinate theme pertains directly to mitigating underrepresentation, focusing on supporting student connections to STEM. The program was able to foster mentees' interest and knowledge in STEM topics. This was achieved primarily through cohort events and the STEM kit activities. Mentees were also educated about careers in STEM. Some mentees gained new-found interest regarding specific STEM careers, while others had their interests affirmed and learned of the next steps necessary to achieve their career goals.

6.4.b Improvements And Future Plans Beyond Covid

Based on mentor and mentee feedback, several areas for program improvement were identified. One suggestion from mentors was to recruit less students that were already high-level academic achievers. The greater number of mentees with high versus other levels of academic achievement was likely a result of the recruitment process. One way to improve this is to have teachers recommend their students from last year who show potential but cover a range of academic achievement levels.

Mentees suggested that the program create better opportunities for mentee-mentee interaction. Mentees noted that though they created deep bonds with their mentors, their relationships with the other mentees were not strong. Mentees have suggested the idea of a mentee debate or competition to develop comradery.

In terms of future plans, pending funding, the program hopes to expand and eventually replicate our virtual model in other places and institutions. This program is of value even when COVID-19 eventually fades because adolescents will always face challenges around loneliness, isolation, and achieving academic success. In addition, the mentoring program also seeks to

provide further insight into optimal ways of getting young people from underrepresented groups successfully through STEM career pathways. Practical plans for program improvement for 2021-2022 include holding a STEM kit symposium, introducing “mentoring houses”, and further refinement of our model.

References (Chapter 6)

Alexander, S. (2021), *Fear of a Black Universe An Outsider's Guide to the Future of Physics*, Basic Books.

Bayne, G. (2009) “Cogenerative Dialogues”, Roth, W.M., Tobin, K., *The World of Science Education*, Brill, The Netherlands, pp. 513–527.

Bayne, G. (2012), “Capturing essential understandings of the urban science learning environment”, Springer Netherlands, Dordrecht, Vol. 15 No. 2, pp. 231–250.

Bayne, G. (2021), “NSBP-HGS Mentoring Program, June 2021 Evaluation Report”, unpublished report

Brefczynski-Lewis, J.A., Lutz, A., Schaefer, H.S., Levinson, D.B. and Davidson, R.J. (2007), “Neural Correlates of Attentional Expertise in Long-Term Meditation Practitioners”, National Academy of Sciences, United States, Vol. 104 No. 27, pp. 11483–11488.

Emdin, C. (2016), *For White Folks Who Teach in the Hood... and the Rest of y'all Too*, Beacon Press, New York

Ensher, E.A. and Murphy, S.E. (1997), “Effects of Race, Gender, Perceived Similarity, and Contact on Mentor Relationships”, Elsevier Inc, Vol. 50 No. 3, pp. 460–481.

Gill, J. (2011), *Harlem*, Grove Press, New York, NY.

Hines, E.M., Cooper, J.N. and Corral, M. (2019), “Overcoming the odds”, Vol. 13 No. 1, pp. 51–69.

Joplin, C.P., Orman, B. and Evans, K.D. (2004), “The essence of M&M'S: Mentoring Minority Students”, Vol. 17 No. 3.

Killgore, W.D., Cloonan, S.A., Taylor, E.C. and Dailey, N.S. (2020), “Loneliness: A signature mental health concern in the era of COVID-19”, Elsevier B.V, Ireland, Vol. 290, p. 113117.

Leyton-Armakan, J., Lawrence, E., Deutsch, N., Lee Williams, J. and Henneberger, A. (2012), “Effective youth mentors: The relationship between initial characteristics of college women mentors and mentee satisfaction and outcome”, Vol. 40 No. 8, pp. 906–920.

Loades, M.E., Chatburn, E., Higson-Sweeney, N., Reynolds, S., Shafran, R., Brigden, A., Linney, C., *et al.* (2020), “Rapid Systematic Review: The Impact of Social Isolation and Loneliness on the Mental Health of Children and Adolescents in the Context of COVID-19”, Elsevier Inc, United States, Vol. 59 No. 11, pp. 1218-1239.e3.

Mai, Y., Wu, Y.J. and Huang, Y. (2021), “What Type of Social Support Is Important for Student Resilience During COVID-19? A Latent Profile Analysis”, Frontiers Media S.A, Vol. 12, p. 646145.

Mendelson, T., Greenberg, M., Dariotis, J., Gould, L., Rhoades, B. and Leaf, P. (2010), “Feasibility and Preliminary Outcomes of a School-Based Mindfulness Intervention for Urban Youth”, Springer US, Boston, Vol. 38 No. 7, pp. 985–994.

National Center for Science and Engineering Statistics (2021), *Women, Minorities, and Persons with Disabilities in Science and Engineering: 2021*, Special Report NSF 21-321, Alexandria, VA

Ong, M., Smith, J.M. and Ko, L.T. (2018), “Counterspaces for women of color in STEM higher education: Marginal and central spaces for persistence and success”, Vol. 55 No. 2, pp. 206–245.

- Ospina, M.B., Bond, K., Karkhaneh, M., Tjosvold, L., Vandermeer, B., Liang, Y., Bialy, L., *et al.* (2007), “Meditation practices for health: state of the research”, United States. Agency for Healthcare Research and Quality, United States, No. 155, pp. 1–263.
- Page, S.E. (2008), *The Difference*, Princeton University Press, Princeton, NJ
- Pascarella, E.T., Martin, G.L., Hanson, J.M., Trolian, T.L., Gillig, B. and Blaich, C.F. (2014), “Effects of Diversity Experiences on Critical Thinking Skills Over 4 Years of College”, Johns Hopkins University Press, Baltimore, Vol. 55 No. 1, pp. 86–92.
- Pew Research Center (2021), “STEM Jobs See Uneven Progress in Increasing Gender, Racial and Ethnic Diversity”
- Reid, M.J. and Moore, J.L. (2008), “College Readiness and Academic Preparation for Postsecondary Education”, Sage Publications, Los Angeles, CA, Vol. 43 No. 2, pp. 240–261.
- Roscigno, V.J. (2000), “Family/School Inequality and African-American/Hispanic Achievement”, Vol. 47 No. 2, pp. 266–290.
- Smith, J.A. (1996), “Beyond the divide between cognition and discourse: Using interpretative phenomenological analysis in health psychology”, Taylor & Francis Group, Vol. 11 No. 2, pp. 261–271.

References (Chapters 1-5)

- Abatzoglou, J. T., G. Magnusdottir, 2006: Planetary Wave Breaking and Nonlinear Reflection. *Journal of Climate*, **19**, 6139-6152, doi:10.1175/JCLI3968.1.
- Adcroft, A., W. Anderson, V. Balaji, C. Blanton, M. Bushuk, C. O. Dufour, J. P. Dunne, S. M. Griffies, R. Hallberg, M. J. Harrison, I. M. Held, M. F. Jansen, J. G. John, J. P. Krasting, A. R. Langenhorst, S. Legg, Z. Liang, C. McHugh, A. Radhakrishnan, B. G. Reichl, T. Rosati, B. L. Samuels, A. Shao, R. Stouffer, M. Winton, A. T. Wittenberg, B. Xiang, N. Zadeh, and R. Zhang, 2019: The GFDL Global Ocean and Sea Ice Model OM4.0: Model Description and Simulation Features. *Journal of advances in modeling earth systems*, **11**, 3167-3211, doi:10.1029/2019MS001726.
- Anstey, J. A., P. Davini, L. J. Gray, T. J. Woollings, N. Butchart, C. Cagnazzo, B. Christiansen, S. C. Hardiman, S. M. Osprey, and S. Yang, 2013: Multi-model analysis of Northern Hemisphere winter blocking: Model biases and the role of resolution. *Journal of geophysical research. Atmospheres*, **118**, 3956-3971, doi:10.1002/jgrd.50231.
- Barnes, E., J. Slingo, and T. Woollings, 2012: A methodology for the comparison of blocking climatologies across indices, models and climate scenarios. *Clim Dyn*, **38**, 2467-2481, doi:10.1007/s00382-011-1243-6.
- Barnes, E. A., D. L. Hartmann, 2010: Influence of eddy-driven jet latitude on North Atlantic jet persistence and blocking frequency in CMIP3 integrations. *Geophysical research letters*, **37**, n/a, doi:10.1029/2010GL045700.
- Barnes, E. A., L. Polvani, 2013: Response of the Midlatitude Jets, and of Their Variability, to Increased Greenhouse Gases in the CMIP5 Models. *Journal of climate*, **26**, 7117-7135, doi:10.1175/JCLI-D-12-00536.1.

Barnes, E. A., J. Slingo, and T. Woollings, 2011: A methodology for the comparison of blocking climatologies across indices, models and climate scenarios. *Clim Dyn*, **38**, 2467-2481, doi:10.1007/s00382-011-1243-6.

Barriopedro, D., R. García-Herrera, and R. Trigo, 2010: Application of blocking diagnosis methods to General Circulation Models. Part I: a novel detection scheme. *Clim Dyn*, **35**, 1373-1391, doi:10.1007/s00382-010-0767-5.

Berggren, R., B. Bolin, and C. -. Rossby, 1949: An Aerological Study of Zonal Motion, its Perturbations and Break-down. *Tellus*, **1**, 14-37, doi:10.3402/tellusa.v1i2.8501.

Berrisford, P., B. J. Hoskins, and E. Tyrlis, 2007: Blocking and Rossby Wave Breaking on the Dynamical Tropopause in the Southern Hemisphere. *Journal of the Atmospheric Sciences*, **64**, 2881-2898, doi:10.1175/JAS3984.1.

Booth, J. F., E. Dunn-Sigouin, and S. Pfahl, 2017: The Relationship Between Extratropical Cyclone Steering and Blocking Along the North American East Coast. *Geophysical research letters*, **44**, 11,976-11,984, doi:10.1002/2017GL075941.

Booth, J. F., V. Narinesingh, K. L. Towey, and J. Jeyaratnam, 2021: Storm Surge, Blocking, and Cyclones: A Compound Hazards Analysis for the Northeast United States. *Journal of applied meteorology and climatology*, , doi:10.1175/JAMC-D-21-0062.1.

Bowley, K. A., J. R. Gyakum, and E. H. Atallah, 2019: A New Perspective toward Cataloging Northern Hemisphere Rossby Wave Breaking on the Dynamic Tropopause. *Monthly Weather Review*, **147**, 409-431, doi:10.1175/MWR-D-18-0131.1.

Brayshaw, D. J., B. Hoskins, and M. Blackburn, 2009: The basic ingredients of the North Atlantic storm track. Part I: Land-sea contrast and orography. *Journal of the atmospheric sciences*, **66**, 2539-2558, doi:10.1175/2009JAS3078.1.

- Brayshaw, D. J., B. Hoskins, and M. Blackburn, 2009: The Basic Ingredients of the North Atlantic Storm Track. Part I: Land–Sea Contrast and Orography. *Journal of the Atmospheric Sciences*, **66**, 2539-2558, doi:10.1175/2009JAS3078.1.
- Brunet, G., 1994: Empirical normal-mode analysis of atmospheric data. *Journal of the atmospheric sciences*, **51**, 932-952, doi:10.1175/1520-0469(1994)051<0932:ENMAOA>2.0.CO;2.
- Brunner, L., N. Schaller, J. Anstey, J. Sillmann, and A. K. Steiner, 2018: Dependence of Present and Future European Temperature Extremes on the Location of Atmospheric Blocking. *Geophysical research letters*, **45**, 6311-6320, doi:10.1029/2018GL077837.
- Carrera, M. L., R. W. Higgins, and V. E. Kousky, 2004: Downstream Weather Impacts Associated with Atmospheric Blocking over the Northeast Pacific. *Journal of climate*, **17**, 4823-4839, doi:10.1175/JCLI-3237.1.
- Chan, P., P. Hassanzadeh, and Z. Kuang, 2019: Evaluating Indices of Blocking Anticyclones in Terms of Their Linear Relations With Surface Hot Extremes. *Geophysical research letters*, **46**, 4904-4912, doi:10.1029/2019GL083307.
- Charney, J. G., J. G. DeVore, 1979: Multiple Flow Equilibria in the Atmosphere and Blocking. *Journal of the atmospheric sciences*, **36**, 1205-1216, doi:10.1175/1520-0469(1979)036<1205:MFEITA>2.0.CO;2.
- Cheung, H. H. N., W. Zhou, 2015: Implications of Ural Blocking for East Asian Winter Climate in CMIP5 GCMs. Part I. *Journal of climate*, **28**, 2203-2216, doi:10.1175/JCLI-D-14-00308.1.

Clark, S. K., Y. Ming, I. M. Held, and P. J. Phillipps, 2018: The Role of the Water Vapor Feedback in the ITCZ Response to Hemispherically Asymmetric Forcings. *Journal of Climate*, **31**, 3659-3678, doi:10.1175/JCLI-D-17-0723.1.

Collins, M., R. Knutti, 2014: Long-term Climate Change: Projections, Commitments and Irreversibility. Anonymous .

Colucci, S. J., 1985: Explosive cyclogenesis and large-scale circulation changes: implications for atmospheric blocking. *Journal of the atmospheric sciences*, **42**, 2701-2717, doi:10.1175/1520-0469(1985)042<2701:ECALSC>2.0.CO;2.

Cook, K., I. M. Held, 1992: The Stationary Response to Large-Scale Orography in a General Circulation Model and a Linear Model. *Journal of the Atmospheric Sciences*, **49**, 525-539, doi:10.1175/1520-0469(1992)049<0525:TSRTLS>2.0.CO;2.

D'Andrea, F., S. Tibaldi, M. Blackburn, G. Boer, M. Déqué, M. R. Dix, B. Dugas, L. Ferranti, T. Iwasaki, A. Kitoh, V. Pope, D. Randall, E. Roeckner, D. Strauss, W. Stern, H. Van den Dool, and D. Williamson, 1998: Northern Hemisphere atmospheric blocking as simulated by 15 atmospheric general circulation models in the period 1979–1988. *Climate Dynamics*, **14**, 385-407, doi:10.1007/s003820050230.

Danielson, R. E., J. R. Gyakum, and D. N. Straub, 2006: A Case Study of Downstream Baroclinic Development over the North Pacific Ocean. Part II: Diagnoses of Eddy Energy and Wave Activity. *Monthly Weather Review*, **134**, 1549-1567, doi:10.1175/MWR3173.1.

Davini, P., S. Corti, F. D'Andrea, G. Rivière, and J. von Hardenberg, 2017: Improved Winter European Atmospheric Blocking Frequencies in High-Resolution Global Climate

Simulations. *Journal of advances in modeling earth systems*, **9**, 2615-2634,

doi:10.1002/2017MS001082.

Davini, P., C. Cagnazzo, S. Gualdi, and A. Navarra, 2012: Bidimensional Diagnostics, Variability, and Trends of Northern Hemisphere Blocking. *Journal of Climate*, **25**, 6496-6509, doi:10.1175/JCLI-D-12-00032.1.

Davini, P., F. D'Andrea, 2016: Northern Hemisphere Atmospheric Blocking Representation in Global Climate Models. *Journal of climate*, **29**, 8823-8840, doi:10.1175/JCLI-D-16-0242.1.

Davini, P., F. D'Andrea, 2020: From CMIP3 to CMIP6: Northern Hemisphere Atmospheric Blocking Simulation in Present and Future Climate. *Journal of climate*, **33**, 10021-10038, doi:10.1175/JCLI-D-19-0862.1.

de Vries, H., T. Woollings, J. Anstey, R. J. Haarsma, and W. Hazeleger, 2013a: Atmospheric blocking and its relation to jet changes in a future climate. *Clim Dyn*, **41**, 2643-2654, doi:10.1007/s00382-013-1699-7.

de Vries, H., T. Woollings, J. Anstey, R. Haarsma, and W. Hazeleger, 2013b: Atmospheric blocking and its relation to jet changes in a future climate. *Clim Dyn*, **41**, 2643-2654, doi:10.1007/s00382-013-1699-7.

Dee, D. P., S. M. Uppala, A. J. Simmons, P. Berrisford, P. Poli, S. Kobayashi, U. Andrae, M. A. Balmaseda, G. Balsamo, P. Bauer, P. Bechtold, A. C. M. Beljaars, L. van de Berg, J. Bidlot, N. Bormann, C. Delsol, R. Dragani, M. Fuentes, A. J. Geer, L. Haimberger, S. B. Healy, H. Hersbach, E. V. Hólm, L. Isaksen, P. Kållberg, M. Köhler, M. Matricardi, A. P. McNally, B. M. Monge-Sanz, J. - Morcrette, B. - Park, C. Peubey, P. de Rosnay, C. Tavolato, J. - Thépaut, and F. Vitart, 2011: The ERA-Interim reanalysis: configuration

and performance of the data assimilation system. *Quarterly Journal of the Royal Meteorological Society*, **137**, 553-597, doi:10.1002/qj.828.

Delworth, T. L., A. J. Broccoli, A. Rosati, R. J. Stouffer, V. Balaji, J. A. Beesley, W. F. Cooke, K. W. Dixon, J. Dunne, K. A. Dunne, J. W. Durachta, K. L. Findell, P. Ginoux, A. Gnanadesikan, C. T. Gordon, S. M. Griffies, R. Gudgel, M. J. Harrison, I. M. Held, R. S. Hemler, L. W. Horowitz, S. A. Klein, T. R. Knutson, P. J. Kushner, A. R. Langenhorst, H. Lee, S. Lin, J. Lu, S. L. Malyshev, P. C. D. Milly, V. Ramaswamy, J. Russell, M. D. Schwarzkopf, E. Shevliakova, J. J. Sirutis, M. J. Spelman, W. F. Stern, M. Winton, A. T. Wittenberg, B. Wyman, F. Zeng, and R. Zhang, 2006: GFDL's CM2 Global Coupled Climate Models. Part I. *Journal of climate*, **19**, 643-674, doi:10.1175/JCLI3629.1.

Dole, R. M., N. D. Gordon, 1983: Persistent anomalies of the extratropical northern hemisphere wintertime circulation: geographical distribution and regional persistence characteristics. *Monthly weather review*, **111**, 1567-1586, doi:10.1175/1520-0493(1983)111<1567:PAOTEN>2.0.CO;2.

Dong, L., C. Mitra, S. Greer, and E. Burt, 2018: The Dynamical Linkage of Atmospheric Blocking to Drought, Heatwave and Urban Heat Island in Southeastern US: A Multi-Scale Case Study. *Atmosphere*, **9**, 33, doi:10.3390/atmos9010033.

Dunn-Sigouin, E., S. Son, 2013: Northern Hemisphere blocking frequency and duration in the CMIP5 models. *Journal of geophysical research. Atmospheres*, **118**, 1179-1188, doi:10.1002/jgrd.50143.

Edmund K. M. Chang, Sukyoung Lee, and Kyle L. Swanson, 2002: Storm Track Dynamics. *Journal of Climate*, **15**, 2163-2183, doi:10.1175/1520-0442(2002)015<02163:STD>2.0.CO;2.

- Eyring, V., S. Bony, G. A. Meehl, C. A. Senior, B. Stevens, R. J. Stouffer, and K. E. Taylor, 2016: Overview of the Coupled Model Intercomparison Project Phase 6 (CMIP6) experimental design and organization. *Geoscientific model development*, **9**, 1937-1958, doi:10.5194/gmd-9-1937-2016.
- Fischer, E. M., R. Knutti, 2015: Anthropogenic contribution to global occurrence of heavy-precipitation and high-temperature extremes. *Nature climate change*, **5**, 560-564, doi:10.1038/nclimate2617.
- Fischer, E. M., S. I. Seneviratne, P. L. Vidale, D. Lüthi, and C. Schär, 2007: Soil Moisture–Atmosphere Interactions during the 2003 European Summer Heat Wave. *Journal of climate*, **20**, 5081-5099, doi:10.1175/JCLI4288.1.
- Frierson, D. M. W., 2007: The Dynamics of Idealized Convection Schemes and Their Effect on the Zonally Averaged Tropical Circulation. *Journal of the Atmospheric Sciences*, **64**, 1959-1976, doi:10.1175/JAS3935.1.
- Frierson, D. M. W., I. M. Held, and P. Zurita-Gotor, 2006: A Gray-Radiation Aquaplanet Moist GCM. Part I: Static Stability and Eddy Scale. *Journal of the Atmospheric Sciences*, **63**, 2548-2566, doi:10.1175/JAS3753.1.
- Frierson, D. M. W., I. M. Held, and P. Zurita-Gotor, 2007: A Gray-Radiation Aquaplanet Moist GCM. Part II: Energy Transports in Altered Climates. *Journal of the Atmospheric Sciences*, **64**, 1680-1693, doi:10.1175/JAS3913.1.
- García-Herrera, R., J. Díaz, R. M. Trigo, J. Luterbacher, and E. M. Fischer, 2010: A Review of the European Summer Heat Wave of 2003. *Critical reviews in environmental science and technology*, **40**, 267-306, doi:10.1080/10643380802238137.
- Garriott, E. B., 1904: *Long-range weather forecasts*. US Government Printing Office, .

- Geen, R., F. H. Lambert, and G. K. Vallis, 2018: Regime Change Behavior during Asian Monsoon Onset. *Journal of Climate*, **31**, 3327-3348, doi:10.1175/JCLI-D-17-0118.1.
- Grose, W. L., B. J. Hoskins, 1979: On the Influence of Orography on Large-Scale Atmospheric Flow. *Journal of the Atmospheric Sciences*, **36**, 223-234, doi:10.1175/1520-0469(1979)036<0223:OTIOOO>2.0.CO;2.
- Hassanzadeh, P., Z. Kuang, and B. F. Farrell, 2014: Responses of midlatitude blocks and wave amplitude to changes in the meridional temperature gradient in an idealized dry GCM. *Geophysical research letters*, **41**, 5223-5232, doi:10.1002/2014GL060764.
- Held, I. M., H. Guo, A. Adcroft, J. P. Dunne, L. W. Horowitz, J. Krasting, E. Shevliakova, M. Winton, M. Zhao, M. Bushuk, A. T. Wittenberg, B. Wyman, B. Xiang, R. Zhang, W. Anderson, V. Balaji, L. Donner, K. Dunne, J. Durachta, P. P. G. Gauthier, P. Ginoux, J. - Golaz, S. M. Griffies, R. Hallberg, L. Harris, M. Harrison, W. Hurlin, J. John, P. Lin, S. - Lin, S. Malyshев, R. Menzel, P. C. D. Milly, Y. Ming, V. Naik, D. Paynter, F. Paulet, V. Rammaswamy, B. Reichl, T. Robinson, A. Rosati, C. Seman, L. G. Silvers, S. Underwood, and N. Zadeh, 2019: Structure and Performance of GFDL's CM4.0 Climate Model. *Journal of advances in modeling earth systems*, **11**, 3691-3727, doi:10.1029/2019MS001829.
- Hersbach, H., B. Bell, P. Berrisford, S. Hirahara, A. Horányi, J. Muñoz-Sabater, J. Nicolas, C. Peubey, R. Radu, D. Schepers, A. Simmons, C. Soci, S. Abdalla, X. Abellan, G. Balsamo, P. Bechtold, G. Biavati, J. Bidlot, M. Bonavita, G. Chiara, P. Dahlgren, D. Dee, M. Diamantakis, R. Dragani, J. Flemming, R. Forbes, M. Fuentes, A. Geer, L. Haimberger, S. Healy, R. J. Hogan, E. Hólm, M. Janisková, S. Keeley, P. Laloyaux, P. Lopez, C. Lupu, G. Radnoti, P. Rosnay, I. Rozum, F. Vamborg, S. Villaume, and J.

Thépaut, 2020: The ERA5 global reanalysis. *Quarterly journal of the Royal Meteorological Society*, **146**, 1999-2049, doi:10.1002/qj.3803.

Horton, R. M., J. S. Mankin, C. Lesk, E. Coffel, and C. Raymond, 2016: A Review of Recent Advances in Research on Extreme Heat Events. *Curr Clim Change Rep*, **2**, 242-259, doi:10.1007/s40641-016-0042-x.

Hoskins, B. J., P. J. Valdes, 1990: On the existence of storm-tracks. *Journal of the atmospheric sciences*, **47**, 1854-1864, doi:10.1175/1520-0469(1990)047<1854:OTEOST>2.0.CO;2.

Hoskins, B. J., K. I. Hodges, 2002: New perspectives on the Northern Hemisphere winter storm tracks. *Journal of the atmospheric sciences*, **59**, 1041-1061, doi:10.1175/1520-0469(2002)059<1041:NPOTNH>2.0.CO;2.

Hoskins, B. J., I. N. James, 2014: *Fluid Dynamics of the Mid-Latitude Atmosphere*. Advancing Weather and Climate Science, Wiley, .

Hu, Y., Da Yang, and Jun Yang, 2008: Blocking systems over an aqua planet. *Geophysical Research Letters*, **35**, L19818-n/a, doi:10.1029/2008GL035351.

Huang, C. S. Y., N. Nakamura, 2016: Local Finite-Amplitude Wave Activity as a Diagnostic of Anomalous Weather Events. *Journal of the atmospheric sciences*, **73**, 211-229, doi:10.1175/JAS-D-15-0194.1.

Huang, C. S. Y., N. Nakamura, 2017: Local wave activity budgets of the wintertime Northern Hemisphere: Implication for the Pacific and Atlantic storm tracks. *Geophysical research letters*, **44**, 5673-5682, doi:10.1002/2017GL073760.

Jiang, T., K. Evans, M. Branstetter, P. Caldwell, R. Neale, P. J. Rasch, Q. Tang, and S. Xie, 2019: Northern Hemisphere Blocking in ~25-km-Resolution E3SM v0.3 Atmosphere-

Land Simulations. *Journal of geophysical research. Atmospheres*, **124**, 2465-2482,

doi:10.1029/2018JD028892.

Jung, T., M. J. Miller, L. Marx, C. Stan, K. I. Hodges, T. N. Palmer, P. Towers, N. Wedi, D.

Achuthavarier, J. M. Adams, E. L. Altshuler, B. A. Cash, and J. L. Kinter, 2012: High-

Resolution Global Climate Simulations with the ECMWF Model in Project

Athena. *Journal of climate*, **25**, 3155-3172, doi:10.1175/JCLI-D-11-00265.1.

K. I. Hodges, R. W. Lee, and L. Bengtsson, 2011: A Comparison of Extratropical Cyclones in Recent Reanalyses ERA-Interim, NASA MERRA, NCEP CFSR, and JRA-25. *Journal of Climate*, **24**, 4888-4906, doi:10.1175/2011JCLI4097.1.

Kleiner, N., P. W. Chan, L. Wang, D. Ma, and Z. Kuang, 2021: Effects of Climate Model Mean-State Bias on Blocking Underestimation. *Geophysical research letters*, **48**, n/a, doi:10.1029/2021GL094129.

Luo, D., 2005: A barotropic envelope Rossby soliton model for block-eddy interaction. part I: Effect of topography. *Journal of the atmospheric sciences*, **62**, 5-21, doi:10.1175/1186.1.

Lupo, A. R., 2021: Atmospheric blocking events: a review. *Annals of the New York Academy of Sciences*, **1504**, 5-24, doi:10.1111/nyas.14557.

Lupo, A. R., L. F. Bosart, 1999: An analysis of a relatively rare case of continental blocking. Quarterly journal of the Royal Meteorological Society, 125, 107-138, doi:10.1256/smsqj.55306.

Lutsko, N. J., I. M. Held, 2016: The Response of an Idealized Atmosphere to Orographic Forcing: Zonal versus Meridional Propagation. *Journal of the Atmospheric Sciences*, **73**, 3701-3718, doi:10.1175/JAS-D-16-0021.1.

- Manabe, S., T. B. Terpstra, 1974: The Effects of Mountains on the General Circulation of the Atmosphere as Identified by Numerical Experiments. *Journal of the Atmospheric Sciences*, **31**, 3-42, doi:10.1175/1520-0469(1974)031<0003:TEOMOT>2.0.CO;2.
- Masato, G., B. J. Hoskins, and T. J. Woollings, 2012: Wave-breaking characteristics of midlatitude blocking. *Quarterly journal of the Royal Meteorological Society*, **138**, 1285-1296, doi:10.1002/qj.990.
- Masato, G., B. J. Hoskins, and T. Woollings, 2013: Winter and Summer Northern Hemisphere Blocking in CMIP5 Models. *Journal of climate*, **26**, 7044-7059, doi:10.1175/JCLI-D-12-00466.1.
- Mattingly, K. S., J. T. McLeod, J. A. Knox, J. M. Shepherd, and T. L. Mote, 2015: A climatological assessment of Greenland blocking conditions associated with the track of Hurricane Sandy and historical North Atlantic hurricanes. *International journal of climatology*, **35**, 746-760, doi:10.1002/joc.4018.
- Miralles, D., A. J. Teuling, v. Heerwaarden C.C., and J. Vilà-Guerau de Arellano, 2014: Megahotwave temperatures due to combined soil desiccation and atmospheric heat accumulation. *Nature geoscience*, **7**, 345-349, doi:10.1038/ngeo2141.
- Nabizadeh, E., P. Hassanzadeh, D. Yang, and E. A. Barnes, 2019: Size of the Atmospheric Blocking Events: Scaling Law and Response to Climate Change. *Geophysical Research Letters*, **46**, 13488-13499, doi:10.1029/2019GL084863.
- Nabizadeh, E., S. W. Lubis, and P. Hassanzadeh, 2021: The 3D Structure of Northern Hemisphere Blocking Events: Climatology, Role of Moisture, and Response to Climate Change. *Journal of climate*, , 1-54, doi:10.1175/JCLI-D-21-0141.1.

Nakamura, H., J. M. Wallace, 1993: Synoptic behavior of baroclinic eddies during the blocking onset. *Monthly weather review*, **121**, 1892-1903, doi:10.1175/1520-0493(1993)121<1892:SBOBED>2.0.CO;2.

Nakamura, H., M. Nakamura, and J. L. Anderson, 1997: The Role of High- and Low-Frequency Dynamics in Blocking Formation. *Monthly Weather Review*, **125**, 2074-2093, doi:10.1175/1520-0493(1997)125<2074:TROHAL>2.0.CO;2.

Nakamura, H., A. Shimpo, 2004: Seasonal Variations in the Southern Hemisphere Storm Tracks and Jet Streams as Revealed in a Reanalysis Dataset. *Journal of Climate*, **17**, 1828-1844, doi:10.1175/1520-0442(2004)017<1828:SVITSH>2.0.CO;2.

Nakamura, N., C. S. Y. Huang, 2018a: Atmospheric blocking as a traffic jam in the jet stream. *Science (New York, N.Y.)*, **361**, 42-47, doi:10.1126/science.aat0721.

Nakamura, N., C. S. Y. Huang, 2018b: Atmospheric blocking as a traffic jam in the jet stream. *Science (American Association for the Advancement of Science)*, **361**, 42-47, doi:10.1126/science.aat0721.

Narinesingh, V., J. F. Booth, S. K. Clark, and Y. Ming, 2020: Atmospheric blocking in an aquaplanet and the impact of orography. *Weather and Climate Dynamics*, **1**, 293-311, doi:10.5194/wcd-1-293-2020.

Neal, E., Huang, C., & Nakamura, N. (2021, December). Regional Wave Activity Budget during the Pacific Northwest Heat Wave of June 2021. *AGU Fall Meeting 2021*. AGU.

O'Gorman, P. A., T. Schneider, 2008: The Hydrological Cycle over a Wide Range of Climates Simulated with an Idealized GCM. *Journal of Climate*, **21**, 3815-3832, doi:10.1175/2007JCLI2065.1.

- Paolo Davini, Fabio D'Andrea, 2016: Northern Hemisphere Atmospheric Blocking Representation in Global Climate Models. *Journal of climate*, **29**, 8823-8840, doi:10.1175/JCLI-D-16-0242.1.
- Paradise, A., C. B. Rocha, P. Barpanda, and N. Nakamura, 2019: Blocking Statistics in a Varying Climate: Lessons from a “Traffic Jam” Model with Pseudostochastic Forcing. *Journal of the atmospheric sciences*, **76**, 3013-3027, doi:10.1175/JAS-D-19-0095.1.
- Pelly, J. L., B. J. Hoskins, 2003: A New Perspective on Blocking. *Journal of the Atmospheric Sciences*, **60**, 743-755, doi:10.1175/1520-0469(2003)060<0743:ANPOB>2.0.CO;2.
- Perkins, S. E., 2015: A review on the scientific understanding of heatwaves—Their measurement, driving mechanisms, and changes at the global scale. *Atmospheric research*, **164-165**, 242-267, doi:10.1016/j.atmosres.2015.05.014.
- Pfahl, S., C. Schwierz, M. Croci-Maspoli, C. M. Grams, and H. Wernli, 2015a: Importance of latent heat release in ascending air streams for atmospheric blocking. *Nature Geoscience*, **8**, 610-614, doi:10.1038/ngeo2487.
- Pfahl, S., C. Schwierz, M. Croci-Maspoli, C. M. Grams, and H. Wernli, 2015b: Importance of latent heat release in ascending air streams for atmospheric blocking. *Nature geoscience*, **8**, 610-614, doi:10.1038/ngeo2487.
- Pfahl, S., H. Wernli, 2012: Quantifying the relevance of atmospheric blocking for co-located temperature extremes in the Northern Hemisphere on (sub-)daily time scales. *Geophysical research letters*, **39**, n/a, doi:10.1029/2012GL052261.

- Pithan, F., T. G. Shepherd, G. Zappa, and I. Sandu, 2016: Climate model biases in jet streams, blocking and storm tracks resulting from missing orographic drag. *Geophysical Research Letters*, **43**, 7231-7240, doi:10.1002/2016GL069551.
- Quintanar, A. I., C. R. Mechoso, 1995: Quasi-Stationary Waves in the Southern Hemisphere. Part I: Observational Data. *Journal of Climate*, **8**, 2659-2672, doi:10.1175/1520-0442(1995)008<2659:QSWITS>2.0.CO;2.
- Reinhold, B. B., R. T. Pierrehumbert, 1982: Dynamics of Weather Regimes: Quasi-Stationary Waves and Blocking. *Monthly weather review*, **110**, 1105-1145, doi:10.1175/1520-0493(1982)110<1105:DOWRQS>2.0.CO;2.
- Rex, D. F., 2011: Blocking Action in the Middle Troposphere and its Effect upon Regional Climate. *Tellus A*, , doi:10.3402/tellusa.v2i3.8546.
- Rex, D. F., 1950: Blocking Action in the Middle Troposphere and its Effect upon Regional Climate: II. The climatology of Blocking Action. *Tellus*, **2**, 275-301, doi:10.1111/j.2153-3490.1950.tb00339.x.
- Riahi, K., S. Rao, V. Krey, C. Cho, V. Chirkov, G. Fischer, G. Kindermann, N. Nakicenovic, and P. Rafaj, 2011: RCP 8.5—A scenario of comparatively high greenhouse gas emissions. *Climatic Change*, **109**, 33-57, doi:10.1007/s10584-011-0149-y.
- Sausen, R., W. König, and F. Sielmann, 1995: Analysis of blocking events from observations and ECHAM model simulations. *Tellus. Series A, Dynamic meteorology and oceanography*, **47**, 421-438, doi:10.3402/tellusa.v47i4.11526.
- Scaife, A. A., D. Copsey, C. Gordon, C. Harris, T. Hinton, S. Keeley, A. O'Neill, M. Roberts, and K. Williams, 2011: Improved Atlantic winter blocking in a climate model. *Geophysical research letters*, **38**, n/a, doi:10.1029/2011GL049573.

- Schiemann, R., P. Athanasiadis, D. Barriopedro, F. Doblas-Reyes, K. Lohmann, M. J. Roberts, D. V. Sein, C. D. Roberts, L. Terray, and P. L. Vidale, 2020: Northern Hemisphere blocking simulation in current climate models: evaluating progress from the Climate Model Intercomparison Project Phase 5 to 6 and sensitivity to resolution. *Weather and Climate Dynamics*, **1**, 277-292, doi:10.5194/wcd-1-277-2020.
- Schwierz, C., M. Croci-Maspoli, and H. C. Davies, 2004: Perspicacious indicators of atmospheric blocking. *Geophysical research letters*, **31**, L06125-n/a, doi:10.1029/2003GL019341.
- Shaposhnikov, D., B. Revich, T. Bellander, G. Bedada, M. Bottai, T. Kharkova, E. Kvasha, E. Lezina, T. Lind, E. Semutnikova, and G. Pershagen, 2014: Mortality Related to Air Pollution with the Moscow Heat Wave and Wildfire of 2010. *Epidemiology (Cambridge, Mass.)*, **25**, 359-364, doi:10.1097/EDE.0000000000000090.
- Shutts, G. J., 1983: The propagation of eddies in diffluent jetstreams: Eddy vorticity forcing of ‘blocking’ flow fields. *Quarterly journal of the Royal Meteorological Society*, **109**, 737-761, doi:10.1002/qj.49710946204.
- Sillmann, J., M. Croci-Maspoli, M. Kallache, and R. W. Katz, 2011: Extreme Cold Winter Temperatures in Europe under the Influence of North Atlantic Atmospheric Blocking. *Journal of climate*, **24**, 5899-5913, doi:10.1175/2011JCLI4075.1.
- Steinfeld, D., M. Boettcher, R. Forbes, and S. Pfahl, 2020: The sensitivity of atmospheric blocking to upstream latent heating – numerical experiments. *Weather and Climate Dynamics*, **1**, 405-426, doi:10.5194/wcd-1-405-2020.
- Steinfeld, D., S. Pfahl, 2019: The role of latent heating in atmospheric blocking dynamics: a global climatology. *Clim Dyn*, **53**, 6159-6180, doi:10.1007/s00382-019-04919-6.

- Strong, C., G. Magnusdottir, 2008: Tropospheric Rossby Wave Breaking and the NAO/NAM. *Journal of the Atmospheric Sciences*, **65**, 2861-2876, doi:10.1175/2008JAS2632.1.
- Suarez-Gutierrez, L., W. A. Müller, C. Li, and J. Marotzke, 2020: Dynamical and thermodynamical drivers of variability in European summer heat extremes. *Clim Dyn*, **54**, 4351-4366, doi:10.1007/s00382-020-05233-2.
- Takaya, K., H. Nakamura, 2001: A formulation of a phase-independent wave-activity flux for stationary and migratory quasigeostrophic eddies on a zonally varying basic flow. *Journal of the atmospheric sciences*, **58**, 608-627, doi:10.1175/1520-0469(2001)058<0608:AFOAPI>2.0.CO;2.
- Tibaldi, S., E. Tosi, A. Navarra, and L. Pedulli, 1994: Northern and Southern Hemisphere Seasonal Variability of Blocking Frequency and Predictability. *Monthly Weather Review*, **122**, 1971-2003, doi:10.1175/1520-0493(1994)122<1971:NASHSV>2.0.CO;2.
- Tibaldi, S., F. Molteni, 1990: On the operational predictability of blocking. *Tellus. Series A, Dynamic meteorology and oceanography*, **42**, 343-365, doi:10.3402/tellusa.v42i3.11882.
- Trenberth, K. E., 1986: An assessment of the impact of transient eddies on the zonal flow during a blocking episode using localized Eliassen-Palm flux diagnostics. *Journal of the atmospheric sciences*, **43**, 2070-2087, doi:10.1175/1520-0469(1986)043<2070:AAOTIO>2.0.CO;2.
- Trenberth, K. E., 1991: Storm Tracks in the Southern Hemisphere. *Journal of the Atmospheric Sciences*, **48**, 2159-2178, doi:10.1175/1520-0469(1991)048<2159:STITSH>2.0.CO;2.

- Trenberth, K. E., J. T. Fasullo, 2012: Climate extremes and climate change: The Russian heat wave and other climate extremes of 2010. *Journal of Geophysical Research: Atmospheres*, **117**, n/a, doi:10.1029/2012JD018020.
- Trigo, R., I. Trigo, C. DaCamara, and T. Osborn, 2004: Climate impact of the European winter blocking episodes from the NCEP/NCAR Reanalyses. *Clim. Dynam.*, **23**, 17-28, doi:10.1007/s00382-004-0410-4.
- Troen, I. B., L. Mahrt, 1986: A simple model of the atmospheric boundary layer; sensitivity to surface evaporation. *Boundary-Layer Meteorology*, **37**, 129-148, doi:10.1007/BF00122760.
- Tung, K. K., R. S. Lindzen, 1979: A Theory of Stationary Long Waves. Part I: A Simple Theory of Blocking. *Monthly weather review*, **107**, 714-734, doi:10.1175/1520-0493(1979)107<0714:ATOSLW>2.0.CO;2.
- Tyrlis, E., B. J. Hoskins, 2008: Aspects of a Northern Hemisphere Atmospheric Blocking Climatology. *Journal of the atmospheric sciences*, **65**, 1638-1652, doi:10.1175/2007JAS2337.1.
- Valdes, P. J., B. J. Hoskins, 1991: Nonlinear Orographically Forced Planetary Waves. *Journal of the Atmospheric Sciences*, **48**, 2089-2106, doi:10.1175/1520-0469(1991)048<2089:NOFPW>2.0.CO;2.
- Vallis, G. K., G. Colyer, R. Geen, E. Gerber, M. Jucker, P. Maher, A. Paterson, M. Pietschnig, J. Penn, and S. I. Thomson, 2018: Isca, v1.0: a framework for the global modelling of the atmospheres of Earth and other planets at varying levels of complexity. *Geoscientific Model Development*, **11**, 843-859, doi:10.5194/gmd-11-843-2018.

- Wallace, J. M., G. Lim, and M. L. Blackmon, 1988: Relationship between Cyclone Tracks, Anticyclone Tracks and Baroclinic Waveguides. *Journal of the Atmospheric Sciences*, **45**, 439-462, doi:10.1175/1520-0469(1988)045<0439:RBCTAT>2.0.CO;2.
- Wang, L., Z. Kuang, 2019: Evidence against a general positive eddy feedback in atmospheric blocking.
- Wegren, S. K., 2011: Food Security and Russia's 2010 Drought. *Eurasian geography and economics*, **52**, 140-156, doi:10.2747/1539-7216.52.1.140.
- White, R. H., D. S. Battisti, and G. H. Roe, 2017: Mongolian Mountains Matter Most: Impacts of the Latitude and Height of Asian Orography on Pacific Wintertime Atmospheric Circulation. *Journal of Climate*, **30**, 4065-4082, doi:10.1175/JCLI-D-16-0401.1.
- Wills, R. C. J., R. H. White, and X. J. Levine, 2019: Northern Hemisphere Stationary Waves in a Changing Climate. *Current climate change reports*, **5**, 372-389, doi:10.1007/s40641-019-00147-6.
- Wirth, V., M. Riemer, E. K. M. Chang, and O. Martius, 2018: Rossby Wave Packets on the Midlatitude Waveguide—A Review. *Monthly Weather Review*, **146**, 1965-2001, doi:10.1175/MWR-D-16-0483.1.
- Wolf, G., V. Wirth, 2017: Diagnosing the Horizontal Propagation of Rossby Wave Packets along the Midlatitude Waveguide. *Monthly weather review*, **145**, 3247-3264, doi:10.1175/MWR-D-16-0355.1.
- Woollings, T., 2010: Dynamical influences on European climate: an uncertain future. *Philosophical transactions of the Royal Society of London. Series A: Mathematical, physical, and engineering sciences*, **368**, 3733-3756, doi:10.1098/rsta.2010.0040.

- Woollings, T., E. Barnes, B. Hoskins, Y. Kwon, R. W. Lee, C. Li, E. Madonna, M. McGraw, T. Parker, R. Rodrigues, C. Spensberger, and K. Williams, 2018: Daily to Decadal Modulation of Jet Variability. *Journal of climate*, **31**, 1297-1314, doi:10.1175/JCLI-D-17-0286.1.
- Woollings, T., D. Barriopedro, J. Methven, S. Son, O. Martius, B. Harvey, J. Sillmann, A. R. Lupo, and S. Seneviratne, 2018a: Blocking and its Response to Climate Change. *Curr Clim Change Rep*, **4**, 287-300, doi:10.1007/s40641-018-0108-z.
- Woollings, T., D. Barriopedro, J. Methven, S. Son, O. Martius, B. Harvey, J. Sillmann, A. Lupo, and S. Seneviratne, 2018b: Blocking and its Response to Climate Change. *Curr Clim Change Rep*, **4**, 287-300, doi:10.1007/s40641-018-0108-z.
- Yamazaki, A., M. Honda, and A. Kuwano-Yoshida, 2015: Heavy Snowfall in Kanto and on the Pacific Ocean Side of Northern Japan Associated with Western Pacific Blocking. *Scientific online letters on the atmosphere*, **11**, 59-64, doi:10.2151/sola.2015-013.
- Yamazaki, A., H. Itoh, 2009: Selective absorption mechanism for the maintenance of blocking. *Geophysical research letters*, **36**, L05803-n/a, doi:10.1029/2008GL036770.
- Yamazaki, A., H. Itoh, 2013: Vortex–Vortex Interactions for the Maintenance of Blocking. Part I: The Selective Absorption Mechanism and a Case Study. *Journal of the Atmospheric Sciences*, **70**, 725-742, doi:10.1175/JAS-D-11-0295.1.
- Yamazaki, A., H. ITOH, 2013: Vortex–Vortex Interactions for the Maintenance of Blocking. Part II: Numerical Experiments. *Journal of the atmospheric sciences*, **70**, 743-766, doi:10.1175/JAS-D-12-0132.1.

- Yanai, M., T. Tomita, 1998: Seasonal and Interannual Variability of Atmospheric Heat Sources and Moisture Sinks as Determined from NCEP–NCAR Reanalysis. *Journal of climate*, **11**, 463-482, doi:10.1175/1520-0442(1998)011<0463:SAIVOA>2.0.CO;2.
- Yanai, M., S. Esbensen, and J. Chu, 1973: Determination of Bulk Properties of Tropical Cloud Clusters from Large-Scale Heat and Moisture Budgets. *Journal of the atmospheric sciences*, **30**, 611-627, doi:10.1175/1520-0469(1973)030<0611:DOBPOT>2.0.CO;2.
- Yeh, T., 1949: On Energy Dispersion in the Atmosphere. *Journal of meteorology*, **6**, 1-16, doi:10.1175/1520-0469(1949)006<0001:OEDITA>2.0.CO;2.
- Zhao, M., J. - Golaz, I. M. Held, H. Guo, V. Balaji, R. Benson, J. - Chen, X. Chen, L. J. Donner, J. P. Dunne, K. Dunne, J. Durachta, S. - Fan, S. M. Freidenreich, S. T. Garner, P. Ginoux, L. M. Harris, L. W. Horowitz, J. P. Krasting, A. R. Langenhorst, Z. Liang, P. Lin, S. - Lin, S. L. Malyshev, E. Mason, P. C. D. Milly, Y. Ming, V. Naik, F. Paulot, D. Paynter, P. Phillipps, A. Radhakrishnan, V. Ramaswamy, T. Robinson, D. Schwarzkopf, C. J. Seman, E. Shevliakova, Z. Shen, H. Shin, L. G. Silvers, J. R. Wilson, M. Winton, A. T. Wittenberg, B. Wyman, and B. Xiang, 2018: The GFDL Global Atmosphere and Land Model AM4.0/LM4.0: 1. Simulation Characteristics With Prescribed SSTs. *Journal of advances in modeling earth systems*, **10**, 691-734, doi:10.1002/2017MS001208.

ProQuest Number: 28965789

INFORMATION TO ALL USERS

The quality and completeness of this reproduction is dependent on the quality
and completeness of the copy made available to ProQuest.



Distributed by ProQuest LLC (2022).

Copyright of the Dissertation is held by the Author unless otherwise noted.

This work may be used in accordance with the terms of the Creative Commons license
or other rights statement, as indicated in the copyright statement or in the metadata
associated with this work. Unless otherwise specified in the copyright statement
or the metadata, all rights are reserved by the copyright holder.

This work is protected against unauthorized copying under Title 17,
United States Code and other applicable copyright laws.

Microform Edition where available © ProQuest LLC. No reproduction or digitization
of the Microform Edition is authorized without permission of ProQuest LLC.

ProQuest LLC
789 East Eisenhower Parkway
P.O. Box 1346
Ann Arbor, MI 48106 - 1346 USA